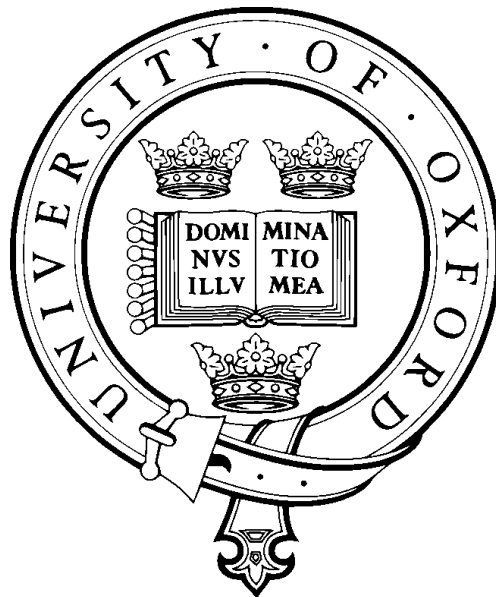


Retrieval of non-standard species from MIPAS-ENVISAT

Joanne Christine Walker
St Anne's College

Atmospheric, Oceanic and Planetary Physics
Clarendon Laboratory
University of Oxford



Thesis submitted for the Degree of Doctor of Philosophy in the
University of Oxford

· 2008 ·

Abstract

Trace gas retrievals from high spectral resolution infra-red limb emission measurements using the Michelson Interferometer for Passive Atmospheric Sounding (MIPAS) are presented.

The effect of reduced spectral resolution and increased vertical sampling, introduced after a fault was detected in the interferometer slide mechanism, is investigated for the retrieval of a best (N_2O_5) and worst case (CO) molecule.

The thesis then addresses the principal hypothesis that the six species retrieved operationally by ESA: H_2O , O_3 , HNO_3 , CH_4 , N_2O and NO_2 , can be extended to include other species of scientific interest in an Oxford-specific state of the art retrieval system. In particular, we investigate the feasibility of an operational algorithm for the retrieval of CO which is an important tracer used throughout the atmosphere. Limb-viewing measurements of CO emission in the infra-red are complicated by non-LTE (non local thermodynamic equilibrium) effects, and currently sophisticated models of the non-LTE excitation are required within the retrieval process, resulting in long processing times, which are considered impractical for the purposes of an operational retrieval. We investigate an alternative approach, whereby CO is retrieved jointly with a non-LTE parameter known as “vibrational temperature” that characterises the effects. Such a method, if successful, is simpler to implement and faster. In simulations, we find that the prior estimate of vibrational temperature needs to be known to within 7 K for the successful retrieval of CO. A preliminary climatology of vibrational temperature is developed and is applied to retrievals from real data. We find that it is particularly important to characterise the non-LTE excitation in the mesosphere. However, there are large biases due to non-LTE effects that remain unaccounted for, and we conclude that knowledge of vibrational temperature needs to be so good, that on-line calculations, such as are already performed by IMK/IAA, may be required for an accurate retrieval.

As part of the advancement of a suite of NO_y chemistry measurements, the retrieval of the diurnally varying species N_2O_5 is improved. The improved retrieval is validated using a novel method which compares two estimates of a rate constant associated with its nighttime formation. Very good agreement is obtained and estimated biases in the N_2O_5 retrieval are less than 0.1 ± 0.3 ppbv under most circumstances. We then show in simulations how biases introduced into the log-space retrieval of very small values of N_2O_5 , caused by the asymmetry of the *a priori* distribution, can be removed by performing the retrieval in linear-space.

Finally, a climatology of NO_y (Nighttime NO_2 , HNO_3 , $2 \times \text{N}_2\text{O}_5$ and ClONO_2) is outlined for the first time using both the full and reduced resolution datasets from 2002–2008. Correlations calculated for extra-vortex air reveal very good agreement between full and reduced resolution data and high altitude aircraft measurements.

Contents

Acknowledgments	xi
1 Introduction	1
1.1 MIPAS	3
1.1.1 Overview	3
1.1.2 Viewing geometry	4
1.1.3 Instrument hardware	5
1.1.4 Interferometry	7
1.1.5 Data processing	9
1.1.6 Changes to the mission plan	10
1.2 Radiative Transfer	12
1.3 Forward models	13
1.3.1 RFM	14
1.3.2 GRANADA	14
1.4 Retrieval methods	14
1.4.1 Definitions	16
1.4.2 Unconstrained least-squares solution	17
1.4.3 Regularised least-squares solution	19
1.4.4 Optimal estimation	19
1.4.5 Retrieval diagnostics	20
1.4.6 Iterative methods	23

1.5	Microwindow selection	24
1.6	Background continuum	26
1.7	Retrieval algorithms	29
1.7.1	MORSE	29
1.7.2	MIPAS level 2 operational analysis	30
2	Impact of reduced spectral resolution modes	31
2.1	Introduction	31
2.1.1	Impact of reduced spectral resolution	33
2.1.2	Impact of retrieval grid spacing	35
2.2	Random errors	36
2.2.1	CO	36
2.2.2	N ₂ O ₅	40
2.3	Systematic errors	42
2.4	Conclusions	45
3	Carbon monoxide	50
3.1	Role in the atmosphere	50
3.2	Previous measurements	51
3.3	Non local thermodynamic equilibrium	54
3.3.1	Vibrational temperature	59
3.3.2	Treatment of non-LTE in the RFM	60
3.3.3	Existing non-LTE retrieval schemes	60
3.4	Systematic errors due to ignoring non-LTE	61
3.5	LTE retrieval	65
3.5.1	Comparisons with EOS MLS	66
3.5.2	Zonal mean profiles	71
3.5.3	Conclusions and future work	72
3.6	Joint retrieval of CO and vibrational temperature	73

3.6.1	Retrieval precision	73
3.6.2	Retrievals from simulated data	75
3.6.3	Preliminary T_v climatology	82
3.6.4	CO climatology	87
3.6.5	Retrievals from real data	87
3.6.6	Conclusions and future work	90
3.7	Non-LTE effects in CO isotopologues	92
3.7.1	Estimating T_v of isotopologues	96
3.8	Observations of the hot bands	98
3.8.1	Conclusions and future work	100
4	N_2O_5 from MIPAS-ENVISAT	101
4.1	Role in the atmosphere	102
4.1.1	The diurnal cycle	103
4.2	Previous measurements	106
4.3	Improving retrieval precision	108
4.4	Retrieval method	109
4.5	Validation of N_2O_5 retrieval	111
4.5.1	Standard rate constant	111
4.5.2	Determination of N_2O_5 -dependent rate constant	112
4.5.3	Rate constant from nighttime observations only	114
4.5.4	Rate constant including daytime observations	116
4.5.5	Implied bias in retrieved N_2O_5	124
4.6	Linear-space retrieval of N_2O_5	124
4.6.1	Retrieval simulations	125
4.7	Conclusions and future work	126
5	Long-term measurements of NO_y	129
5.1	Previous measurements	134

5.2	Retrieval method	136
5.2.1	Random and systematic errors in total NO _y	138
5.3	Global and seasonal variation of NO _y	138
5.3.1	Time series	138
5.3.2	Correlations between N ₂ O and NO _y	145
5.4	Conclusions and future work	151
6	Conclusions	153
6.1	Future Work	160
A	Derivation of N₂O₅-dependent rate constant	163
B	NO_y random and sytematic errors	165
C	Coordinate transformations	170
C.1	Potential vorticity potential temperature coordinates	170
C.2	Equivalent latitude	172
C.3	Defining the vortex edge	172
	Bibliography	172

List of Figures

1.1	MIPAS viewing geometry	4
1.2	MIPAS FR17, RR27 and RR19 scan patterns	6
1.3	Schematic of the MIPAS instrument	7
1.4	Generic layout of MIPAS FTS	8
1.5	Effect of apodisation on MIPAS spectra	9
1.6	Process of growing microwindows	26
1.7	Separating the contribution of the target gas from the back-ground continuum	28
2.1	The effect of a reduction in spectral resolution for narrow and broad spectral features (Dudhia, 2005).	33
2.2	Modelled CO line convolved with the FR and RR AILS	34
2.3	Simple relationship between retrieval sensitivity and grid spacing	35
2.4	Mid-latitude nighttime spectra of CO and contaminants at 12 km under LTE conditions simulated using RFM	37
2.5	Simulated CO random error for various retrieval and scan pattern configurations at full and reduced spectral resolution	38
2.6	Simulated CO averaging kernels for various retrieval grid and scan pattern configurations at full and reduced spectral resolution	39
2.7	Mid-latitude nighttime N ₂ O ₅ spectrum and contaminant gases at 30 km simulated using the RFM	41

2.8	Simulated retrieval random error for N_2O_5 for various retrieval configurations and scan patterns at full and reduced spectral resolution	42
2.9	Simulated N_2O_5 averaging kernels for various retrieval grids and scan pattern configurations at full and reduced spectral resolution	43
2.10	Spectral features and microwindows selected for CO and N_2O_5 in the FR17 and RR27 modes.	48
2.11	Random and systematic errors for CO in the FR17 and RR27 mode using operational microwindows. Retrieval points at tangent altitudes.	49
2.12	Random and systematic errors for N_2O_5 in FR17 and RR27 mode using operational microwindows. Retrieval points at tangent altitudes. Abbreviations are listed in 1.1.	49
3.1	Real MIPAS spectra at 12 km for day and nighttime observations	54
3.2	Simulated spectra for CO and contaminant gases at 12 km	62
3.3	Systematic errors introduced from ignoring non-LTE	63
3.4	Modelled 4.7 μm CO emission assuming LTE and including isotopic features. FR17 and RR27 microwindows	65
3.5	Zonally averaged CO VMR retrieved from real data assuming LTE conditions for 28th January 2005	67
3.6	MIPAS RR27 and MLS level 1b coverage on 28th January 2005	68
3.7	MLS and MIPAS RR27 simulated averaging kernels	69
3.8	Comparison of MLS (v2.22) and MIPAS RR27 LTE CO	71
3.9	Random errors for joint CO, T_v retrieval	74
3.10	Simulated retrieved profiles when T_v known exactly	76
3.11	Averaging kernels when prior T_v is known exactly	76

3.12	Simulated retrieved profiles using T_k as prior estimate of T_v	77
3.13	Averaging kernels using T_k as prior estimate of T_v	78
3.14	Biases in simulated retrievals when prior T_v is an underestimate. No upper-atmosphere column retrieval of CO	79
3.15	Biases in simulated retrievals when prior T_v is an overestimate	80
3.16	Biases in simulated retrievals when prior T_v is an underestimate. Upper-atmosphere column retrieval of CO	80
3.17	Biases in simulated retrievals when prior T_v is an overestimate. Upper-atmosphere column retrieval of CO	81
3.18	Non-LTE enhancements generated from non-LTE populations climatology for orbit#09155 on 30th November 2003	85
3.19	Error introduced into T_v climatology by parameterisation of non-LTE populations	86
3.20	Joint CO, vibrational temperature retrievals on real data . .	91
3.21	Observed and simulated spectra of CO isotopologues	94
3.22	Observed daytime radiance against RFM modelled radiance for CO isotopologues	96
3.23	Observed nighttime radiance against RFM modelled radiance for CO isotopologues	97
3.24	Derived T_v profiles of CO isotopologues	99
3.25	Observations of CO(2-1) hotband emission	100
4.1	The diurnal variation of stratospheric nitrogen species at 30 km	104
4.2	Simulated N_2O_5 retrieval random error	110
4.3	Simulated N_2O_5 ν_{12} band emission at 30 km	111
4.4	Daily zonal mean nighttime observations of NO_2 and N_2O_5 for dates between July 2002 and March 2004 at the 36 km tangent altitude.	115

4.5	Rate constants at 36 km.	117
4.6	Daily zonal mean daytime observations of N ₂ O ₅ for dates between July 2002 and March 2004 at the 36 km.	119
4.7	Estimates of rate constant scaled to T=235 K at 36 km	120
4.8	As in figure 4.7 but at 33 km	121
4.9	As in figure 4.7 but at 39 km	122
4.10	Implied relative and absolute bias in retrieved N ₂ O ₅ at 36 km.	123
4.11	Linear and log-space retrievals of N ₂ O ₅	126
5.1	Components of NO _y for equatorial conditions derived from climatological values by Remedios et al. (2007). NO ₂ , NO and N ₂ O ₅ profiles do not include diurnal variation. HNO ₄ , which cannot be measured by MIPAS, accounts for < 1% of total NO _y	130
5.2	Simplified reaction scheme for NO _y	131
5.3	Random and systematic errors calculated for total NO _y using FR17 and RR27 operational microwindows.	139
5.4	Time series of N ₂ O, NO _y species and ozone on the 600 K potential temperature surface	140
5.5	1 σ percentage standard deviation for monthly averages in 5° equivalent latitude bands for N ₂ O, NO _y species (nighttime NO ₂ , HNO ₃ , N ₂ O ₅ , ClONO ₂) and ozone on the 600 K potential temperature surface.	141
5.6	Random and systematic errors calculated for NO ₂ using FR17 and RR27 operational microwindows.	143
5.7	Time series of NO _y on 600 K, 800 K and 1000 K potential temperature surfaces	144
5.8	Standard deviation in percentage of time series of NO _y on 600 K, 800 K and 1000 K potential temperature surfaces	145

5.9	Correlations between N_2O and NO_y at 600 K for Northern and Southern Hemisphere winters in 2003, 2005 and 2007.	149
5.10	N_2O , NO_y correlations with altitude	151
B.1	Random and systematic errors calculated for N_2O using FR17 and RR27 operational microwindows.	167
B.2	Random and systematic errors calculated for NO_2 using FR17 and RR27 operational microwindows.	167
B.3	Random and systematic errors calculated for HNO_3 using FR17 and RR27 operational microwindows.	168
B.4	Random and systematic errors calculated for N_2O_5 using FR17 and RR27 operational microwindows.	168
B.5	Random and systematic errors calculated for ClONO_2 using FR17 and RR27 operational microwindows.	169
C.1	Illustration of potential vorticity	171
C.2	Determination of the vortex edge	173

List of Tables

1	Expansion of acronyms of instruments and platforms referred to in text	xiii
2	Expansion of various abbreviations used throughout the text	xiv
1.1	Sources of systematic error and estimates of 1σ uncertainty used in microwindow selection	25
2.1	Configurations examined in investigation into reduced spectral resolution modes	37
3.1	Some previous space-based measurements of atmospheric CO	52
3.2	Uncertainties on CO and T_v used for retrievals from real data	88
4.1	Some previous space-based measurements of atmospheric N_2O_5	107
4.2	Relative percentage bias introduced in log-space retrieval of small values of N_2O_5	127
5.1	Empirical correlation between N_2O and NO_y in Northern and Southern Hemispheres	150
B.1	FR17 mode microwindows used to retrieve NO_y	166
B.2	RR27 mode microwindows used to retrieve NO_y	166

Acknowledgments

Thanks to my parents, Christine and Craig Walker, without whom this work would surely not have been possible, from so many points of view. Many thanks to my supervisor Anu, who has probably shouldered more than his fair share of the burden of this DPhil, and has offered his support tirelessly, and without complaint, except for the occasional raised eyebrow. We should also acknowledge his role as guardian and protector; after all, without our loyal chaperone at the ENVISAT Symposium 2007, who knows what fate might have befallen the MIPAS Girls. Thanks to Chiara in her role as post-graduate mentor, for her advice and gentle encouragement. Thanks also to Don, who after an initial, brief period of supervision, left me, perhaps with some relief, in Anu's capable hands. Thank-you also to Manuel and Bernd in Granada, for a lovely visit, and a productive couple of weeks, in between tapas y cervezas. And thanks also to all my friends in AOPP, in particular Bob, Claire (MG), Jane (MG) and Ranah, without whose solidarity and support, I surely could not have completed this painful process. I had wondered in the past at a well-known quote included in the front of a previous student's thesis that begins "I have of late - but wherefore I know not - lost all my mirth, forgone all customs of exercises; and indeed it goes so heavily with my disposition that this goodly frame, the earth, seems to me a sterile promontory...." (Hamlet Act II Scene II), and had thought it to be over-doing it a little, a bit too morose perhaps, after all, Hamlet had really been having a bit of a hard time, but now having lived through the write-up process myself, I find that I am almost entirely in agreement with his sentiments, and thought even of including it, perhaps, in the front of my own thesis. Instead, I've decided to leave it to the curious DPhil reader to look the quote up for themselves, and hope instead that the post-thesis world regains its former lustre, and that each and every DPhil student is restored to their happy, enthusiastic¹ former selves.

This research was funded by the Natural Environment Research Council.

¹Anu may raise some objections as to whether these adjectives were ever really applicable in this particular student's case.

Instrument and platform acronyms

Instrument		Platform	
ACE-FTS	Atmospheric Chemistry Experiment Fourier Transform Spectrometer	SCISAT-1	SCIENCE SATellite
ATMOS	Atmospheric Trace MOlecule Spectroscopy	Spacelab 3	
CLAES	Cryogenic Limb Array Etalon Spectrometer	UARS	Upper Atmospheric Research Satellite
HALOE	Halogen Occultation Experiment	UARS	
IMG	Interferometric Monitor for Greenhouse gases	ADEOS	ADvanced Earth Observing Satellite
ISAMS	Improved Stratospheric and Mesospheric Sounder	UARS	
MIPAS	Michelson Interferometer for Passive Atmospheric Sounding	ENVISAT	ENVironmental SATellite
MLS	Microwave Limb Sounder	EOS	Earth Observing System
MOPITT	Measurements Of Pollution In The Troposphere	EOS	
OSIRIS	Optical Spectrograph and InfraRed Imager System	Odin AOS	Orbital Design INtegration (System) Acousto-Optical Spectrometer
SCIAMACHY	Scanning Imaging Absorption Spectrometer for Atmospheric CHartography	ENVISAT	
SMR	Sub-Millimetre Radiometer	Odin AOS	
TES	Tropospheric Emission Spectrometer	EOS	

Table 1: Expansion of acronyms of instruments and platforms referred to in the text.

Abbreviations used in text

FOV	Field-Of-View
FTS	Fourier Transform Spectrometer
FR	Full Resolution (spectral)
FWHM	Full Width at Half Maximum
GRANADA	Generic non-LTE populations model
ILS	Instrument Line Shape
IMK	Institut fr Meteorologie und Klimaforschung
IPF	Instrument Processing Facility
LST	Local Solar Time
LTE	Local Thermodynamic Equilibrium
MORSE	MIPAS Orbital Retrieval using Sequential Estimation
MPD	Maximum Path Difference
non-LTE	non Local Thermodynamic Equilibrium
RFM	Reference Forward Model
RR	Reduced Resolution (spectral)
RR19	RR special mode focussed on the UTLS with 19 vertical levels
RR27	nominal RR mode with 27 vertical levels
T_v	vibrational temperature
T_k	kinetic temperature
UTLS	Upper-Troposphere Lower-Stratosphere

Table 2: Expansion of various abbreviations used throughout the text.

Chapter 1

Introduction

Investigations are presented into extending the range of trace gas measurements from the Michelson Interferometer for Passive Atmospheric Sounding (MIPAS) to include important species whose retrieval is challenging using an Oxford-specific state of the art retrieval scheme. The instrument is a high spectral resolution limb-sounding Fourier transform spectrometer operating in the infra-red. It was launched aboard ESA's ENVIRONMENTAL SATELLITE (ENVISAT) in March 2002. Operations were halted for several months in March 2004 due to a fault in the interferometer slide mechanism. New measurement modes were introduced at a reduced spectral resolution in January 2005, with the reduced measurement time being exploited to increased vertical sampling. Chapter 2 explores the changes to the retrieval process arising from these alterations to the mission plan and quantifies their effect on retrieved species.

The thesis then addresses the principal hypothesis that the six species retrieved operationally by ESA: H_2O , O_3 , HNO_3 , CH_4 , N_2O and NO_2 , can be extended to include other species of scientific interest using an Oxford-specific state of the art retrieval scheme known as MIPAS Optimal Estimation using Sequential Estimation (MORSE). In particular,

we investigate the feasibility of an operational algorithm for the retrieval of CO, which is a useful tracer throughout the atmosphere. Observations of CO in the upper-troposphere have the potential to identify uplift events and long-range transport of pollution, as well as processes of tropospheric-stratospheric exchange. It can be used as a tracer of polar vortex dynamics in the stratosphere and mesosphere and as a reference tracer for other chemical species. However, infra-red emission measurements of CO in the limb-viewing geometry are complicated by non-LTE (non local thermodynamic equilibrium) effects, whereby emission is not described solely by the Planck function at the local kinetic temperature. In chapter 3, the feasibility of a joint retrieval of CO and a non-LTE parameter that characterises these effects is investigated.

Improvements are then made to the retrieval of the diurnally varying species N_2O_5 , forming part of the advancement of the suite of chemistry measurements for the so-called “big-five” NO_y species (HNO_3 , NO_2 , NO , N_2O_5 and ClONO_2) which make up the majority of odd nitrogen in the stratosphere, and play an important role in stratospheric ozone chemistry. Currently, MIPAS is the only space-based instrument to provide measurements of the local time variation of this gas. The Atmospheric Chemistry Experiment (ACE) Fourier Transform Spectrometer (-FTS) is also able to measure N_2O_5 but is only able to perform measurements at sunrise and sunset. Di-nitrogen pentoxide is not yet routinely measured from MIPAS, however, due to the difficulty in distinguishing its contribution from the spectrally flat background continuum. In chapter 4, the standard treatment of the background continuum is altered, resulting in improvements in retrieval precision of N_2O_5 , and a novel method is then presented to validate the retrieval, which avoids the use of complicated chemical transport models. Finally, in chapter 5 we outline a climatol-

ogy of NO_y , including the improved N_2O_5 retrieval, which for the first time incorporates both the full and reduced spectral resolution datasets, establishing the ability of the MIPAS instrument to provide long-term, global measurements of NO_y .

1.1 MIPAS

1.1.1 Overview

The Michelson Interferometer for Passive Atmospheric Sounding (MIPAS), launched aboard ESA's ENVISAT on 1st March 2002, is a high spectral resolution, limb-viewing fourier transform spectrometer (FTS). It measures thermal emission across a broad spectral region, 685–2410 cm^{-1} , where most gases have characteristic spectral signatures (Fischer and Oelhaf, 1996). The satellite sits in a sun-synchronous polar orbit at an altitude of around 800 km. There are approximately 14 orbits per day with pole-to-pole coverage. It completes a single orbit in around 100 minutes, ascending on the nightside at 22:00 LST (Local Solar Time) and descending on the dayside at 10:00 LST. In the original full spectral resolution mode (FR, sampled at 0.0250 cm^{-1}), which was operational between July 2002 and March 2004, measurements extended from 6 to 68 km with 3 km spacing in the upper-troposphere lower-stratosphere (UTLS), increasing to 8 km in the upper-stratosphere.

The instrument was switched off for several months after a fault in the drive unit of one of the interferometer mirrors became critical in late March 2004. Reduced spectral resolution modes (RR, sampled at 0.0625 cm^{-1}) with a shorter measurement time, were first tested during August 2004 using the original scan pattern and later, in January 2005, various new scan patterns, designed to take advantage of the re-

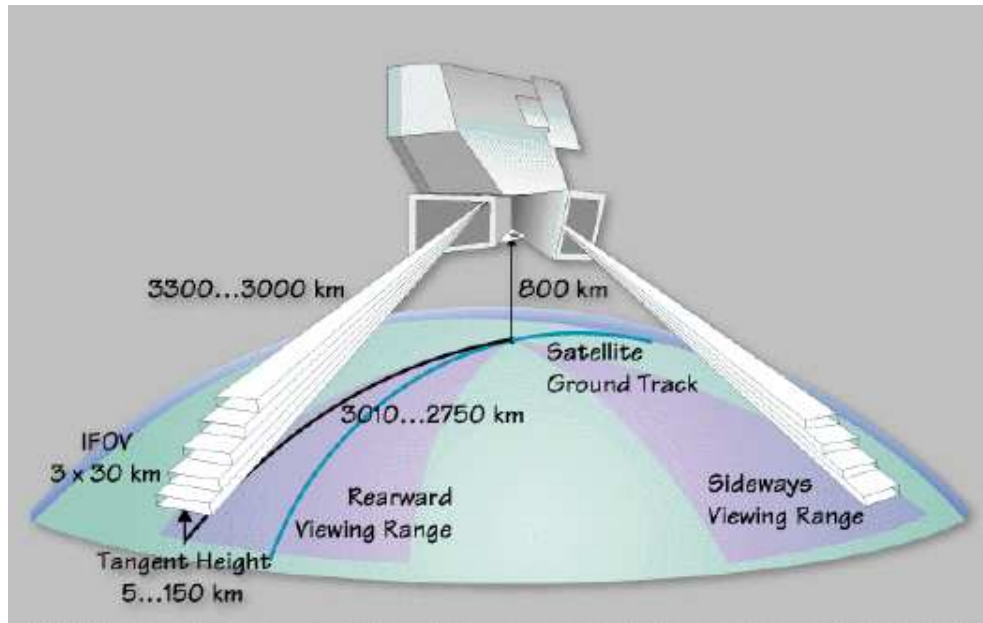


Figure 1.1: The viewing geometry of MIPAS. Most measurements are performed using the rearward view (MIPAS Product Handbook [Internet], 2008).

duced measurement time to increase vertical and horizontal coverage, were introduced. There have been large gaps in data coverage since the introduction of these new modes. However, since December 2007 the instrument has been in continuous operation, and the slide mechanism in the interferometer drive unit now appears to be operating more smoothly.

1.1.2 Viewing geometry

The long path length viewed through the atmosphere against the background of cold space allows for sensitive emission measurements of trace species. Figure 1.1 shows the rearward and azimuth viewing capabilities. Measurements are usually acquired in the rearward view although reduced resolution special modes have now been introduced using the azimuth viewing capability. The instantaneous field of view (FOV) is 3 km high in the vertical, providing good vertical resolution, and 30 km wide in the horizontal direction to boost signal. For optically thin paths,

the majority of radiance is emitted from the lowest point along this path, known as the tangent point, where the air density is highest. This defines the altitude at which gas concentrations are measured. The acquisition of the interferogram at a particular tangent height is called a sweep. Measurements at all tangent heights are known collectively as a scan. Figure 1.2 shows the original FR scan pattern, the RR nominal mode scan pattern (RR 27) and the most common RR special mode (UTLS-1). Adjacent levels in the RR modes overlap at low altitudes as the 3 km FOV of the instrument is wider than the 1.5 km grid spacing. A floating altitude grid is used in the RR modes beginning at a higher altitude at the equator than at the poles to minimise cloud contamination. Dashed lines in figure 1.2 show the vertical extent of floating grid. In the FR mode there is a horizontal spread of some 500 km in the tangent points within a single scan due to the motion of the platform around its orbit. Consecutive scans are spaced approximately 500 km apart. In the new RR modes, consecutive scans are spaced by approximately 410 km.

1.1.3 Instrument hardware

The optics module is shown in figure 1.3. The front-end optics consist of the elevation and azimuth scan units, an input telescope, as well as the black-body assembly used for calibrating the signal. From here the radiation is directed into the interferometer. The interfering beams are focussed onto a series of Hg:Cd:Te detectors in the focal plane subsystem. To reduce the self-emission of the instrument, and increase sensitivity to the atmospheric signal, the instrument is cooled passively using a series of radiators, tilted away from the earthshine. This cools the optics and focal plane subsystem to around 210K. Even so, the detectors need extremely high sensitivity, expressed in terms of Noise Equivalent Spectral Radi-

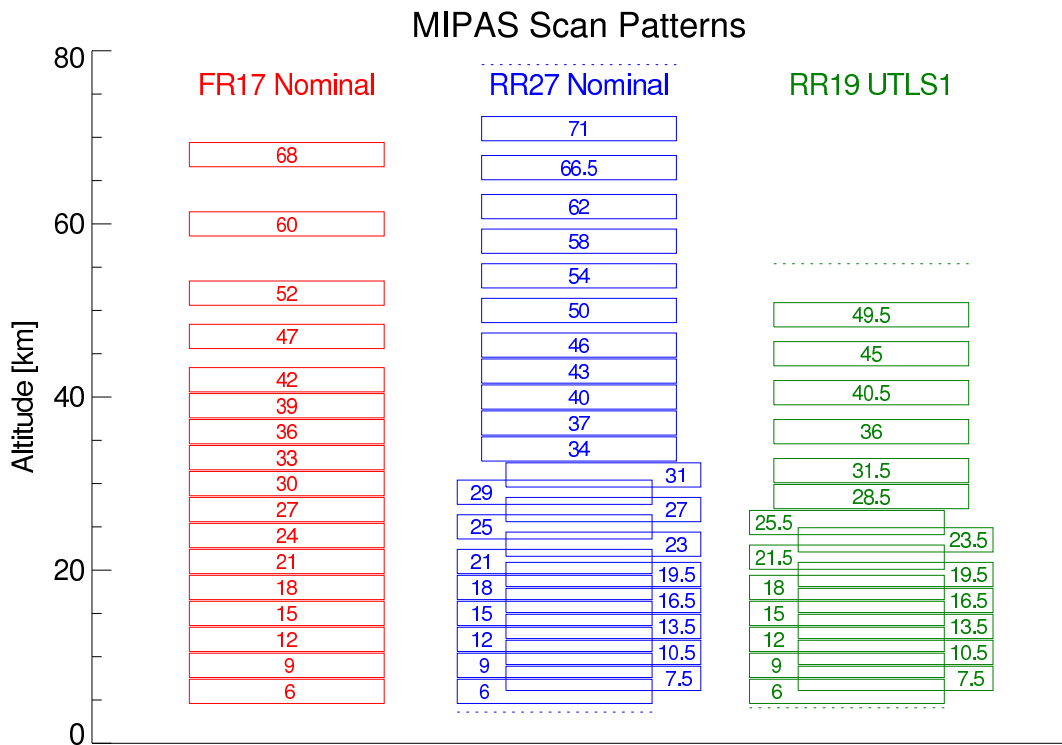


Figure 1.2: Nominal mode at full spectral resolution (RR17), nominal mode at reduced spectral resolution (RR27) and UTLS-1 special mode (RR19). Rectangles indicate extent of FOV. Dashed lines indicate extent of floating altitude grid.

ance (NESR), with an NESR $50 \text{ nWm}^{-2}\text{sr}^{-1}\text{cm}$ on the long wavelength side, decreasing to $4.2 \text{ nWm}^{-2}\text{sr}^{-1}\text{cm}$ on the short wavelength side, where atmospheric emission is weaker. In total, measurements are performed in 5 spectral bands: A: $685\text{--}970 \text{ cm}^{-1}$, AB: $1020\text{--}1170 \text{ cm}^{-1}$, B: $1215\text{--}1500 \text{ cm}^{-1}$, C: $1570\text{--}1750 \text{ cm}^{-1}$, D: $1820\text{--}2410 \text{ cm}^{-1}$. A good knowledge of the absolute radiance is essential for the retrieval of temperature and species concentrations, and radiometric accuracy of between 1 and 2 % has been reported in most situations, which is difficult to achieve even for ground based instruments (Kleinert et al., 2007). The calibration of the instrument and non-linearity of the spectral response are important aspects which contribute to the baseline signal, see section 1.6. Finally, the electronics module contains the elements which control the instrument and power and perform the first steps in processing the raw data which,

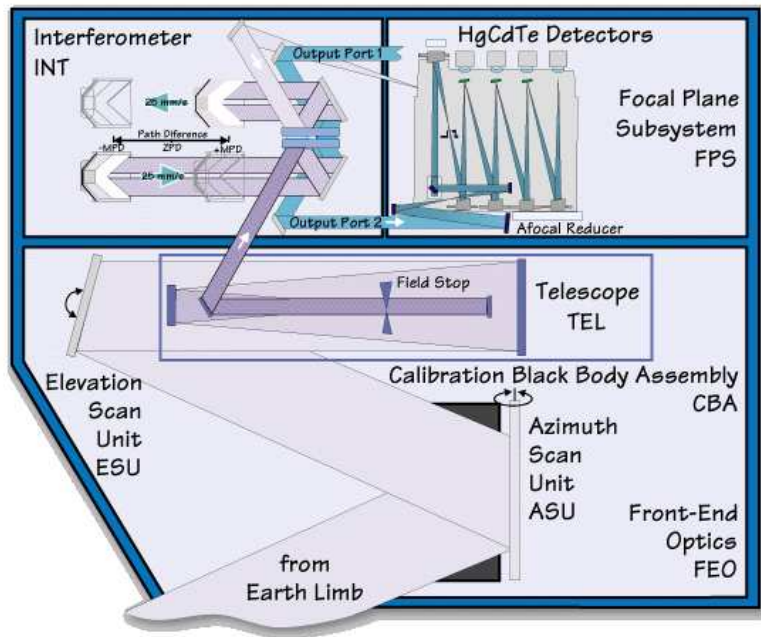


Figure 1.3: Schematic of the MIPAS instrument (MIPAS Product Handbook [Internet], 2008).

in order to maximise flexibility in data processing, is mainly limited to the digitisation and formatting, followed by transmission to ground.

1.1.4 Interferometry

The generic layout of the MIPAS FTS is shown in figure 1.4. The design is derived from a Michelson-type interferometer, but with two beams rather than one, providing better momentum balance aboard the orbiting platform. The input radiance is divided by a beamsplitter into two beams of similar intensity which travel along each arm of the interferometer and are reflected by moving retroreflectors into the beam combiner where they interfere. As the path difference travelled by each beam is altered, the phase between the two beams changes causing fluctuations in light intensity at each of the output ports. The sum of the intensity in both ports remains constant and the 2-sided interferogram allows the

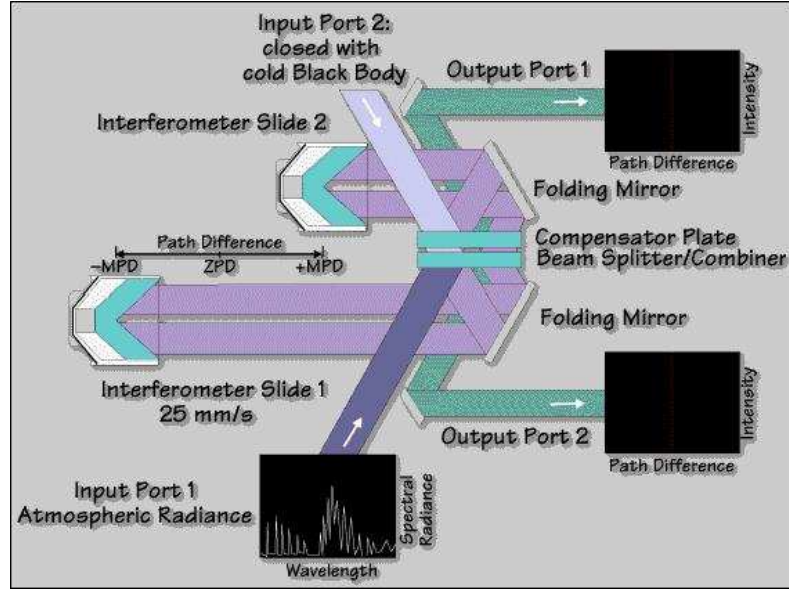


Figure 1.4: Generic layout of the MIPAS Fourier transform spectrometer (MIPAS Product Handbook [Internet], 2008).

phase to be calibrated helping to identify alignment errors. The inverse Fourier transform of this interference-modulated signal is known as an interferogram and yields the spectrum of the incoming radiation. For an infinite Maximum Path Difference (MPD), it is given by

$$F(\nu) = \frac{1}{L} \int_{-\infty}^{+\infty} G(x) \cos(2\pi\nu x) dx \quad (1.1)$$

where $G(x)$ is the recorded interferogram and $F(\nu)$ is the recovered radiance spectrum. The spectral resolution of the instrument is mostly determined by the MPD. The convolution of the interferogram with a boxcar function representing the MPD is equivalent to the convolution of the spectrum with a sinc function whose width is inversely proportional to the MPD. The spectral sampling grid is chosen to preserve as much information as possible and is used as the definition of spectral resolution throughout this thesis. In the original FR mode of operation, with an MPD of 20 cm, the spectral data was sampled on a 0.0250 cm^{-1}

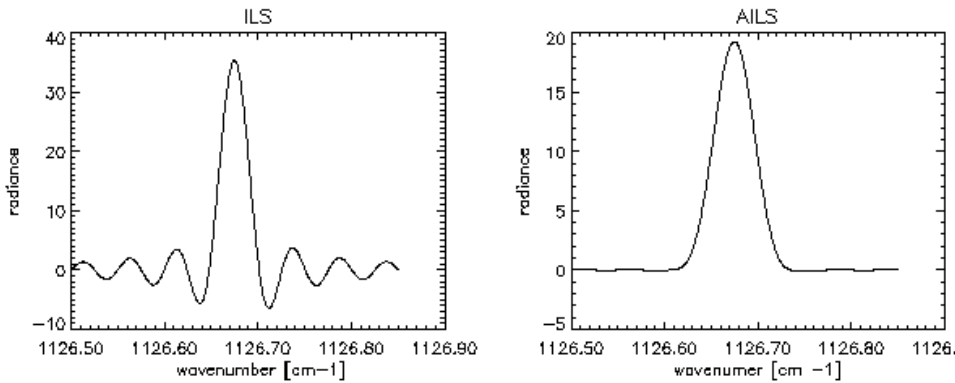


Figure 1.5: Apodisation of MIPAS spectra. Unapodised ILS has side lobes which introduce unwanted contributions from far away lines. Side lobes are suppressed in apodised ILS (AILS) (MIPAS Product Handbook [Internet], 2008).

grid. In the new RR modes of operation, with an MPD of 8 cm, the data is sampled at 0.0625 cm^{-1} intervals.

This resolution is degraded somewhat by convolution with the ILS, which, due to a finite FOV, results in incoming rays being not quite parallel and travelling slightly different path lengths through the instrument, introducing contributions from far away lines. These contributions can be mostly suppressed by a process known as apodisation, using the Norton-Beer strong function (Norton and Beer, 1976) which is applied numerically to the spectrum. As a result, spectral resolution is degraded to around 0.05 cm^{-1} , in the FR mode, and correlations are introduced between the spectral elements. The process of apodisation is illustrated in figure 1.5.

1.1.5 Data processing

The MIPAS processing chain, which is overseen by ESA, may be summarised as follows;

- **level 0:** Time-ordered, reformatted data ready for computer processing.

- **level 1A:** Reconstructed interferograms.
- **Level 1B:** Calibrated and geolocated spectra derived from interferograms.
- **Level 2:** Retrieved profiles of the operational products, namely: pressure, temperature, H₂O, O₃, CH₄, HNO₃, N₂O and NO₂. See section 1.7.2 for a brief description of the retrieval methods used.

In this thesis, we use ‘Offline’ Level 1B data as well as Level 2 data. ¹

1.1.6 Changes to the mission plan

Fourier transform spectrometers are mechanically complex but offer the high spectral resolution and good radiometric sensitivity necessary for the discrimination of a wide variety of weakly emitting trace species. Despite a long history of ground, aircraft and balloon-based missions, in particular the balloon-based MIPAS-B (Friedl-Vallon et al., 2004), the forerunner of MIPAS-ENVISAT, the engineering challenges of operating a cooled infra-red FTS in space, mainly relating to the stability of the platform and the demanding optical performance, mean that MIPAS is one of the few to be flown and, indeed, has not been without problems.

The smooth running of the interferometer mirrors, which perform millions of cycles back and forth over the lifetime of the instrument, has proved crucial. In order to record a useful interferogram, the interference modulated output must be recorded at a sampling accuracy of around 30nm of path difference out of an MPD of 20 cm. This is achieved using a laser which is directed through the same optical set-up as the measured

¹The level 1B data is split into near-real-time (NRT) data, which becomes available hours after acquisition, and ‘Offline’ data products which take longer to become available. The ‘Offline’ products have better calibration and geolocation.

radiance and is used to trigger the sampling electronics behind the detectors at precise increments. The integrity of this sampling rate depends upon the smoothly varying velocity of the interferometer mirrors, which must be kept constant to within an accuracy less than 1% (Endemann, 1999). Despite operating without problems for more than 18 months, at the end of March 2004 it was noticed that velocity errors were exceeding this tolerance, with these effects eventually being attributed to problems with the functioning of the interferometer slide mechanism. The original FR mode of operation, with an MPD of 20 cm^{-1} , was revised and it was decided that a shorter MPD of 8 cm^{-1} would be used, decreasing spectral resolution to about 40 % of its optimal value but, in its favour, also decreasing measurement time and offering the potential for increased vertical and horizontal coverage of the atmosphere.

The instrument was switched off for several months during which time the MIPAS engineering team worked to diagnose hardware problems, propose engineering solutions, suggest revised measurement modes, and to implement and test the changes that would be necessary. The instrument was switched back on and tested in August 2004 at the reduced resolution using the original scan pattern and then later, in January 2005, measurements commenced using a suite of reduced resolution modes with a variety of scan patterns, offering high altitude measurements as well as measurements with increased vertical resolution in the UTLS. Although the cause of the slide errors remains unknown, warming the temperature of the slides appears to have produced a significant improvement. As a precaution, the instrument was initially rested for extended periods, leaving long data gaps, but the time during which the instrument is left idle has been gradually decreased as confidence in its performance has grown.

There have been some additional problems relating to ice formation on the detectors which occasionally requires decontamination by warming the instrument.

1.2 Radiative Transfer

The atmosphere absorbs, emits and scatters radiation according to its temperature and the gases and aerosols present. In the infra-red, absorption and emission involves the vibrational-rotational transitions of the gas molecules. In the absence of clouds, scattering in the infra-red is small and can be neglected.

For a certain path through the atmosphere, the radiance arriving at the satellite can be thought of as the radiance transmitted from one end of the path plus emission emanating from along the path. Under conditions of local thermodynamic equilibrium (LTE), emission at any point along the path is described by the Planck function at the local kinetic temperature

$$J(\nu, T_k) = B(\nu, T_k) = 2hc^2\nu^3 \left[\exp\left(\frac{hc\nu}{kT_k}\right) - 1 \right]^{-1} \quad (1.2)$$

Under certain conditions, the energy level populations are no longer described by the Boltzmann distribution and conditions of LTE no longer apply. A more general source function may be defined, which allows for a non-Boltzmann distribution of the energy level populations but reduces to the Planck function under LTE

$$J(\nu, T_K) = B_\nu r_2 \frac{\bar{k}_\nu}{k_\nu}; \quad \frac{k_\nu}{\bar{k}_\nu} = r_1 \left[\frac{1 - \Gamma r_2 / r_1}{1 - \Gamma} \right] \quad (1.3)$$

where r_1 and r_2 are the non-LTE to LTE population ratios of the levels

denoted 1 and 2, \bar{k}_ν is the LTE absorption coefficient, k_ν is the non-LTE adjusted absorption coefficient and Γ is the Boltzmann exponential factor given by $\Gamma = \frac{g_1}{g_2} \exp\left(\frac{-h\nu_0}{kT_k}\right)$.

Transmittance from a point x_s along the path to the instrument at x_{obs} for the monochromatic case is given by

$$\tau(\nu, x_s, x_{obs}) = \exp\left(-\int_{x_s}^{x_{obs}} \sum_i k_i(\nu, x) \rho_i(x) dx\right) \quad (1.4)$$

where $k_i(\nu, x)$ is the absorption coefficient for the i 'th absorber and $\rho_i(x)$ is the absorber density. The radiance arriving at the instrument from a path extending to the source at x_s is then given by

$$L(\nu, x_{obs}) = L(\nu, x_s) \tau(\nu, x_s, x_{obs}) + \int_{x_s}^{x_{obs}} J(\nu, T_k(x)) \frac{\partial \tau(\nu, x, x_{obs})}{\partial x} dx \quad (1.5)$$

In limb-sounding, $L(\nu, x_s)$ is emission from cold-space, and so this term can be neglected, in which case the radiance observed at the instrument at a particular wavenumber is given by

$$L(\nu, x_{obs}) = \int_{x_s}^{x_{obs}} J(\nu, T_k(x)) \tau(\nu, x_s, x_{obs}) \sum_i k_i(\nu, x) \rho_i(x) dx \quad (1.6)$$

1.3 Forward models

In the context of the MIPAS instrument, the forward model simulates the infra-red radiative transfer through the atmosphere and measurement process to provide simulated MIPAS measurements for given atmospheric conditions and instrumental parameters.

1.3.1 RFM

The Reference Forward Model (RFM) is used in the MIPAS Orbital Retrieval using Optimal Estimation (MORSE) system. The RFM was developed mainly by A. Dudhia at the University of Oxford under an ESA contract to provide reference spectral calculations for MIPAS-ENVISAT. It is a line-by-line radiative transfer model written in Fortran-77 based on the general purpose line-by-line atmospheric transmittance and radiance model (GENLN2) (Edwards, 1992). The RFM does not consider scattering, which is negligible at infra-red wavelengths in the absence of clouds. Its functionality has been widely extended, with the most recent additions including non-LTE spectral calculations and emission calculations for isotopic species (see RFM Manual Dudhia, 2008b, Internet).

1.3.2 GRANADA

The Generic non-LTE populations model (GRANADA) (Funke et al., 2002) for MIPAS-ENVISAT data, was developed at the Instituto de Astrofísica de Andalucía (IAA) in Granada. It is used in chapter 3 for various calculations of non-LTE radiative transfer. The model allows for the treatment of non-LTE effects in the retrieval of trace gas abundances and temperature, as well as for the retrieval of non-LTE specific parameters such as chemical and collisional rate constants (Funke et al., 2002).

1.4 Retrieval methods

Whenever direct measurements are difficult, it may be possible to use remote, or indirect, measurements, although they often bring in their wake complex problems of interpretation known as *Inverse Problems* (Rodgers,

2000). Satellite-based measurements provide almost simultaneous global measurements of atmospheric parameters which would be virtually impossible to obtain *in situ*. However, the electromagnetic radiation emerging from the atmosphere is some complicated function of the parameter actually required, for example the vertical distribution of VMR, and in addition depends on many other parameters relating to the state of the atmosphere and instrument. We are faced with the problem of setting up and solving a set of complicated simultaneous equations relating the parameter of interest to the observations. In cases where a solution exists, such problems are often ill-conditioned meaning that small errors in the observations lead to large errors in the solutions. To make things worse, in many real life situations the equations are often non-linear. In order to deal with such problems, they must first be reformulated, along with various assumptions, so that numerical solutions may be found.

The general approach to the solution of the inverse problem in remote sounding begins with the construction of the forward model. This model represents the state of the atmosphere and also the measurement process. In the retrieval, statistical estimation techniques are then used to fit the output of the forward model, the simulated measurements, to the real measurements. The estimate of the unknowns is then updated until the fit of the simulated measurements with the real measurements satisfies some pre-defined criteria. We begin our explanation of these techniques by outlining some key concepts and definitions within the context of the MIPAS instrument following Rodgers (2000).

1.4.1 Definitions

Measurement and state vectors

The measurement vector, \mathbf{y} , corresponds to a set of m spectral measurements. The state vector, \mathbf{x} , corresponds to the unknown parameters. This most often represents temperature and pressure or VMR given altitudes. However, the elements of the state vector are not limited to these characteristics but may also include a range of different types of parameter, providing that these can be altered within the forward model. For example, radiometric offset of the detector or vibrational temperature (a parameterisation of non-LTE effects) may also be included.

Forward model

We assume that the forward model represents the atmosphere and measurement process perfectly such that

$$\mathbf{y} = \mathbf{F}(\mathbf{x}, \mathbf{b}) + \epsilon \quad (1.7)$$

where \mathbf{y} is the measurement vector, \mathbf{F} represents the forward model, ϵ is the random experimental error due to instrument noise, \mathbf{x} is the state vector and \mathbf{b} represents the many other parameters not being retrieved but which influence the measurement such as spectral line shape and non-target species.

Weighting functions

The weighting functions describe the sensitivity of the forward model to alterations in the unknown quantity, \mathbf{x} . If the problem is not too non-linear then the forward model may be linearised about some reference state \mathbf{x}_0 , in which case

$$\mathbf{y} - \mathbf{F}(\mathbf{x}_0) = \left. \frac{\partial \mathbf{F}}{\partial \mathbf{x}} \right|_{x_0} (\mathbf{x} - \mathbf{x}_0) + \epsilon \quad (1.8)$$

The matrix $\partial \mathbf{F} / \partial \mathbf{x}|_{x_0}$ is the weighting function matrix, \mathbf{K} , or jacobian, and contains the partial derivatives of each forward model element with respect to each element of the state vector. It is an $m \times n$ matrix such that

$$\mathbf{K} = \left. \frac{\partial \mathbf{F}}{\partial \mathbf{x}} \right|_{x_0} = \begin{pmatrix} \frac{\partial F_1}{\partial x_1} & \frac{\partial F_1}{\partial x_2} & \cdots \\ \frac{\partial F_2}{\partial x_1} & \ddots & \\ \vdots & & \end{pmatrix} \quad (1.9)$$

Covariance matrix

For a general vector \mathbf{a} containing n random variables, the covariance matrix, \mathbf{S} may be defined

$$\mathbf{S}_{ij} = E(a_i - \bar{a}_i)(a_j - \bar{a}_j) \quad (1.10)$$

where the operator E gives the expectation value of repeated measurements and the bar notation indicates the mean value. The diagonal elements of \mathbf{S} give the variance in \mathbf{a} and the off-diagonal elements give the covariance between the different elements of \mathbf{a} . The correlation coefficients between elements of \mathbf{a} are then given by the covariance normalised by appropriate variances; $\mu = \frac{S_{ij}}{\sqrt{S_{ii}S_{jj}}}$

1.4.2 Unconstrained least-squares solution

In the over-constrained case, where there are more measurements than unknowns, the problem may be well-conditioned in which case a least squares fit of the forward model to the measurements is suitable, whereby

we minimise $\sum_i (y_i - K_i x_i)^2$. In its simple form it is largely unbiased, since there are no *a priori* constraints although, because of this, the solution can be prone to instabilities. The least-squares solution is given by the minimisation the cost function

$$\chi^2 = (\mathbf{y} - \mathbf{K}\mathbf{x})^T \mathbf{S}_y^{-1} (\mathbf{y} - \mathbf{K}\mathbf{x}) \quad (1.11)$$

where \mathbf{S}_y is the random measurement error covariance determined by instrument noise. The solution is given by

$$\mathbf{x} = (\mathbf{K}^T \mathbf{S}_y^{-1} \mathbf{K})^{-1} \mathbf{K}^T \mathbf{S}_y^{-1} \mathbf{y} \quad (1.12)$$

with a retrieval error given by

$$\mathbf{S}_x = (\mathbf{K}^T \mathbf{S}_y^{-1} \mathbf{K})^{-1} \quad (1.13)$$

For moderately non-linear cases, an iterative form is used (Raspollini et al., 2006)

$$\mathbf{x}_{i+1} = \mathbf{x}_i + (\mathbf{K}_i^T \mathbf{S}_y^{-1} \mathbf{K}_i + \lambda \mathbf{I})^{-1} \mathbf{K}_i^T \mathbf{S}_y^{-1} \mathbf{K}_i \quad (1.14)$$

where \mathbf{I} is the identity matrix and λ is the Levenberg-Marquardt factor, which controls the amplitude of the iteration steps to ensure convergence is reached, see section 1.4.6. This type of retrieval is used in the operational MIPAS level 2 processing at full spectral resolution (IPF 4.61/4.62).

1.4.3 Regularised least-squares solution

Because of oversampling of the profile in UTLS region in the RR modes, unphysical oscillations are intrinsic to the retrieved profiles unless external constraints are introduced into the retrieval process. Tikhonov type *a posteriori* regularisation is applied introducing an operator \mathbf{R} constraining the solution towards some selected feature, i.e., a value or shape of the *a priori* state (Carlotti et al. (2005), Carlotti et al. (2006))

$$\mathbf{x}_{i+1} = \mathbf{x}_i + [\mathbf{K}_i^T \mathbf{S}_x^{-1} \mathbf{K} + \lambda \mathbf{I} + \mathbf{R}]^{-1} [\mathbf{K}_i^T \mathbf{S}_x^{-1} (\mathbf{x}_i - \mathbf{x}_a) - \mathbf{R}(\mathbf{x}_i - \mathbf{x}_a)] \quad (1.15)$$

This type of retrieval algorithm is currently being implemented in the ESA level 2 operational processor for reduced resolution modes (IPF 5). This type of regularization is already implemented in the IMK (Institut für Meteorologie und Klimaforschung) scientific processor (Stiller et al., 2003).

1.4.4 Optimal estimation

Optimal estimation is a least-squares method which considers an *a priori* estimate of the state in addition to the spectral measurements to constrain the possible outcomes. It is useful in the case of an ill-conditioned problem, where small errors in the measurements lead to large errors in the solution. The Oxford level 2 processor MORSE (MIPAS Orbital Retrieval using Sequential Estimation) works on this basis. Specific features of MORSE are described in section 1.7.1.

If we assume that \mathbf{x}_a and \mathbf{x} are described by Gaussian statistics, then we can arrive at an expression for the most probable state $\hat{\mathbf{x}}$ by

minimising the following cost function²

$$\chi^2 = (\mathbf{y} - \mathbf{K}\mathbf{x})^T \mathbf{S}_y^{-1} (\mathbf{y} - \mathbf{K}\mathbf{x}) + (\mathbf{x} - \mathbf{x}_a)^T \mathbf{S}_a^{-1} (\mathbf{x} - \mathbf{x}_a) \quad (1.16)$$

which yields an expression for the most probable state

$$\hat{\mathbf{x}} = \mathbf{x}_a + (\mathbf{K}^T \mathbf{S}_y^{-1} \mathbf{K} + \mathbf{S}_a^{-1})^{-1} \mathbf{K}^T \mathbf{S}_y^{-1} (\mathbf{y} - \mathbf{K}\mathbf{x}_a) \quad (1.17)$$

where \mathbf{x}_a is the prior estimate of the state and \mathbf{S}_a is its covariance. $\partial \hat{\mathbf{x}} / \partial \mathbf{y} = (\mathbf{K}^T \mathbf{S}_y^{-1} \mathbf{K} + \mathbf{S}_a^{-1})^{-1} \mathbf{K}^T \mathbf{S}_y^{-1}$ is known as the gain matrix, \mathbf{G} , or the measurement contribution function. The solution covariance, which is the combination of the propagation of instrument noise through the retrieval and the *a priori* covariance is given by

$$\mathbf{S}_{\hat{\mathbf{x}}} = (\mathbf{K}^T \mathbf{S}_y^{-1} \mathbf{K} + \mathbf{S}_a^{-1})^{-1} \quad (1.18)$$

The optimal solution can be thought of as an average of the measurements and *a priori* estimate weighted according to the uncertainties on each.

1.4.5 Retrieval diagnostics

The χ^2 test

The χ^2 test is a way of testing whether a particular random vector belongs to a given Gaussian distribution (Rodgers, 2000). A multivariate

²In a scalar example, this corresponds to maximising the joint probability of the true state x given the prior estimate x_a , along with the forward model mapping of the true state $F(x)$ given the spectral measurements y , assuming Gaussian probability distributions: $P(x|x_a)P(y|F(x)) \propto \exp\left(-\left[\frac{(x-x_a)^2}{\sigma_x^2} + \frac{(y-F(x))^2}{\sigma_y^2}\right]\right)$. We are essentially minimising the misfit function, given by the argument of the exponential, to find the most probable state \hat{x} .

Gaussian distribution with n degrees of freedom is given by:

$$P_n(\chi^2)d\chi^2 = \frac{1}{\Gamma(n/2)} \left(\frac{1}{2}\chi^2\right)^{\frac{n}{2}-1} \exp\left(-\frac{1}{2}\chi^2\right) \quad (1.19)$$

Such a distribution has the property that the expectation value of the cost $E(\chi^2) = n$. Therefore, if Gaussian statistics hold, which may be a rather loose assumption, the cost normalised by the number of state vector elements should equal one. The value of χ^2 is therefore commonly used as a retrieval diagnostic, and in iterative methods, as an indicator of convergence. The value obtained depends upon how well the forward model represents the real physics, our estimate of the error on the measurements and on the *a priori*. Values which are much higher, or lower, than expected may point to some problem with the measurements, or an incorrect assumption about the retrieval.

Averaging kernels

Averaging kernels describe how the true state of the atmosphere has been distorted by the retrieval

$$\hat{\mathbf{x}} = \mathbf{A}\mathbf{x}$$

They are the rows of the matrix \mathbf{A}

$$\mathbf{A} = \mathbf{I} - \mathbf{S}_x\mathbf{S}_a^{-1} \quad (1.20)$$

These are peaked functions with a half width that provides a measure of the spatial resolution of the observations. The area of the averaging kernel is roughly unity where the retrieval is accurate and can be thought of as a rough measure of the fraction of the retrieval that comes from the

data rather than the *a priori* estimate (Rodgers, 2000).

Shannon information content

Shannon information content is a scalar quantity originally conceived to describe the information carrying capacity of communications channels (Shannon and Weaver, 1962). It is also a useful quantity for the optimisation of observing systems. The information content of a measurement can be defined qualitatively as the factor by which knowledge of a quantity is improved by making the measurement (Rodgers, 2000), usually expressed in terms of bits. For the linear Gaussian problem, it may be calculated as

$$H = \frac{1}{2} \ln |\mathbf{S}_{\hat{\mathbf{x}}}^{-1} \mathbf{S}_a| \quad (1.21)$$

Sequential estimation

The MORSE algorithm uses sequential estimation. In the optimum estimation version, the retrieved state vector from one set of measurements is incorporated as the *a priori* estimate during the inversion of the subsequent set. An equivalent solution can be obtained without needing to invert all measurements simultaneously which significantly improves memory efficiency, mainly through the reduction in size of the weighting function matrix. The solution is calculated sequentially by profile level, beginning at the top of the atmosphere, incorporating values retrieved at previous tangent heights to update the *a priori* estimate. Similarly, microwindow information is processed sequentially for a given gas. Finally, contaminant species are retrieved sequentially in the order of greatest contribution to radiance in a given spectral interval.

1.4.6 Iterative methods

The Gauss-Newton method

In the more general case of a moderately non-linear problem, the optimal solution cannot be found directly using equation 1.17 but must be located iteratively. The simplest approach is to advance the solution in the direction of steepest descent, $-\nabla_x \chi^2$, but in non-linear cases this does not necessarily point towards the minimum of cost. When the problem is not too non-linear, a Newtonian iteration should advance the solution in the right direction

$$\mathbf{x}_{i+1} = \mathbf{x}_a + (\mathbf{S}_a^{-1} + \mathbf{K}_i^T \mathbf{S}_y^{-1})^{-1} \mathbf{K}_i^T \mathbf{S}_y^{-1} [\mathbf{y} - \mathbf{F}(\mathbf{x}_i) + \mathbf{K}_i(\mathbf{x}_i - \mathbf{x}_a)] \quad (1.22)$$

For convenience, the initial guess \mathbf{x}_0 is commonly chosen to be equal to the *a priori* estimate \mathbf{x}_a .

Levenberg-Marquardt method

The Levenberg-Marquardt method introduces a tunable damping factor into the variation of the unknown. It is used when the iterative process is unstable, which may occur when there is a significant degree of non-linearity or when the iterative process begins far from the true solution. In such cases, the Gauss-Newton step can result in an increase rather than a decrease in cost. The Levenberg-Marquardt iteration may be expressed

$$\mathbf{x}_{i+1} = \mathbf{x}_i + [(1 + \gamma)\mathbf{S}_a^{-1} + \mathbf{K}_i^T \mathbf{S}_y^{-1} \mathbf{K}_i]^{-1} (\mathbf{K}_i^T \mathbf{S}_y^{-1} [\mathbf{y} - \mathbf{F}(\mathbf{x}_i)] - \mathbf{S}_a^{-1} [\mathbf{x}_i - \mathbf{x}_a]) \quad (1.23)$$

Through adjustment of the tunable parameter γ , the iteration is nudged out of the local minimum of cost so that the retrieval may progress towards the true solution. In cases where χ^2 increases, γ is decreased, tending towards steepest descent, and the iteration is repeated without updating \mathbf{x}_i . In cases where χ^2 decreases, γ is decreased, tending towards a Gauss-Newton step, and \mathbf{x}_i is updated.

Convergence criteria

Suitable convergence criteria are required such that the iterations are stopped when the retrieved state is as close as possible to the supposed true state. A common method is to compute the change in the χ^2 value from the previous iteration

$$\chi_n^2 = \frac{1}{n}(\mathbf{x}_{i+1} - \mathbf{x}_i)^T \mathbf{S}_x (\mathbf{x}_{i+1} - \mathbf{x}_i) \quad (1.24)$$

where \mathbf{S}_x is the updated covariance of the atmospheric state \mathbf{x}_{i+1} . Iterations are stopped when the decrease in χ^2 is less than some predefined value which tries to ensure that the residual spectra, $\mathbf{F}(\mathbf{x}) - \mathbf{y}$, are of the same order of magnitude as instrument noise. When the residuals are due to purely random noise, normalised χ^2 approaches a value of 1. It is useful to check the absolute value of χ^2 on the current iteration to ensure that the retrieval has not settled in a local minimum of cost far from the true solution.

1.5 Microwindow selection

The methods used to select optimal subsets of the spectrum, known as microwindows, are described in detail in Dudhia et al. (2002). Spectral regions are selected which maximise information about the target

Error Source	1 σ
<i>Errors in instrument characterisation</i>	
Radiometric gain	$\pm 2\%$
Apodised ILS width	$\pm 1\%$
Spectral calibration	$\pm 0.001 \text{cm}^{-1}$
<i>Errors in forward model parameters</i>	
Profiles of 28 gases	Climatological SD
High altitude column	Climatological SD
Line database errors	Accuracy of line params
Continuum model	$\pm 25\%$
Retrieved p error	$\pm 2\%$
Retrieved T error	$\pm 1\text{K}$
<i>Deficiencies in forward model</i>	
Non-LTE effects	Modelled
CO ₂ line mixing	Modelled
Horiz. T gradients	$\pm 1\text{K}/100 \text{ km}$

Table 1.1: Sources of systematic error typically considered and estimates of 1 σ uncertainty (adapted from Dudhia, A., ENVISAT Symposium, 2004).

species whilst minimising the contribution of systematic errors, such as overlapping lines from contaminant molecules, for example.

The propagation of systematic errors through the retrieval is modelled using the Reference Forward Model (RFM) to calculate the total measurement error covariance, given by the sum of the random and systematic components

$$\mathbf{S}_{y_{tot}} = \mathbf{S}_{y_{rnd}} + \sum \mathbf{S}_{y_{sys}}^i \quad (1.25)$$

Sources of systematic error typically considered are listed in table 1.1. The total measurement error is then mapped through the retrieval to give the total retrieval error, \mathbf{S}_x . Microwindows are grown using adjacent spectral points which minimise the total retrieval error. Figure 1.6 illustrates the process of growing microwindows in spectral-altitude space. Each new point is accepted or rejected based on the information content

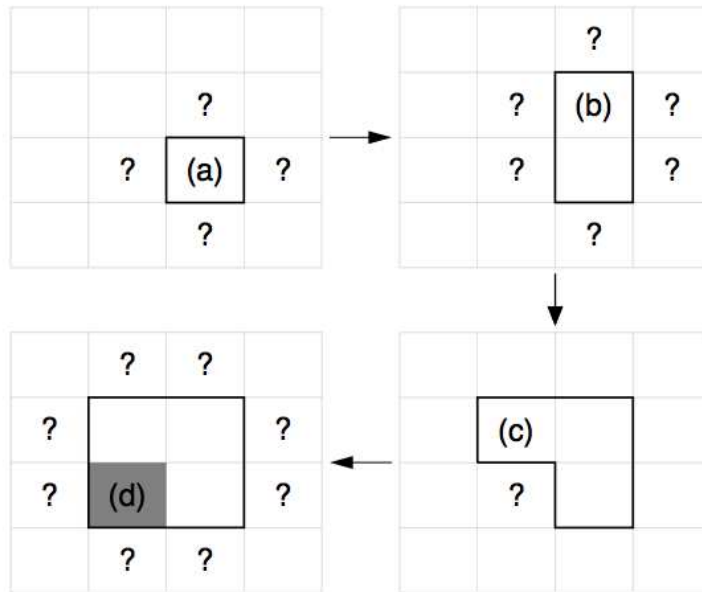


Figure 1.6: The process of growing microwindows on a spectral-altitude grid (Dudhia et al., 2002)

of the microwindow

$$H = \frac{1}{2} \ln |\mathbf{S}_{x_{\text{tot}}}^{-1} \mathbf{S}_a| \quad (1.26)$$

including points which maximise this value. CPU cost is also considered during the selection of operational microwindows.³

1.6 Background continuum

In addition to the spectral features of the target species, the MIPAS level 1b spectra also contain a spectrally smooth baseline signal, or continuum, which arises from a variety of effects related to the instrument, atmosphere and forward model. This baseline contribution is difficult to determine as it arises from various unknown sources, for example:

³Not considered for the selection of microwindows in RR retrievals (*A. Dudhia personal communication*).

- **Instrumental effects:** uncertainties in the self-emission of the instrument, stray light, uncertainties in detector non-linearity, as well as uncertainties introduced due to differences in the emission/reflectance properties of the scan mirror at different angles of incidence.
- **Cloud and aerosol particles:** contributions to radiance from cloud and aerosol can introduce a large continuum signal. Contaminated spectra are generally removed by performing a cloud threshold test. The simplest and most commonly used test is the cloud index (CI) method. It is based on the ratio of integrated radiance between an optically thick (cloud insensitive) and optically thin (cloud sensitive) microwindow. The A-band cloud insensitive microwindow is situated at $788.20\text{--}796.25\text{ cm}^{-1}$, and the cloud sensitive microwindow is situated at $832.3\text{--}834.4\text{ cm}^{-1}$. According to Spang et al. (2004), a CI threshold > 1.8 removes spectra with significant cloud contamination. However, cloud contamination is possible at higher CI values. A CI of 4–5 indicates thin cloud, or a situation where cloud covers only part of the FOV. In this situation, trace gas retrievals are possible but some residual continuum signal is expected.
- **Forward model uncertainties:** uncertainties in the continuum emission of H_2O , O_2 and N_2 also contribute to the baseline signal, particularly at low altitudes.

The spectral features of the target gas are superimposed upon this flat baseline signal, and a separate continuum extinction coefficient is retrieved in order to quantify its contribution. Equation 1.27 shows how terms are included into the 1-D radiative transfer equation to quantify

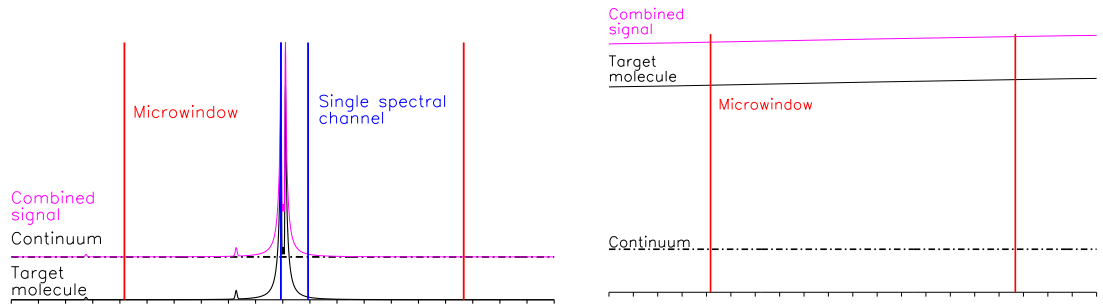


Figure 1.7: Separating the contribution of the target gas from the background continuum for narrow and broad spectral features. (Width of microwindow not to scale).

absorption and emission from this background continuum

$$\frac{dL}{dz} = -(k_{\text{gas}} + k_{\text{ctm}})nL + (k_{\text{gas}} + k_{\text{ctm}})nB + R_{\text{off}} \quad (1.27)$$

where k_{gas} and k_{ctm} are the extinction coefficients for the target gas and background continuum respectively, R_{off} is a constant offset term, and n is the target gas number density, for radiance emerging from some point in the atmosphere at a particular wavelength. The absolute value of continuum extinction is unknown since it originates from uncertainties in the forward model calculations and spectroscopic data, as well as from unknown atmospheric and instrumental contributions. However, as illustrated in figure 1.7, only the relative contribution of the target species with respect to the continuum is needed. This is easily achieved for narrow gas lines where, by using a spectral region wider than the target line, its relative contribution can be fixed. However, for broad spectral features such as N_2O_5 , the typical width of a single microwindow is not sufficient to isolate its contribution. In this case, separating the target signal from the baseline signal consists of determining the absolute value of the continuum, which cannot in general be ascertained. Instead, the

range of altitudes is reduced to limit the continuum contribution, or else a wider spectral region is used so that the contribution of the target species relative to the baseline can be determined.

1.7 Retrieval algorithms

1.7.1 MORSE

MIPAS Orbital Retrieval using Sequential Estimation (MORSE) is a Fortran-77 retrieval code mainly developed by A. Dudhia at the University of Oxford (MORSE Manual Dudhia, 2008a, Internet). The retrieval is based on an optimal estimation scheme and uses *a priori* estimates of the state derived from the IG2 Climatology by Remedios et al. (2007) to constrain the solution. This type of retrieval is naturally suited to the ill-conditioned problem that arises for weakly emitting species or due to oversampling in the reduced resolution modes. A relatively simple adaptation could be applied which allowed retrievals to be performed on different altitude grids for use with both full and reduced resolution data (version 3). The algorithm minimises a cost function, employing Gauss-Newton Levenberg Marquardt iterations to deal with the non-linear problem. Retrievals are performed sequentially to optimize memory efficiency. Spectra at each tangent height are processed sequentially beginning at the top tangent altitude. Microwindow information is also processed sequentially. Contaminant species are retrieved sequentially beginning with a joint retrieval of pressure and temperature, followed by the contaminant species in order of importance. The RFM is used as the forward model. Cloud contaminated scans are identified using the cloud index method by Spang et al. (2004) and spectra with an A-band CI < 1.8 are removed. If the CI test in band A fails, then alternative CI tests in band B or D are

performed. There is also a radiance threshold test in a cloud detection channel situated at 960.7 cm^{-1} whereby sweeps with a threshold value of $< 125 \text{ nWcm}^{-2}\text{sr}^{-1}\text{cm}$ are assumed to be cloud free. A spectrally varying background continuum extinction term, which mostly accounts for the presence of thin cloud, aerosol and poorly modelled line wings, is retrieved jointly with the target species. A radiometric offset term that is constant with altitude is also retrieved.

1.7.2 MIPAS level 2 operational analysis

The MIPAS level 2 operational analysis performed by ESA uses an unconstrained non-linear least-squares method with a Gauss-Newton Levenberg-Marquardt iterative procedure. Microwindows are used that have been optimised for the target species as described in section 1.5. The forward model used is the Optimized Forward Model (OFM) (Ridolfi et al., 2000). The measurements in each scan are inverted globally fitting the spectra at all heights simultaneously. Cloud contaminated spectra with an A-band CI < 1.8 are removed. The retrieval of the standard species (p, T, H₂O, O₃, N₂O, NO₂, HNO₃) is sufficiently well-conditioned in the full resolution mode, and regularisation and *a priori* information are not necessary for a stable retrieval (Raspollini et al., 2006). However, oversampling of the profile in the UTLS in the new reduced resolution modes results in an ill-conditioned problem requiring some form of regularisation. A Tikhonov type regularisation was proposed, as described in section 1.4.3, requiring significant changes to the operational processor. These changes are still being implemented and tested and have resulted in significant delays in the delivery of the ESA operational level 2 product for the reduced resolution modes.

Chapter 2

Impact of new measurement modes

2.1 Introduction

The spectral resolution and vertical sampling of the MIPAS instrument have been drastically altered. From July 2002 until March 2004, the instrument operated at full spectral resolution (0.0250 cm^{-1}) with 3 km vertical spacing from 6–42 km, 5 km spacing up to 52 km, and 8 km spacing up to 68 km. The instrument was switched off for several months after a fault was detected in the interferometer slide mechanism towards the end of March 2004. Then in January 2005, after several months of detailed planning, regular measurements commenced using a shorter maximum path difference at a reduced spectral resolution (0.0650 cm^{-1}). The reduction in measurement time was exploited to introduce denser vertical sampling in the UTLS, with 1.5 km vertical sampling from 6–31 km, as well as high altitude measurement modes extending into the thermosphere. Further details about the problems encountered and subsequent changes to the mission plan can be found in section 1.1.6.

The new measurement modes bring benefits as well as disadvantages. The reduction in time taken to acquire the interferogram has allowed improved horizontal and vertical sampling of the atmosphere. However, the decrease in spectral resolution and oversampling of the atmospheric profile by the field-of-view leads to higher retrieval random errors. In addition, there have been significant practical difficulties associated with the adaptation of existing unconstrained retrieval algorithms, such as the ESA level 2 processor, to cope with oversampling in the vertical domain and subsequent ill-conditioning of the retrieval problem in the new measurement modes. In this respect, the MORSE algorithm, which works on the basis of optimal estimation, using a prior estimate of the atmospheric state to constrain the retrieval, has a natural advantage, and has required relatively few adaptations to cope with the new measurement scenarios. However, the selection of an optimal set of microwindows for the new measurement modes which minimise the propagation of systematic errors due to interference effects from contaminant species, instrumental and modelling errors presents an additional and on-going problem.

Since retrievals using both full and reduced resolution mode data are presented in this thesis, a study is required that investigates the effect of these changes. The molecules N_2O_5 and CO have been selected since they represent a best and worst case respectively due to their differing spectral shapes and are the subject of further investigation in chapters 4 and 3. The effect of changes in spectral resolution as well as vertical spacing of the retrieval and measurement grids are investigated using pure gas spectra modelled using the RFM. Then, in the final section, the propagation of systematic errors is described using operational microwindows for CO and N_2O_5 selected for the FR17 and RR27 measurement modes.

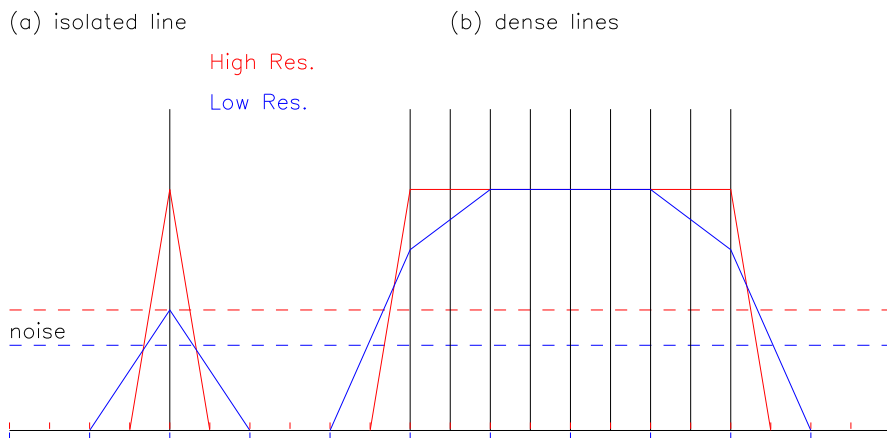


Figure 2.1: The effect of a reduction in spectral resolution for narrow and broad spectral features (Dudhia, 2005).

2.1.1 Impact of reduced spectral resolution

The impact of the change in spectral resolution differs depending on whether the spectral feature is broad or narrow. At high altitudes, CO lines are narrow and are generally close to the spectral resolution of the instrument. On the other hand, N_2O_5 is a more complex molecule, with many closely spaced transitions which appear as broadband continuum features. The effect of a reduction in spectral resolution on S/N for each case is illustrated in figure 2.1.1. The area under the feature remains constant. Therefore, the signal is reduced by R for the narrow feature but remains almost constant for the broad feature. The noise at each spectral point decreases by a factor \sqrt{R} where $R = 0.0250/0.0625$ due to the decrease in integration time at the reduced resolution. For the broad spectral feature, however, this noise advantage is lost as the number of spectral points encompassed decreases by a factor R when spectral resolution is degraded. Hence, to summarise, the limiting cases of S/N when the spectral resolution is decreased are:

- **Features up to ILS width:** S/N is reduced by a factor \sqrt{R} . For example, CO at high altitudes.

- **Features much wider than ILS:** S/N remains approximately constant. For example, N_2O_5 , CFC's and HCFC's.

Many molecules fall somewhere in between these two cases and the effects may be dependent on altitude. For CO, spectral features in the stratosphere are narrow but somewhat wider than the ILS, whereas in the troposphere, CO lines are significantly wider than the ILS due to the effects of pressure broadening. A brief investigation into the effect on CO signal in the stratosphere is presented. A CO line centred on 2165.6 cm^{-1} was modelled at the 30 km tangent height under nighttime LTE conditions at fine spectral resolution (0.0005 cm^{-1}) using the RFM. This spectral feature was then convolved with the apodised FR and RR ILSs. The convolved lines are shown in figure 2.2. The RR signal is 50% of the FR signal, rather than the $R \sim 40\%$ expected for very narrow features. This suggests that the anticipated factor \sqrt{R} degradation in retrieval precision may be overly pessimistic.

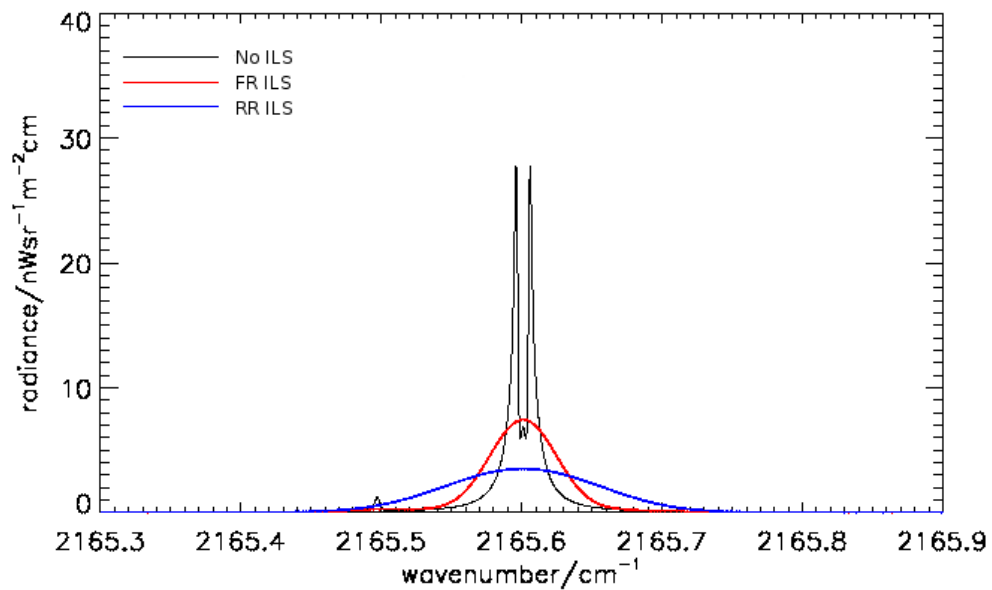


Figure 2.2: Modelled CO line convolved with the FR and RR apodised ILSs. Modelled line shows effects of saturation reflecting the temperature structure of the model atmosphere.

2.1.2 Impact of retrieval grid spacing

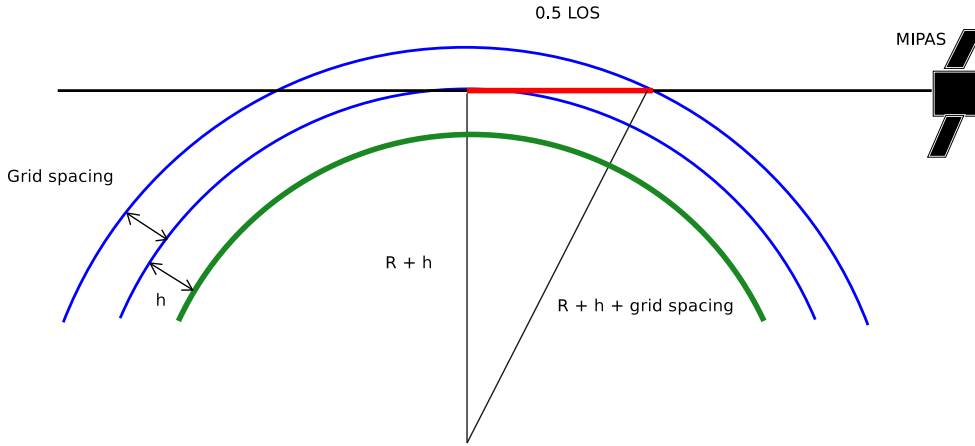


Figure 2.3: Relationship between path length perturbed in forward model and retrieval grid spacing.

Denser vertical sampling increases vertical resolution but reduces sensitivity to the retrieved quantity. For an FOV of negligible width, increasing vertical sampling density by a factor 2 results in a factor $\sqrt{2}$ reduction in the path length perturbed. This is illustrated in figure 2.3 where for the 3 km spacing, the line-of sight is given by: $\text{LOS}_{3km} = 2\sqrt{(R+3)^2 - R^2}$, and for the 1.5 km spacing, it is given by: $\text{LOS}_{1.5km} = 2\sqrt{(R+1.5)^2 - R^2}$, where $R \sim R+h$. The jacobians are correspondingly weaker and retrieval precision is degraded by approximately the same factor.

However, the vertical extent of the FOV is around 3 km. If the retrieval points are placed at the tangent altitudes using the 1.5 km measurement grid, correlations introduced between the levels act to worsen retrieval precision still further. Oversampling by the FOV also means that improvements in vertical resolution of the retrieval are less pronounced.

2.2 Random errors

The effect of decreased spectral resolution and oversampling in the vertical domain on random error is investigated using pure gas spectra. This investigation does not consider differences in the propagation of systematic errors, such as interference from contaminant species. Various measurement and retrieval grid scenarios are presented, namely retrievals using FR 17 data, RR17 data, RR27 data with retrieval points at the tangent altitudes, and RR27 data with more widely spaced retrieval points. The configurations examined are listed in table 2.1. An *a priori* standard deviation of 100% of the profile value is assumed in the calculation of the random error. Vertical correlations in the *a priori* estimate, which are typically introduced to stabilise the retrieved profile, resulting in smaller random errors and a smoothed vertical profile, have been omitted from the analysis, due to the somewhat arbitrary nature of selecting an appropriate correlation length scale.

2.2.1 CO

The effect of the new measurement modes is investigated for a standard CO retrieval. Measurements were simulated using the RFM for a mid-latitude CO only atmosphere in the 2135.000–2175.000 cm^{-1} spectral region, assuming LTE conditions.

FR 3km scan pattern, 3 km retrieval grid (A)

Figure 2.5 indicates that above 18 km, where the CO lines are very narrow, retrievals from the full spectral resolution data result in the best retrieval random error. Averaging kernels for the FR17 data are shown in figure 2.6(a). In the UTLS, integrated kernels are near unity indi-

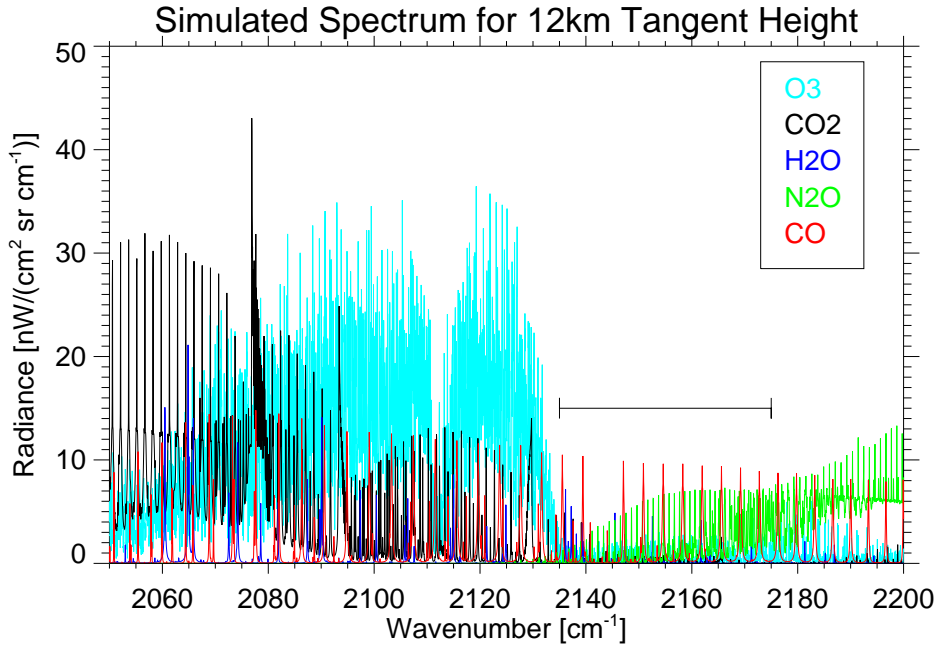


Figure 2.4: Mid-latitude nighttime CO spectrum and contaminant gases at 12 km, simulated at full spectral resolution using the RFM under LTE conditions. Bar indicates spectral region used in CO retrieval analysis (2135.000–2175.000 cm^{-1}).

Label	Spectral resolution [cm^{-1}]	Scan pattern	Retrieval grid	Operational mode
A	0.0250	3 km nominal	3 km nominal	FR17
B	0.0625	1.5 km nominal	1.5 km nominal	RR27
C	0.0625	1.5 km nominal	3 km nominal	RR27
D	0.0625	3 km nominal	3 km nominal	RR17

Table 2.1: List of scan pattern and retrieval grid configurations at full and reduced spectral resolution. Configuration A applies to data obtained July 2002–March 2004 (FR17), B and C to data from January 2005 onwards (RR27), and D to data during the August 2004 test period (RR17).

cating that nearly all the information is derived from the measurements rather than the *a priori*. However, retrieval sensitivity is poor at higher altitudes, and the *a priori* influence dominates the solution. Vertical resolution, defined as the FWHM of the kernels, is also shown in figure 2.6(a). Vertical resolution is 5 km in the upper-troposphere decreasing to 10 km in the upper-stratosphere.

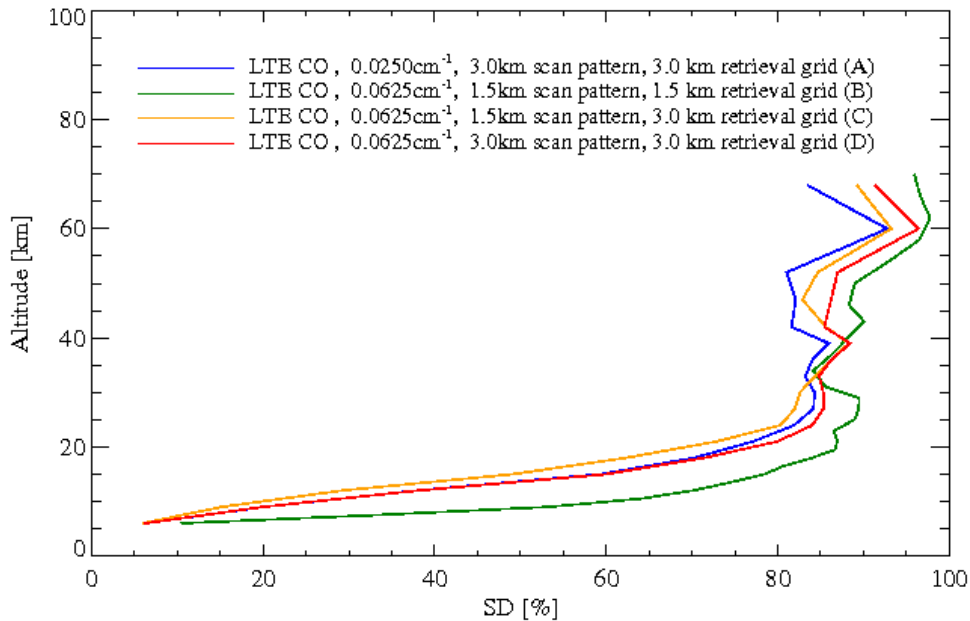
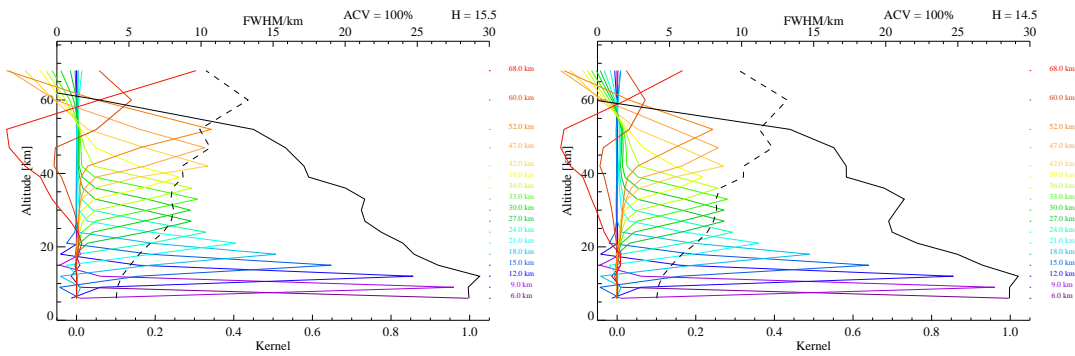


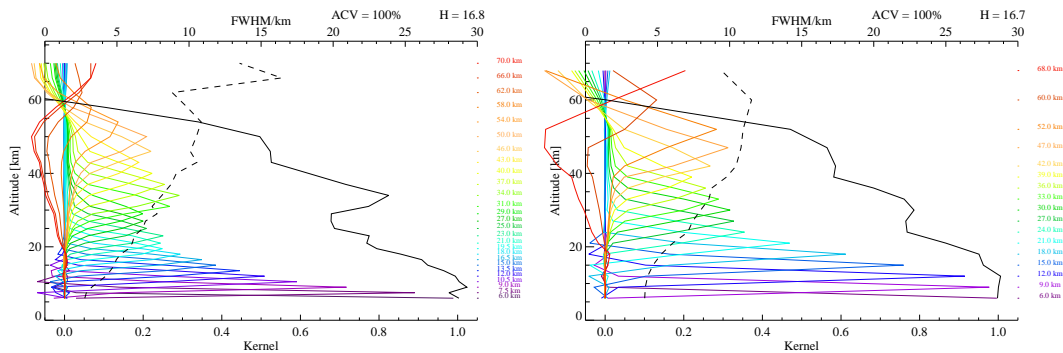
Figure 2.5: Simulated CO random error for the various retrieval and scan pattern configurations listed in table 2.1. An *a priori* standard deviation of 100 % of the profile value is assumed.

RR 3 km scan pattern, 3 km retrieval grid (D)

Comparison of cases A and D in figure 2.5 shows the effect of reducing spectral resolution on retrieval precision independent of changes in the grid spacing. There are negligible differences in the UTLS, where line width is significant due to Doppler broadening, but at higher altitudes, where lines are narrower, precision is significantly worse in the RR case. Averaging kernels for case D are shown in figure 2.6(b). As the retrieval grids in cases A and D are identical, the information content (H), also indicated in figures 2.6(a) and 2.6(b), is directly comparable. As expected, the information content of the RR retrieval ($H = 14.5$) is lower than in the FR case ($H = 15.5$).



(a) FR 3km nominal scan pattern and 3 km retrieval grid (A, table 2.1). (b) RR 3 km nominal scan pattern and 3 km retrieval grid (D, table 2.1).



(c) RR 1.5 km nominal scan pattern and 1.5 km retrieval grid (B, table 2.1). (d) RR 1.5 km nominal scan pattern and 3 km retrieval grid (C, table 2.1).

Figure 2.6: Simulated CO averaging kernels for configurations listed in table 2.1. Vertical resolution (FWHM) shown as dashed line. Integrated kernels shown as solid black line. *A priori* standard deviation (denoted ACV) set to 100%. Information content also indicated (H).

RR 1.5 km scan pattern, 1.5 km retrieval grid (B)

In the RR27 mode, retrieval random error is significantly worse when the retrieval points are placed at the tangent altitudes due to oversampling of the vertical profile by the FOV. Figure 2.5 shows that retrieval precision in case B is significantly worse than in the other cases at most altitudes. Furthermore, improvements in vertical resolution are modest. At 20 km, vertical resolution is improved by less than 10 %.

RR 1.5 km scan pattern, 3 km retrieval grid (C)

Significant improvements in retrieval random error can be obtained by using the finely gridded data and performing the retrieval at a coarser vertical resolution. Case C shows the effect of retrieving from the RR27 data at the FR17 tangent points. In the UTLS, retrieving on the FR17 grid effectively results in 2 spectra at each retrieval level, and this configuration results in the best retrieval precision, see figure 2.5. Averaging kernels are shown in figure 2.6(d). Comparing cases B and C shows the effect of changing only the retrieval grid spacing. Precision in case B, whereby retrieval points are spaced by 1.5 km in the UTLS, is worse than the predicted factor $\sqrt{2}$ degradation for an FOV of negligible width due to correlations introduced between profile levels by the 3 km FOV.

2.2.2 N₂O₅

We present an analogous analysis for N₂O₅ for the configurations listed in table 2.1. Measurements of N₂O₅ were simulated using the RFM between 1219.000–1239.000 cm⁻¹ as shown in figure 2.7 under mid-latitude nighttime conditions. Again, an *a priori* standard deviation of 100% is assumed throughout the profile with no vertical correlations.

FR 3 km scan pattern, 3 km retrieval grid (A)

Retrieval precision is shown in figure 2.8. Random errors of better than 30% are obtained in the mid-stratosphere, where N₂O₅ concentrations are at a maximum. However, there is very little signal in the mid-upper stratosphere, or in the troposphere, where concentrations of N₂O₅ are negligible, and random errors quickly tend to 100%. Averaging kernels are shown in figure 2.9(a). Integrated kernels are near unity in the mid-

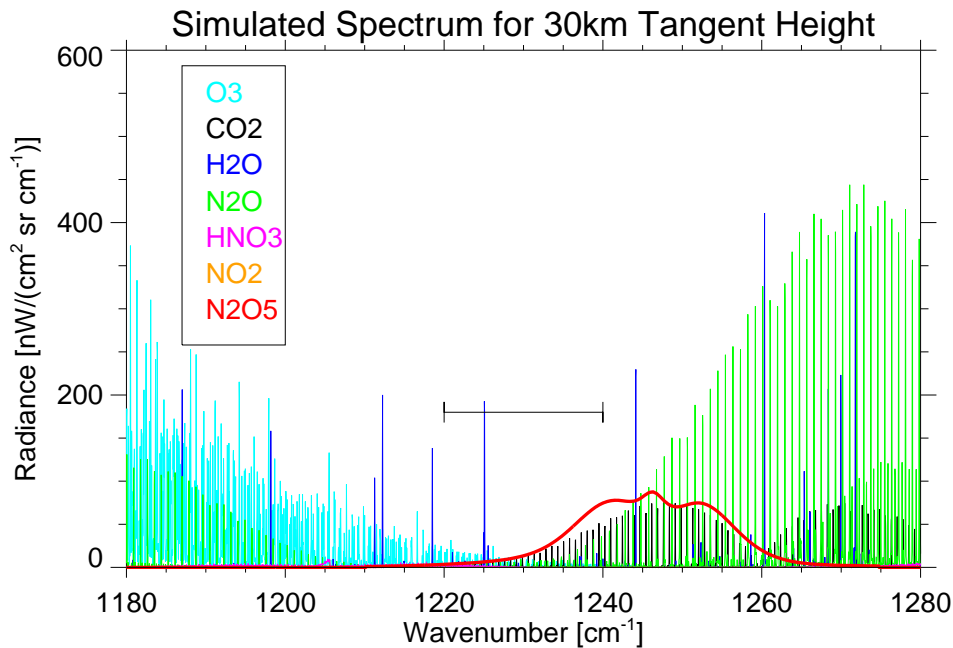


Figure 2.7: Mid-latitude nighttime N_2O_5 spectrum and contaminant gases at 30 km simulated using the RFM at full spectral resolution. Bar indicates spectral region used in analysis ($1219.000\text{--}1239.000\text{ cm}^{-1}$).

stratosphere. The kernels are strongly peaked in this region and vertical resolution of better than 5 km is possible.

RR 3 km scan pattern, 3 km retrieval grid (D)

For broad spectral features, there is little change in S/N when spectral resolution is reduced. Comparison of cases A and D in figure 2.8 confirms that there are only very small changes in retrieval precision at the reduced spectral resolution. Averaging kernels shown in figure 2.9(b) are almost indistinguishable from the full resolution case. There is also no significant difference in information content calculated for cases A and D.

RR 1.5 km scan pattern and 1.5 km retrieval grid (B)

Retrieval precision in case B is significantly worse than in other cases at low altitudes, see figure 2.8. Above this height differences are negligible

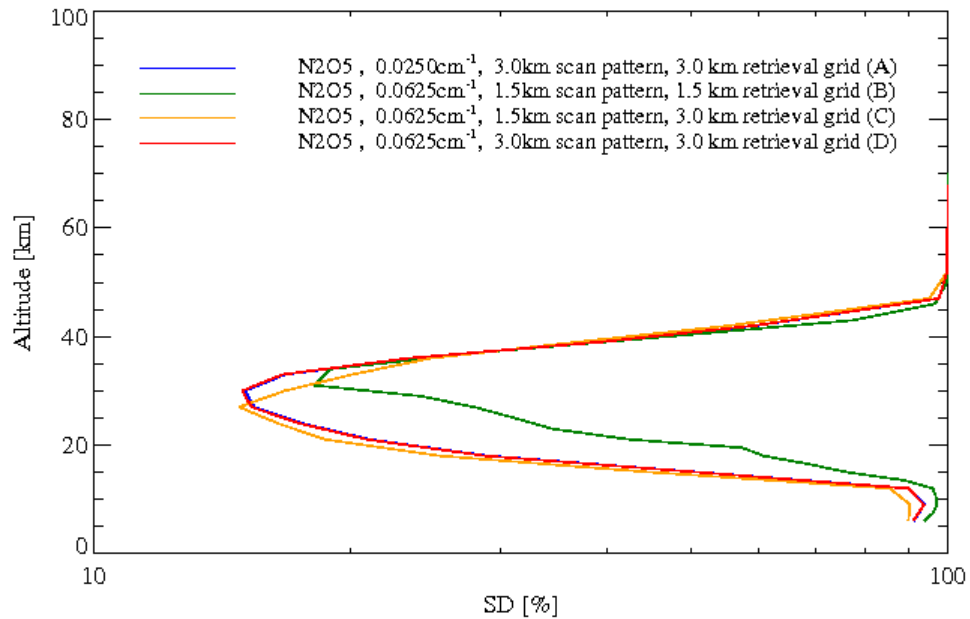


Figure 2.8: Retrieval random error for N₂O₅ simulated under mid-latitude nighttime conditions at full and reduced spectral resolution for the various scan patterns listed in table 2.1. An *a priori* standard deviation of 100% of the profile value is assumed.

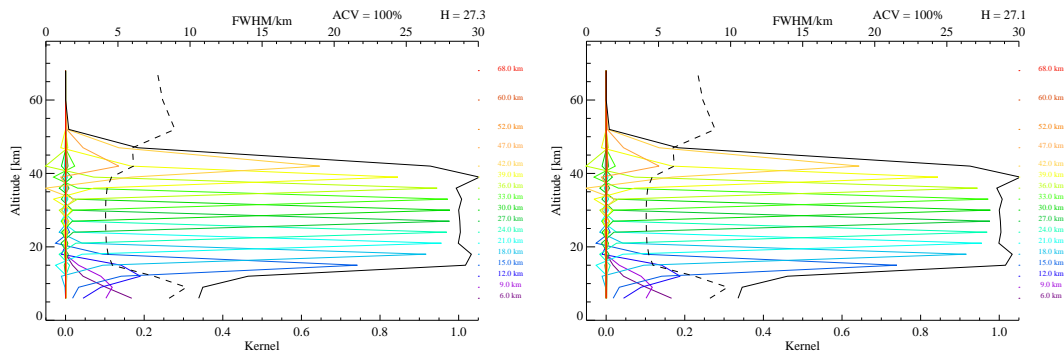
as the grid spacing becomes wider. Averaging kernels are shown in figure 2.9(c). There is a slight improvement in vertical resolution of around 10 % using the more finely spaced retrieval grid.

RR 1.5 km scan pattern, 3 km retrieval grid (C)

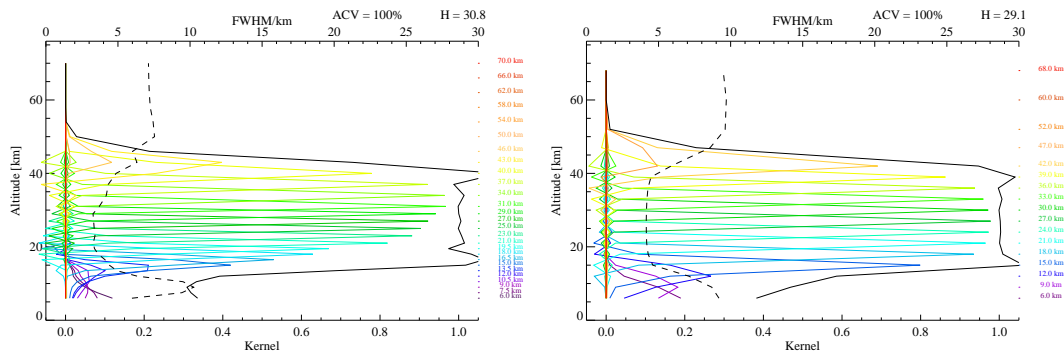
At low altitudes, by retrieving on a 3 km grid there are effectively 2 spectra available at each retrieval level, and in the UTLS region, this configuration results in the best precision. Averaging kernels are shown in figure 2.9(d).

2.3 Systematic errors

In reality, effects not included in the pure gas analysis such as interference from contaminant species, instrumental and modelling errors, could be



(a) FR 3km nominal scan pattern and 3 km retrieval grid (A, table 2.1). (b) RR 3 km nominal scan pattern and 3 km retrieval grid (D, table 2.1).



(c) RR 1.5 km nominal scan pattern and 1.5 km retrieval grid (B, table 2.1). (d) RR 1.5 km nominal scan pattern and 3 km retrieval grid (C, table 2.1).

Figure 2.9: Simulated N_2O_5 averaging kernels for the configurations listed in table 2.1. Vertical resolution (FWHM) shown as dashed line. Integrated kernels shown as solid black line. *A priori* standard deviation (denoted ACV) set to 100%. Information content also indicated (H).

important in determining the retrieval error in the full and reduced resolution modes. The error budget for CO and N_2O_5 is investigated for the FR17 and RR27 modes using operational microwindows. Microwindows are selected in order to minimise random as well as systematic errors, due to interference from contaminant species, uncertainties in pressure and temperature, instrumental calibration and unmodelled effects, such as the horizontal temperature gradient, as described in section 1.5. Figure 2.10 shows operational microwindows selected for use in the FR17 and RR27 modes under nighttime conditions as defined in the climatol-

ogy by Remedios et al. (2007). Retrieval points are placed at the tangent altitudes.

The error budget for CO is shown in figure 2.11. As before, there is a marked increase in random error (RND) due to oversampling in the vertical domain. However, up to 21 km, systematic errors due to uncertainties in the horizontal temperature gradient (GRA) are larger in the RR27 mode than in the FR17 mode. Uncertainties in the continuum (CTM) also contribute more to systematic error in the RR27 mode. Random errors dominate above 21 km reaching 100 % of the profile value, indicating that the retrieved profile at these altitudes is derived entirely from the prior estimate. Selection of additional high altitude RR27 microwindows may be necessary to overcome the low signal and high random error in the mid-stratosphere and above.

Random and systematic errors calculated for N_2O_5 are shown in figure 2.12. As before, the random error is larger in the RR27 mode due to oversampling in the vertical domain from the lowest tangent altitude up to 31 km. Uncertainties in the spectral database (SPECDB) make the most significant contribution to systematic error at both full and reduced resolution, as the infra-red properties of N_2O_5 are still relatively poorly characterised. Uncertainties in temperature (TEM) and pressure (PRE) make a slightly smaller contribution to the error budget in the RR27 mode than in the FR17 mode below 21 km.

Continuing optimisation of operational microwindows for the new measurement modes, particularly the minimisation of systematic errors, is an important area for future work. The propagation of systematic errors may lead to significant retrieval biases, which are a more serious concern than increases in random error, whose impact can be reduced by averaging of data. Biases in the ESA level 2 retrieval using operational

full and reduced resolution microwindows have already been noted for ozone by Ceccherini et al. (2008), and may well exist for other species, especially if there are systematic biases present in the pressure and temperature retrievals. The importance of quantifying the horizontal temperature gradient in the reduced resolution modes has been noted by von Clarmann et al. (2009).

2.4 Conclusions

The effects of changes in spectral resolution and vertical sampling were investigated for the retrieval of CO and N₂O₅, which were selected due to their differing spectral shapes. A brief study was performed investigating the change in signal of a modelled CO line in the stratosphere where the change in spectral resolution was expected to have a significant effect. However, the degradation was somewhat less pronounced than anticipated, with a factor 0.5 reduction in signal at 30 km. Retrieval quality was then considered in terms of random errors, averaging kernels, information content and vertical resolution, using pure gas spectra modelled using the RFM for the following configurations: FR17, RR17, RR27 measurement grid with retrieval points at the tangent altitudes, and RR27 measurement grid with retrieval points at the FR17 tangent altitudes, listed in table 2.1.

In general, retrieval quality for nighttime CO was highest in the UTLS, where random errors were below 40 % and the integrated averaging kernels approached unity. Above 31 km, the best retrieval random error was obtained in the FR17 mode. For retrievals performed on the 3 km grid, vertical resolution of 5 km was obtained in the UTLS, decreasing to 10 km in the upper-stratosphere. It was found that by retrieving

on a 1.5 km grid, vertical resolution was only slightly improved ($< 10\%$ at 20 km) and losses in retrieval sensitivity were significant. Up to 31 km, the best retrieval random error was obtained by exploiting the increased number of measurements in the UTLS, and retrieving on a 3 km grid from the RR27 data.

The impact of the RR modes on the retrieval of N_2O_5 was less pronounced. Retrieval quality for this molecule was highest in the mid-stratosphere where concentrations are at a maximum. Vertical resolution of 5 km was obtained. As with CO, the increase in vertical resolution obtained in the UTLS by placing the retrieval points at the tangent altitudes was small whereas losses in retrieval sensitivity were significant. Up to 31 km, retrieving from the RR27 data on a 3 km grid also resulted in the best retrieval precision.

The propagation of random and systematic errors through the retrieval was investigated using operation microwindows selected for use in the RR27 and FR17 measurement modes. For CO, systematic errors due to uncertainties in the horizontal temperature gradient were larger in the RR27 mode. Uncertainties in the background continuum also contributed more in the RR27 mode.

For N_2O_5 , differences in systematic errors between full and reduced resolution were less significant, and uncertainty in the spectral database was the most significant factor at both full and reduced spectral resolution.

Minimisation of systematic errors in the reduced resolution modes through the selection of an optimal set of microwindows that are consistent between measurement modes is an important area for future work. In addition, further high altitude RR27 microwindows should be selected for CO to overcome the problem of weak signal and high retrieval random

errors.

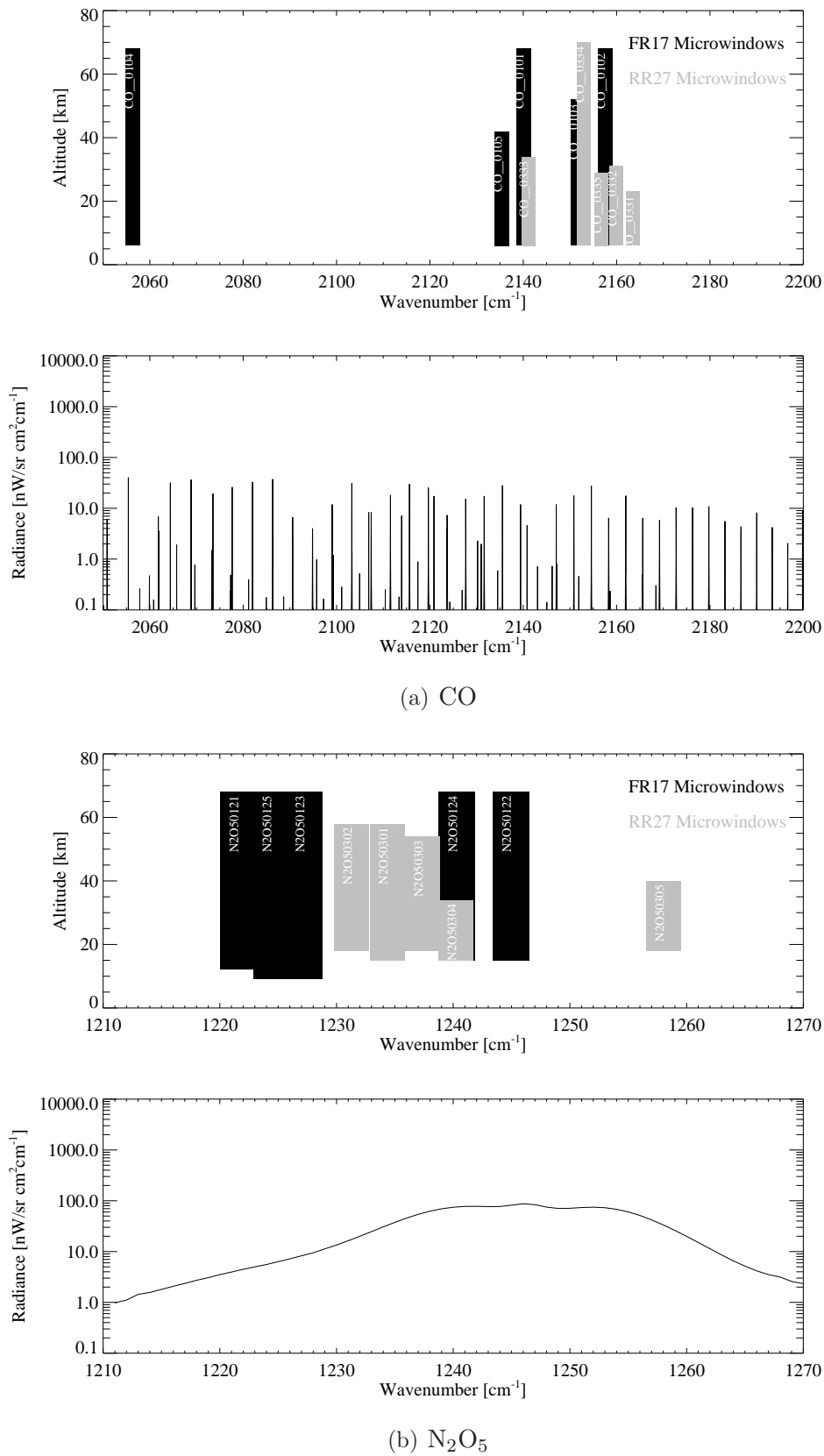


Figure 2.10: Spectral features and microwindows selected for CO and N_2O_5 in the FR17 and RR27 modes.

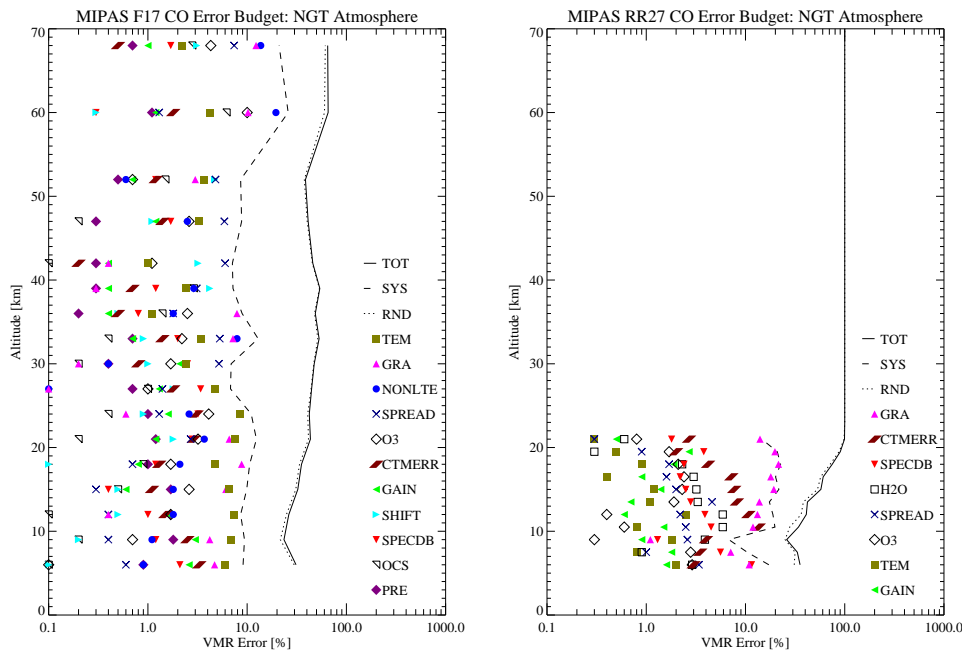


Figure 2.11: Random and systematic errors for CO in the FR17 and RR27 mode using operational microwindows. Retrieval points at tangent altitudes.

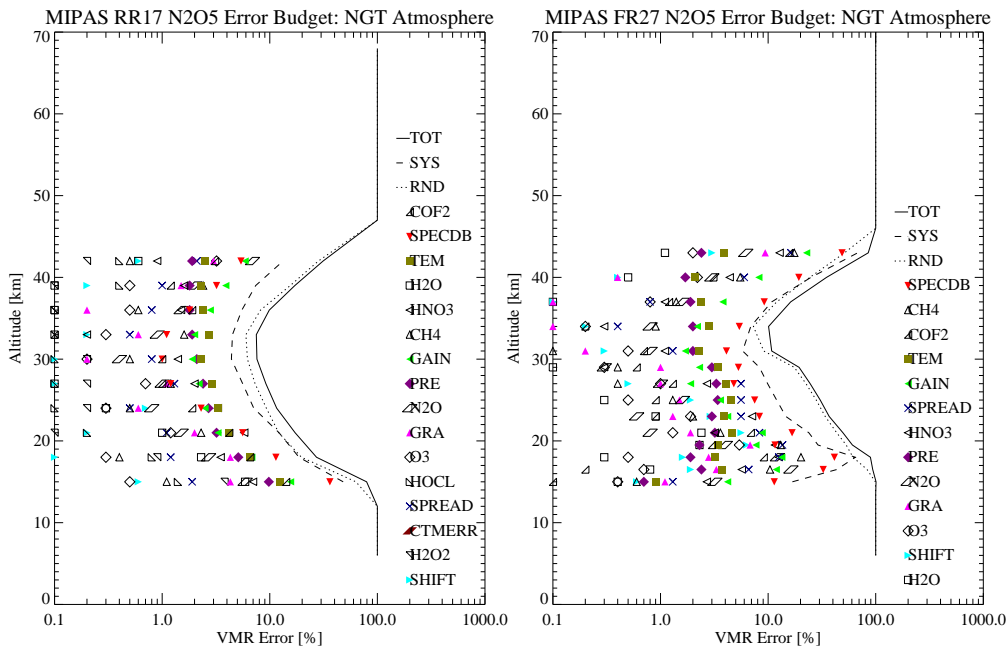


Figure 2.12: Random and systematic errors for N_2O_5 in FR17 and RR27 mode using operational microwindows. Retrieval points at tangent altitudes. Abbreviations are listed in 1.1.

Chapter 3

Carbon monoxide

3.1 Role in the atmosphere

In the troposphere, CO is produced primarily by the oxidation of atmospheric methane and other hydrocarbons as well as from various terrestrial sources including the incomplete combustion of fossil fuels and biomass (Brasseur et al., 1999b). Carbon monoxide is a useful tracer molecule for biomass burning plumes (e.g. Edwards et al., 2006) and transport of pollution (e.g. Heald et al., 2003). Anthropogenic sources were small until the 20th century, but it is now estimated that Northern Hemisphere (NH) concentrations may have doubled in the latter half of last century, mostly due to man's industrial activities, with CO produced from human activities now accounting for the majority of the global budget (Brasseur et al., 1999b). Carbon monoxide has a significant effect, at least locally, on the oxidising capacity of the troposphere where it is the main sink of the hydroxyl (OH) radical, in many areas controlling OH concentrations (Logan et al., 1981; Brasseur et al., 1999b). The role of tropospheric OH as the atmospheric cleaning agent led the theoretical atmospheric chemist S. Madronivich to postulate a "run-away"

pollution effect whereby removal of OH diminishes the troposphere's capacity for the oxidation and removal of other atmospheric pollutants. However, rather interestingly, despite strong increases in CO (and the other principal sink of the hydroxyl radical, CH₄) in the industrial era, the tropospheric hydroxyl system has been shown to be remarkably stable, with hardly any change in global mean OH concentration (Lelieveld et al., 2002).

At higher altitudes, the flux of CO from the troposphere and production of CO via oxidation of CH₄ are small compared to losses via OH destruction, which leads to a stratospheric minimum. In the upper atmosphere CO produced by photodissociation of CO₂ leads to increasing concentrations with height. There are strong horizontal and vertical gradients of CO in the middle-atmosphere, making it a useful tracer molecule for stratospheric motions or as a reference tracer for other chemical species, for example in processes of tropospheric-stratospheric exchange (e.g. Newell, 1977), or in relation to the polar vortex (e.g. Allen et al., 1999), especially at high altitudes where other diagnostics may not be readily available.¹

Limb observations of infra-red CO emissions are complicated by non-LTE (non local thermodynamic equilibrium) whereby the emitted radiance is not characterised by the local kinetic temperature.

3.2 Previous measurements

The first space-based measurements of CO were performed from ATMOS/Spacelab3; an FTS spectrometer launched aboard the Space Shut-

¹Ertel's potential vorticity is typically used as a tracer of vortex dynamics, but large uncertainties in model wind vectors at high altitudes place an upper limit on this diagnostic, typically around $\theta = 1000K$, or ~ 5 mb.

Instrument	Platform	Type	Operational	Reference
ATMOS	Spacelab 3	Limb-viewing FTS IR ab- sorption	May 1985	Irion et al. (2002)
ISAMS	UARS	IR Gas correla- tion radiometer	1991–92	López-Valverde et al. (1996)
IMG	ADEOS	IR FTS nadir	1996–97	Barret et al. (2001)
MOPITT	EOS Terra	IR gas correla- tion radiometer nadir	1999 –	Emmons et al. (2002); Wang et al. (1999)
SMR	Odin AOS	Limb-viewing microwave	2001–2006	Dupuy et al. (2004)
SCIAMACHY	ENVISAT	Limb viewing near-IR, scat- tered radiation	2002 –	Buchwitz et al. (2004)
MIPAS	ENVISAT	Limb-viewing IR FTS spec- trometer	2002–	Belotti et al. (2006)
ACE-FTS	SCISAT-1	IR FTS solar occultation	2003 –	Clerbaux et al. (2005)
TES	EOS Aura	Nadir viewing IR spectrome- ter	2004 –	Luo et al. (2007)
MLS	EOS Aura	Limb-viewing microwave	2004 –	Filipiak et al. (2005); Pumphrey et al. (2007)

Table 3.1: Some previous space-based measurements of atmospheric CO concentrations. Table of acronyms included in preface.

tle in 1985. Carbon monoxide concentrations were determined using solar occultation measurements of the $4.6\mu\text{m}$ ro-vibrational band (Irion et al., 2002). This type of measurement is largely unaffected by non-LTE since, unlike emission measurements, which depend on the populations of the excited states, absorption depends on the population of the ground state which is usually only weakly affected. Solar occultation measurements of the bands centred on $4.6\mu\text{m}$ and $2.3\mu\text{m}$ have since been used to determine CO from ACE-FTS/SCISAT-1 (Clerbaux et al., 2005; Barret et al., 2001). In addition, scattered solar radiation in the $2.3\mu\text{m}$ region

has been used to determine CO from SCIAMACHY-ENVISAT (Buchwitz et al., 2004). Microwave measurements, which are insensitive to cloud and aerosol, are now also being performed from SMR on Odin (Dupuy et al., 2004), and MLS on Aura (Filipiak et al., 2005). The rotational transitions involved in microwave emissions are easily thermalised by collisions with ambient molecules even at high altitudes, and so these measurements are unaffected by non-LTE. Currently, however, emission measurements of the $4.7\ \mu\text{m}$ band, which can provide global coverage without the complications of measuring scattered radiation, are commonly only performed in the nadir, for example retrievals from MOPITT-Terra (Emmons et al., 2004), TES-Aura (Luo et al., 2007) or IMG-ADEOS (Clerbaux et al., May 1999; Barret et al., 2001), where the short path length viewed through the upper atmosphere means that the non-LTE contribution can be neglected. Such observations generally focus on the troposphere and are unable to provide the vertical resolution in the UTLS and high altitude measurements afforded by limb sounders. As an example of the non-LTE effects encountered in limb-sounding observations, figure 3.1 shows the day and nighttime radiance for a mid-latitude sweep at 12 km. Even at low altitudes, the observed daytime radiance is enhanced with respect to nighttime radiance. The long path length viewed through the upper layers means that non-LTE emissions from higher altitudes affect limb radiances even at tangent heights much lower than where the breakdown of non-LTE occurs. Carbon monoxide has been determined from limb emission around $4.7\ \mu\text{m}$ in the past, however, using the infra-red radiometer ISAMS-UARS (López-Valverde et al., 1996) and, more recently, from MIPAS-ENVISAT, either by neglecting non-LTE effects (Belotti et al., 2006) or through sophisticated modelling of the non-LTE populations (Funke et al., 2008). The Generic non-LTE popu-

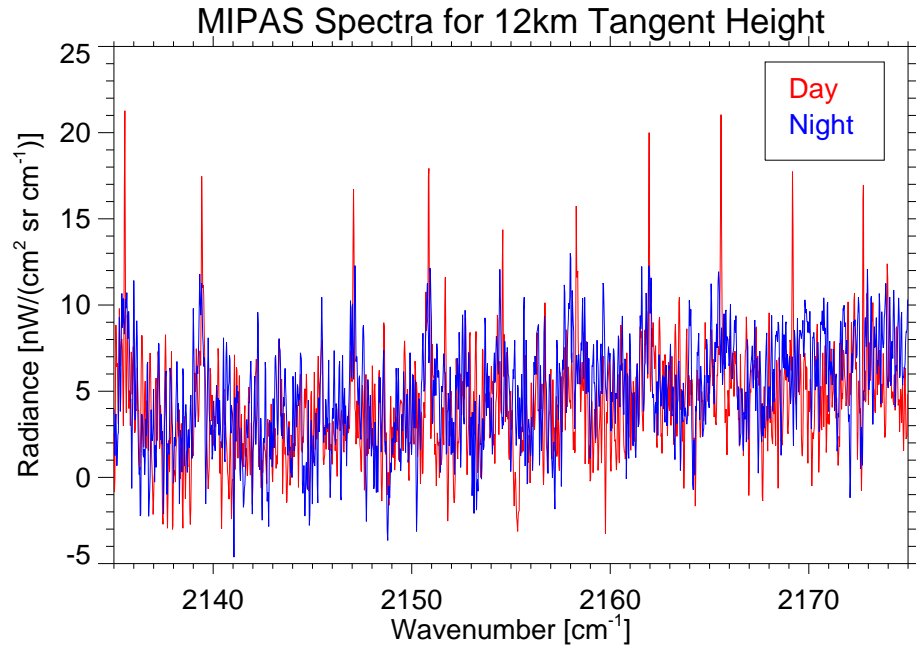


Figure 3.1: Real mid-latitude day and nighttime MIPAS spectra (L1B version 4.61 after apodisation) around 2140–2170 cm^{-1} at the 12 km tangent altitude.

lations model for MIPAS-ENVISAT data analysis (GRANADA) (Funke et al., 2002) was originally developed for retrievals from ISAMS and has since been adapted for use in retrievals of CO from MIPAS. The physics behind such models is complicated, however, and the calculations time-consuming, essentially ruling out the operational processing of CO by ESA using these methods. We investigate a simpler and faster approach, retrieving CO jointly with a parameter that characterises the non-LTE effects known as “vibrational temperature”; a method, which if implemented successfully, could allow for the operational processing of CO from MIPAS.

3.3 Non local thermodynamic equilibrium

Non-LTE is described following López-Puertas and Taylor (2001). Interactions between molecules within an isolated parcel of gas, via radiative

and collisional exchange of energy, eventually leads to thermodynamic equilibrium between the various modes, both translational and internal. Under these conditions, the distribution of molecular velocities is given by Maxwell's distribution at the kinetic temperature T_k , and the internal energy levels are populated according to Boltzmann's law at that temperature. The source function is then given by the familiar Planck function and depends only on T_k ;

$$J(\nu, T_k) = B(\nu, T_k) = 2hc^2\nu^3 \left[\exp\left(\frac{hc\nu}{kT_k}\right) - 1 \right]^{-1} \quad (3.1)$$

In the atmosphere, parcels of gas are not isolated and, in principle, no such equilibrium can be defined. It is useful, however, to look for situations where it is a close approximation to reality. The concept of a *local* thermodynamic equilibrium (LTE) was first suggested by Schwarzschild in 1906, who recognised its utility in his study of stellar atmospheres (López-Puertas and Taylor, 2001). In simple terms, conditions of LTE apply when the internal energy states are closely coupled to the kinetic distribution. It happens that a *local* kinetic temperature can be defined anywhere in the atmosphere, since the translational distribution responds much more quickly to any external change than the internal energy states and, additionally, the transfer of energy to and from the internal to the translational modes is not sufficient to significantly alter the translational distribution. At low altitudes, where collision rates are high, coupling of the internal modes to the kinetic distribution is strong, and so conditions of LTE tend to prevail in the troposphere and lower-stratosphere.

At low pressures, however, the vibrational populations may be principally controlled by other factors such as upwelling radiation, a par-

ticular resonance in the solar excitation or collisions with other excited molecules, for example. Few collisions with the surrounding gas mean that these states are maintained out of equilibrium with the kinetic distribution and the molecules are said to be in non local thermodynamic equilibrium (non-LTE).

The populations of the upper and lower energy levels may be described by the Statistical Equilibrium Equation (STE) which accounts for the various excitation and de-excitation processes. For a two level system, it is given by;

$$\frac{n_1}{n_0} = \frac{B_{01}\bar{L}_{\Delta v} + K'[M] + p_{nt}}{A_{10} + K[M] + l_{nt}} \quad (3.2)$$

where B_{01} and A_{10} are the Einstein coefficients for spontaneous absorption and emission respectively, describing the rate at which particles exchange energy with the radiation field, $K'[M]$ and $K[M]$ are the rate of increase per unit volume of molecules in state 1 and 0 respectively due to thermal collisional processes and p_{nt} and l_{nt} represent other so-called non-thermal processes (López-Puertas and Funke, 2007), for example collisions with molecules already in non-LTE. The vibrational temperature structure can be understood qualitatively by considering the various excitation and de-excitation processes. For an optically thin band, where only collisions and radiative de-excitation are important (radiative absorption is negligible), departures from LTE begin when the rate of collisional de-excitation $K[M]$, which is proportional to pressure, is of the same order as the rate of spontaneous² radiative de-excitation A_{10} . The energy level difference is important in this respect. Carbon monoxide (and NO), for example, has large gaps between its ro-vibrational levels, and so higher collisional rates are needed to maintain LTE for this molecule, with de-

²Stimulated emission is not normally considered.

partures at relatively low altitudes, around 40km. In the upper stratosphere, spontaneous emission dominates and the populations of CO(1) are lower than LTE. However, radiative excitation $B_{01}\bar{L}_{\Delta\nu}$ in the mesosphere by the solar flux and upwelling flux from the lower layers becomes more important due to increasing CO concentrations, leading to higher than LTE populations. Spontaneous emission to space dominates in the thermosphere.

A more general source function is needed which allows for the non-Boltzmann distribution of the energy level populations but reduces to the Planck function under LTE. It is given by;

$$J(\nu, T_K) = B_\nu r_2 \frac{\bar{k}_\nu}{k_\nu}; \quad \frac{k_\nu}{\bar{k}_\nu} = r_1 \left[\frac{1 - \Gamma r_2 / r_1}{1 - \Gamma} \right] \quad (3.3)$$

where r_1 and r_2 are the non-LTE to LTE population ratios of the levels denoted 1 and 2, \bar{k}_ν is the LTE absorption coefficient, k_ν is the non-LTE adjusted absorption coefficient and Γ is the Boltzmann exponential factor given by $\Gamma = \frac{g_1}{g_2} \exp\left(\frac{-h\nu_0}{kT_k}\right)$. When the non-LTE state distributions are known, it is possible to compute the radiative transfer in the usual manner, including the non-LTE adjusted source term, according to;

$$\begin{aligned} L(x_{obs}) &= \int_{\Delta\nu} \int_{x_s}^{x_{obs}} J_\nu(x) \frac{d\tau_\nu(x)}{dx} dx F(\nu) d\nu \\ ; \tau_\nu(x, x_{obs}) &= \exp\left(-\int_x^{x_{obs}} k_\nu(x') n_a(x') dx'\right) \end{aligned} \quad (3.4)$$

Computation of the radiance given some pre-computed estimate of the non-LTE state distributions has been implemented in the RFM (Dudhia, 2008b; Edwards et al., 1993).

The calculation of the non-LTE state distributions from first princi-

ples is much more involved, and is the time-consuming task of sophisticated non-LTE populations models such as GRANADA which considers the incoming solar flux, radiative transfer between layers, collisional excitations, chemical productions (important for NO) as well as factors such as cloudiness and surface albedo (Funke et al., 2002). The populations are computed using the inversion of the multi-level³ steady-state equations using either the Lambda iteration⁴ or Curtis matrix⁵ formalisms. An in depth discussion of these methods is beyond the scope of this thesis but may be found in López-Puertas and Taylor (2001).

Modelling studies have been performed using GRANADA that investigate the importance of various factors in determining the non-LTE effects for CO (see López-Puertas et al., 1993). In general, non-LTE effects are stronger during the day than at night. Solar pumping of the CO(1) vibrational state in the region around $4.7 \mu m$ results in strong daytime non-LTE emissions, with the solar flux and the mesospheric CO abundance being the main factors determining the non-LTE effects. Excitation rates are significantly greater at high solar zenith angles and high mesospheric CO abundance increases this excitation further. At low solar zenith angles, however, high CO abundance means that the solar flux is absorbed in the upper regions, and gives rise to smaller excitation rates in the mesosphere. At night, non-LTE effects are less important but, for low CO abundances, tropospheric VMR and kinetic temperature play an important role in mesospheric excitation through radiative cou-

³“multi-level” as in the energy levels affected by radiative and collisional processes involving other levels.

⁴Lambda iteration is the method of finding an iterative solution to the source function and radiative transfer equation to compute radiance at a given altitude in a particular frequency interval (inversion in frequency domain).

⁵The Curtis matrix describes the transmittances between atmospheric layers. This method finds an iterative solution to the source function and radiative transfer to compute radiance at a given frequency over a particular altitude range (inversion in altitude domain).

pling in the population of CO(1). For higher CO abundances, the major absorption in the mesosphere at night takes place from photons emitted from upper altitudes in the stratosphere, which being warmer produce a larger excitation. Vibration-vibration energy transfer (V-V), one of the so-called non-thermal process, whereby vibrational energy is exchanged between molecules, with at least one of them being in non-LTE, is also important during the day but more so, relatively speaking, at night. The most important V-V exchange partner is N₂ (López-Puertas et al., 1993; Allen and Simpson, 1980)



3.3.1 Vibrational temperature

Vibrational temperature, T_v , is a parameterisation of the non-LTE populations. It is the temperature inserted into the Boltzmann exponential factor that produces the observed non-LTE population for a given vibrational level. Following Edwards et al. (1993), the ratio of non-LTE to LTE populations (r_m) for a level m may be expressed

$$r_m = \frac{n_m}{\bar{n}_m} = \frac{n_0}{\bar{n}_0} \exp\left(\frac{E_m}{k} \left(\frac{1}{T_{v_m}} - \frac{1}{T_k}\right)\right) \quad (3.6)$$

where the bar notation denotes LTE, n_0 is the population of the ground state, T_{v_m} is the vibrational temperature of the level m , T_k is the kinetic temperature and E_m is the difference in energy between the level m and the ground state.

3.3.2 Treatment of non-LTE in the RFM

The RFM accepts pre-calculated non-LTE state distributions in the form of vibrational temperatures to calculate the non-LTE adjustment to the source term according to equation 3.3. This functionality allows T_v to be treated as an additional retrieved parameter. Since the spacing between rotational levels is small and the populations are easily thermalised, rotational levels for most species are assumed to be in LTE below 120 km (Edwards et al., 1993).

3.3.3 Existing non-LTE retrieval schemes

Non-LTE retrieval schemes include a non-LTE populations model in the inversion process. However, due to radiative and collisional coupling between energy levels, the radiative transfer calculations entail a high computational cost. In addition, since the non-LTE effects often depend on the retrieved parameters, for example kinetic temperature or VMR, calculations of the non-LTE state distributions must often be performed within each iteration of the retrieval (López-Puertas and Funke, 2007). Including a non-LTE model within the inversion process therefore leads to long processing times.

IMK/IAA retrieval

A non-LTE retrieval scheme for use with MIPAS-ENVISAT data has been developed at IMK/IAA (Institut für Meteorologie und Klimaforschung/ Instituto de Astrofísica de Andalucía). The forward model used is the Karlsruhe Optimised and Precise Radiative transfer Algorithm (KOPRA), which is a line-by-line radiative transfer code for the calculation of atmospheric transmission and radiance along with the partial deriva-

tives of the spectra with respect to the atmospheric state parameters (see Stiller et al., 2002; Stiller and von Clarmann, 2008). KOPRA is used in conjunction with the GRANADA model which calculates the non-LTE state distributions and their jacobians with respect to the retrieved parameters. To account for the strong mesospheric contributions due to non-LTE effects, the retrieval is performed on an altitude grid of 1 km step widths up to 50 km, 2–2.5 km steps between 50 and 80 km and 5–10 km steps to 120 km. The retrieval is a global fit non-linear least squares algorithm with Levenberg-Marquardt damping (López-Puertas and Funke, 2007). A Tikhonov-type user defined regularisation is applied to deal with ill-conditioning due to oversampling of the retrieval grid compared to the tangent height spacing (Funke et al., 2008).

3.4 Systematic errors due to ignoring non-LTE

The simplest way to avoid complicated, time-consuming calculations of the non-LTE populations within the inversion process is to ignore the non-LTE effects altogether. To investigate the impact of neglecting the non-LTE effects, four cases are considered which represent the range of atmospheric conditions encountered globally:

1. Mid-latitude daytime (sunlit).
2. Mid-latitude nighttime (dark).
3. Polar summer (sunlit).
4. Polar winter (dark).

These conditions correspond to a set of standard atmospheres which make up the IG2 climatology. Non-LTE effects were included using representative vibrational temperature profiles provided by IAA. The mid-latitude daytime and polar summer cases are sunlit and include the solar pumping of the v_1-0 transition, whereas the mid-latitude nighttime and polar winter cases are in darkness. Retrieval random and systematic errors were calculated for the cases listed above for the FR17 mode using the RFM to simulate pure CO spectra between $2135\text{--}2175\text{ cm}^{-1}$. The CO emission features were modelled across the spectral interval shown in figure 3.2. The principal contaminants in the region are also indicated in figure 3.2. Uncertainty in the contribution of contaminant species, and other errors such as uncertainties in instrumental calibration and modelling errors, were not taken into account in the calculation of systematic error.

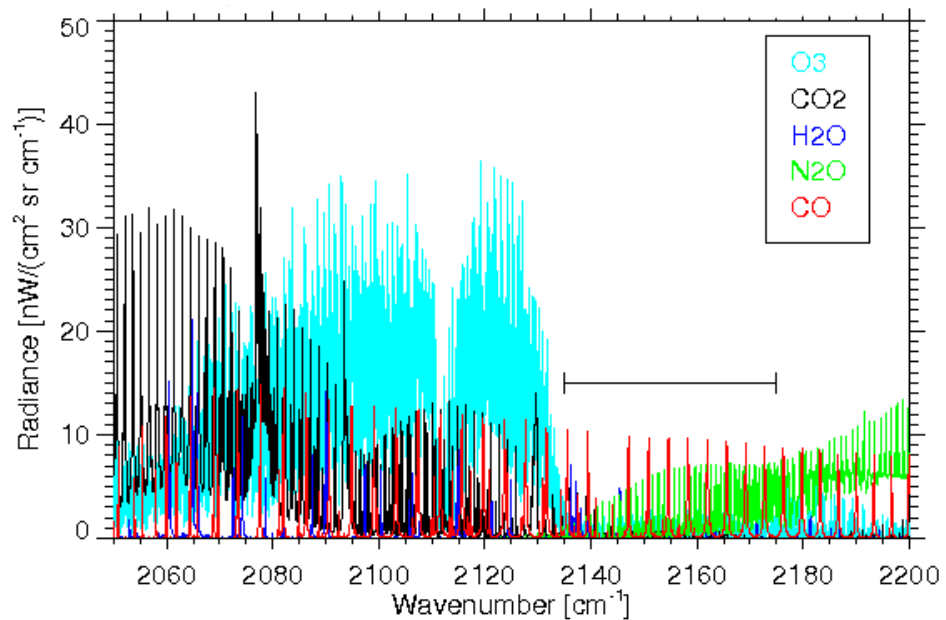


Figure 3.2: Full resolution spectra at 12 km for CO and contaminant gases, simulated under LTE conditions using the RFM between $2135\text{--}2175\text{ cm}^{-1}$. Horizontal bar shows interval used in simulations of pure CO spectra.

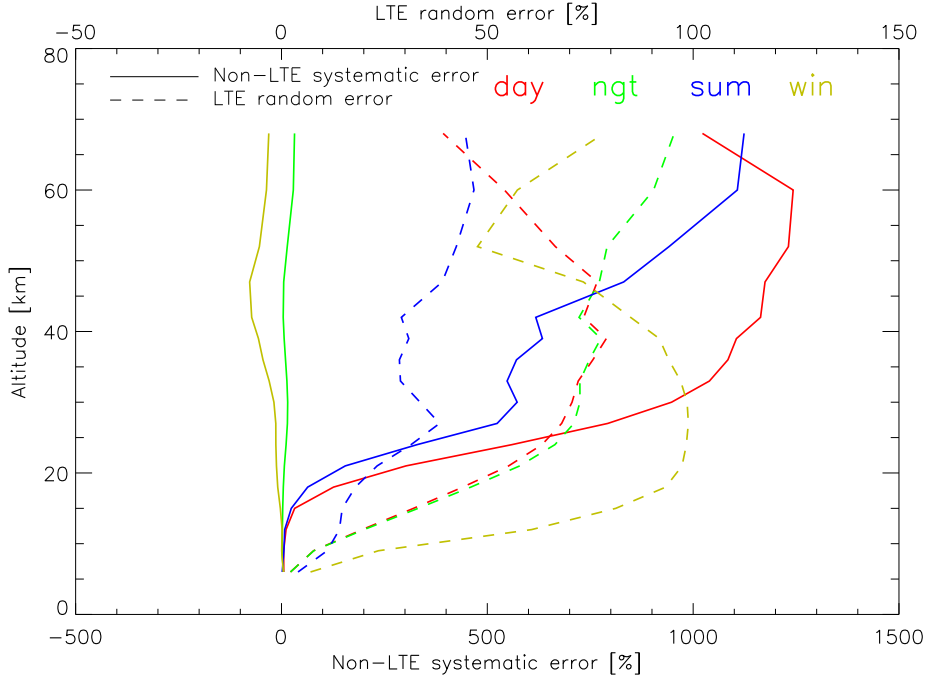


Figure 3.3: Retrieval precision and systematic error ignoring non-LTE simulated using the RFM. Precision indicated on upper axis and systematic errors on lower axis. Key: ‘day’ denotes mid-latitude daytime, ‘ngt’ denotes mid-latitude nighttime, ‘sum’ denotes polar summer, and ‘win’ denotes polar winter.

Assuming linearity, the systematic error introduced from ignoring non-LTE effects in CO may be estimated as

$$\Delta \mathbf{x} = (\mathbf{K}^T \mathbf{S}_y^{-1} \mathbf{K} + \mathbf{S}_a^{-1})^{-1} \mathbf{K}^T \mathbf{S}_y^{-1} (\mathbf{y}_{\text{non-LTE}} - \mathbf{y}_{\text{LTE}}) \quad (3.7)$$

where $\Delta \mathbf{x}$ is the error in the retrieved profile, and $\mathbf{y}_{\text{non-LTE}}$ and \mathbf{y}_{LTE} are the RFM simulated non-LTE and LTE radiances for CO calculated using appropriate vibrational temperature profiles.

In optimal estimation, retrieval precision is the combination of the propagation of instrument noise through the retrieval and the *a priori* covariance (Rodgers, 2000)

$$\mathbf{S}_x = (\mathbf{K}^T \mathbf{S}_y^{-1} \mathbf{K} + \mathbf{S}_a^{-1})^{-1} \quad (3.8)$$

where \mathbf{K} is the forward model jacobian, \mathbf{S}_y is the instrument noise covariance and \mathbf{S}_a is the *a priori* covariance. An appropriate NESR for the D-band of $4.2 \text{ nWm}^{-2}\text{sr}^{-1}\text{cm}$ is assumed. An *a priori* standard deviation of 100% is assumed for \mathbf{S}_a with no vertical correlations.

Results are shown in figure 3.3. In the mid-latitude daytime case, strong solar excitation leads to very large positive systematic errors in the upper profile levels exceeding 1000 %. In the polar summer case, the continual sunlight and long path length through the upper atmosphere, as well as radiative upwelling from the warm stratopause region, also result in strong non-LTE enhancements at high altitudes. At night, the non-LTE effect is generally less severe. However, the magnitude of the non-LTE effects in the upper-stratosphere and mesosphere at night depends upon cloud conditions and the temperature of the lower atmosphere and surface, and can be positive or negative depending on the particular conditions. In the cold, dark polar winter case, the non-LTE effect is negative. Under these conditions, upwelling flux is small due to the low temperature of the surface and troposphere, and the CO band cools effectively to space. The negative bias is of the same order of magnitude as the random error under these conditions. When the lower atmosphere is warm however, enhancements in T_v of up to 20 K are observed in the lower mesosphere, leading to a small, positive non-LTE contribution. However, figure 3.3 indicates that the systematic error due to non-LTE effects can be ignored without introducing large systematic errors at most altitudes at night under typical conditions for the surface and lower atmosphere. Under all conditions, the non-LTE effects can be safely ignored in the upper-troposphere. Under sunlit conditions at high altitudes, enhancements in signal due to non-LTE effects could lead to an improved retrieval of CO if the non-LTE conditions are modelled

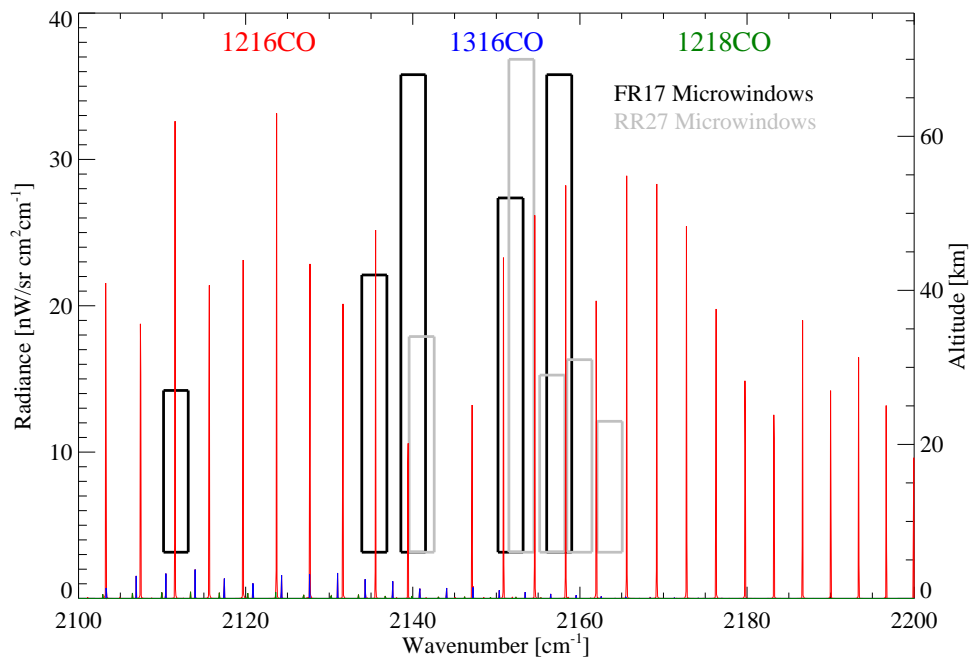


Figure 3.4: CO 4.7 μm emission at 30 km modelled using RFM, assuming non-LTE. Isotopic emission features also included. Spectral and altitude range of FR17 and RR27 CO microwindows shown.

correctly.

3.5 LTE retrieval

Retrievals of CO using RR27 data from 28th January 2005 were performed ignoring non-LTE effects. Microwindows were selected that minimise the contribution of systematic errors such as contaminant contributions, and maximise the information content on the target species. The CO emission features and the FR17 and RR27 microwindows which minimise errors due to non-LTE are shown in figure 3.4. Contaminant species, principally H_2O , N_2O , O_3 and CH_4 are retrieved beforehand for each sweep. Prior VMR for CO and contaminant species is derived from the IG2 Climatology Database v3.1 (Remedios et al., 2007). An *a priori* standard deviation of 100% of the profile value is used to construct \mathbf{S}_a

with a vertical correlation length of 50 km. Sweeps identified as cloudy are removed. Sweeps with a retrieval random error of greater than 50 % are discarded.

Zonal mean CO is calculated in 5° latitude bands, separating day ($\text{SZA} < 93^\circ$) and nighttime ($\text{SZA} \geq 93^\circ$) scans. Results are shown in figure 3.5. The fourth panel shows the relative difference between the zonally averaged nighttime CO retrievals and climatological values. In general, retrieved CO is less than the climatological value at night. The difference is less than 20 % in most regions. As expected, there is a more significant negative bias in the polar winter regions. Similarly, the 3rd panel shows the relative difference between zonally averaged daytime retrievals and the climatology. Daytime values are higher than the climatology at mid-latitudes. Day-night difference is shown in the bottom panel. Day-night difference is often considered a useful diagnostic for how well the retrieval takes account of the non-LTE excitation, since in the absence of systematic errors due to non-LTE effects, the zonally averaged day and nighttime fields should be similar. There are maximum relative differences of around 95 % in the SH mid-latitudes due to ignoring non-LTE effects.

3.5.1 Comparisons with EOS MLS

The LTE retrieval of CO using 4.61/4.62 level 1b RR27 data from 28th January 2005 is compared against CO observations from the Earth Observation System Microwave Limb Sounder (EOS MLS), which is unaffected by non-LTE. We use MIPAS retrievals for nighttime and polar winter conditions where the errors introduced by ignoring non-LTE are relatively small. Daytime scans ($\text{SZA} < 93^\circ$ at mid-point) are excluded from the analysis since errors due to neglecting non-LTE are large.

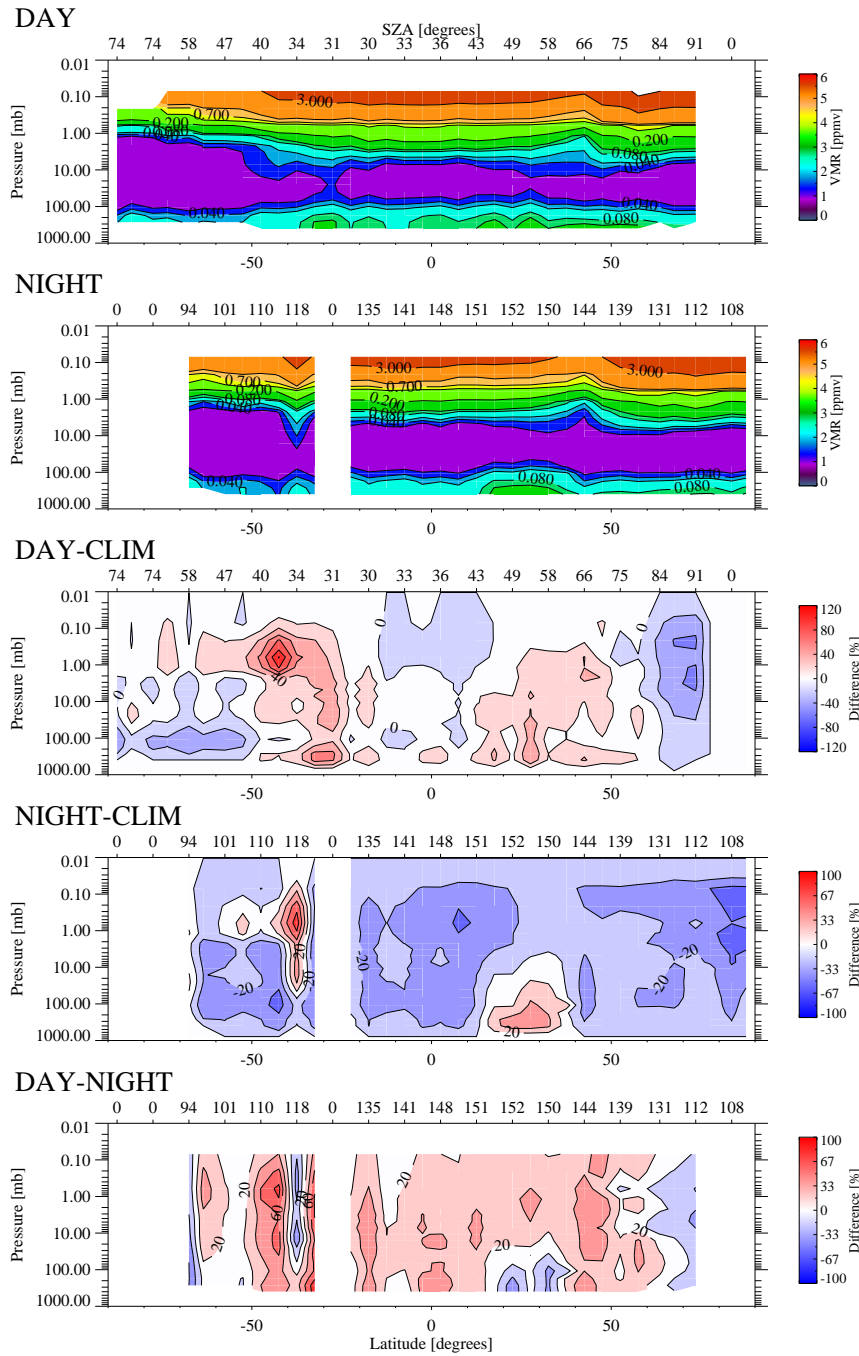


Figure 3.5: Zonal mean CO VMR on 28th January 2005 (RR27) retrieved using MORSE assuming LTE conditions. Top panel shows retrieved daytime VMR, 2nd panel shows retrieved nighttime VMR, 3rd panel shows the relative percentage difference of daytime values from climatology, 4th panel shows relative percentage difference of nighttime data from climatology, and bottom panel shows the day-night percentage difference normalised with respect to climatological values i.e. $\left(\frac{\text{CO}_{\text{day}} - \text{CO}_{\text{ngt}}}{\text{CO}_{\text{clim}}}\right) \times 100\%$.

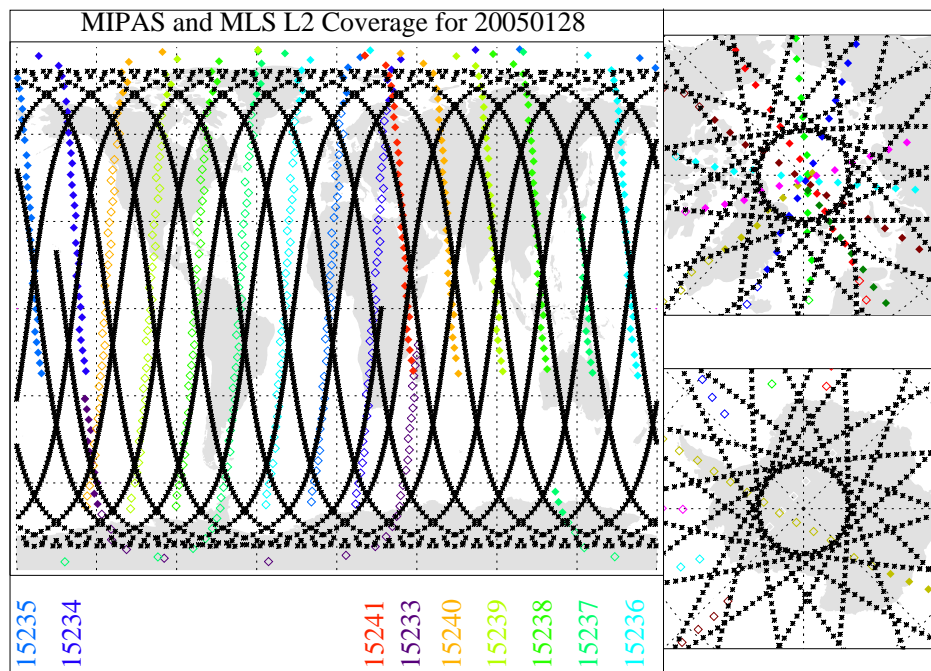


Figure 3.6: MIPAS and MLS L2 data coverage on 28th January 2005. MLS data shown as black crosses. MIPAS nighttime data ($\text{SZA} \geq 93^\circ$) shown as filled diamonds. MIPAS daytime data ($\text{SZA} < 93^\circ$) shown as open diamonds.

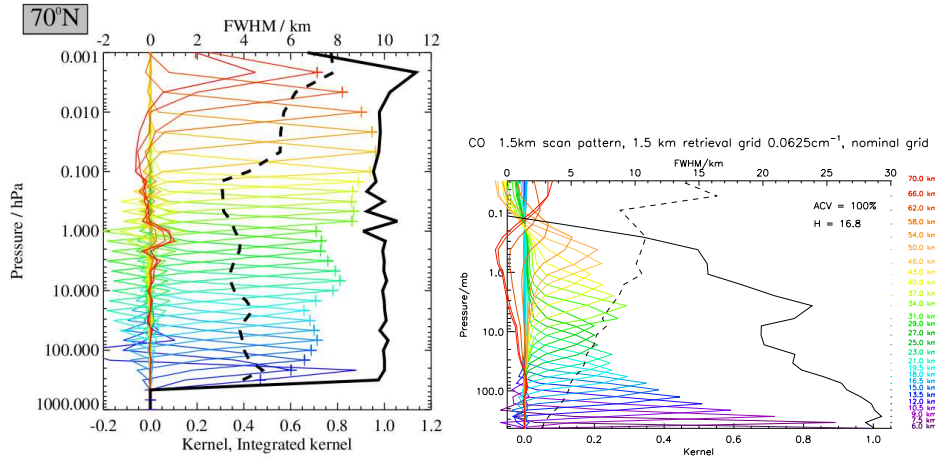
EOS MLS

EOS MLS was launched aboard NASA's Aura satellite on 15th July 2004 into a sun-synchronous polar orbit providing around 14.5 orbits per day. Figure 3.6 shows the geographical coverage of the two instruments on the 28th January 2005. The MLS measurements extend from 82S:82N, whereas MIPAS provides almost pole-to-pole coverage. The MLS profiles are more densely spaced along-track, separated by just 168 km, as opposed to 410 km for MIPAS.⁶ MLS profiles extend to higher altitudes, from 8–90 km (6–71 km for MIPAS RR27), with a total of 120 tangent points.

The MLS instrument is essentially a small radio telescope (Pumphrey et al., 2007). It uses heterodyne radiometers operating at ambient temperature with emission measurements performed in broad spectral regions

⁶Oversampling of MLS along-track is handled by including 12 scans into the measurement vector \mathbf{y} and 12 profiles into the state vector \mathbf{x} and discarding end profiles.

centered on 118 (R1), 190 (R2), 240 (R3), 640 (R4) GHz and 2.5 THz (R5) (Waters et al., 2006). Pressure and temperature are derived mainly from the O₂ line wings in the R1 band. Carbon monoxide is measured in the J 2-1 ro-vibrational band centered on 230.538GHz in the R3 band (Filipiak et al., 2005). The low energy J 2-1 transition is easily thermalised by collisions with the ambient molecules, even at high altitudes, and so measurements are unaffected by non-LTE. Measurements in the microwave region are also much less sensitive to clouds and aerosol.



(a) Simulated MLS v2.2 CO averaging kernels (Livesey et al., 2007). Thick black line denotes integrated area under kernel. Dashed black line denotes FWHM vertical resolution.

(b) MIPAS CO averaging kernels for RR27 data. Thick black line denotes integrated area under kernel. Dashed black line denotes FWHM vertical resolution on upper axis.

Figure 3.7: MLS and MIPAS RR27 simulated CO averaging kernels for Northern Hemisphere polar winter conditions.

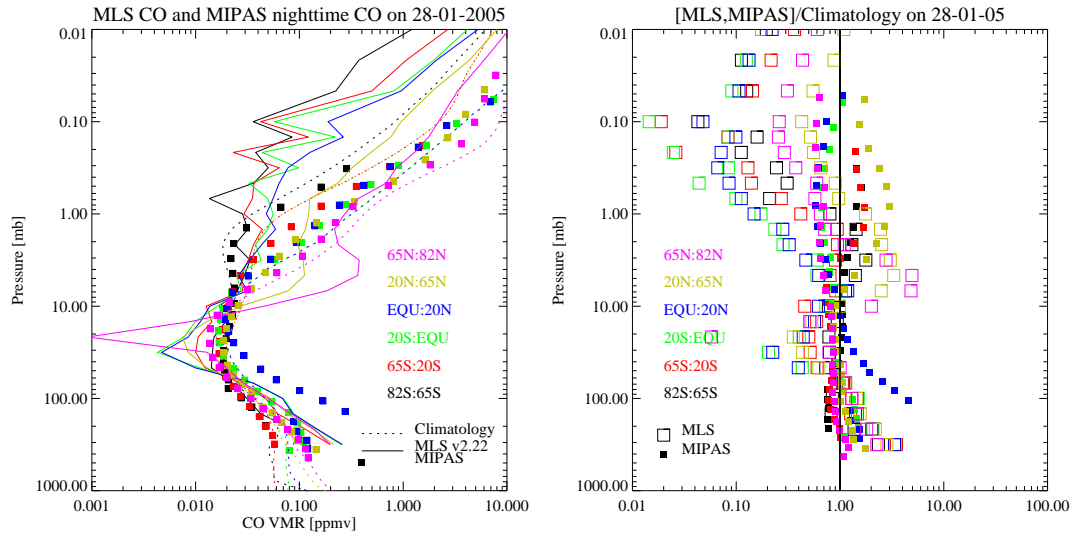
MLS CO data product

We present results from EOS MLS using the v2.22 Level 2 (L2) data products. A detailed description of the MLS retrieval, which uses a weighted non-linear least-squares approach with *a priori* constraints, may be found in Livesey et al. (2006).

The following section briefly discusses the baseline v2.2 product. The

updates included in v2.22 used in this comparison should not alter the retrieval of CO (*N. Livesey personal communication*). Figure 3.7 shows simulated averaging kernels (vertical) for the MIPAS and MLS CO retrievals. The integrated kernel is close to unity over the majority of the profile due to the use of a loose *a priori* constraint. However, random errors in the v2.2 data are generally greater than 100% VMR for much of the vertical range and considerable averaging is recommended (Livesey et al., 2007). Figure 3.7 shows that the FWHM resolution for MLS is around 4.5 km in the UTLS, decreasing to 6 km in the mesosphere. Vertical resolution for MIPAS is similar, in the UTLS, although at the top of the profile, vertical resolution is somewhat coarser.

Validation studies have shown that in v1.5 (previous baseline product) there is a positive bias of 5% in the mid-stratosphere increasing to 50–100% in the mesosphere and thermosphere compared with ACE-FTS (Froidevaux et al., 2006). After a correction in the handling of DACS (Data Analysis Center for Software) data, implemented in v2.2, this discrepancy has been mostly resolved, bringing mesospheric VMR down by 30%, into line with ACE-FTS data (Pumphrey et al., 2007). Comparisons with aircraft (AVE) and balloon (ALIAS, Mark-IV) data indicate that the MLS v1.5 CO data has a positive bias at 215hPa; values at this level are also generally 2 times larger than those from GEOS-CHEM model simulations (Livesey et al., 2005). This bias is still present in v2.2 data. There are strong oscillations in the MLS v1.5 CO profiles, attributed to problems in the regularization of the profiles (Livesey et al., 2005). These oscillations are much improved in v2.2, attributed to a combination of factors, mainly changes in the *a priori* constraints, improvements in spectroscopy and corrected handling of the DACS data (Pumphrey et al., 2007). An *a priori* that is too dissimilar from the true profile can



(a) Zonal mean of MLS (solid lines) v2.22 and MIPAS (filled squares) CO. *A priori* profiles (open squares) and MIPAS CO (filled squares) used for MIPAS retrievals derived from Reme from average climatological values. dios et al. (2007) also shown (dotted line).

Figure 3.8: Comparison of MIPAS zonal mean RR27 CO assuming LTE conditions with MLS v2.22 zonal mean CO.

be the dominant error source in the lower stratosphere and can be significant in the mesosphere. Gain compression, which originates from the spectral signature, introduced in calibrated MLS radiances by departures from linear response within the signal chains, is also a significant source of systematic error ($\pm 5\text{--}10\%$ at most altitudes, worst case $\sim 25\%$).

3.5.2 Zonal mean profiles

Zonal means were computed in 6 latitude bands: 82:65 N/S, 65:20 N/S, 20:0 N/S. The MLS data is screened as recommended in the v2.2 data quality document (see Livesey et al., 2007), removing retrievals that had failed to converge, where a poor fit to the radiances had been achieved, or where the *a priori* influence was too strong (precision greater than 50 % *a priori* VMR). Due to the large number of profiles averaged, the resulting random error in the data can be ignored in the comparison,

although caution is recommended in the 82:65 °S band where there are missing MIPAS profiles, see figure 3.6. Results are shown in figure 3.8. There is a high bias with respect to MIPAS, and the climatology, in the upper-troposphere, corresponding to the known high bias at 215hPa. Oscillations in the MLS retrievals in the mesosphere and lower stratosphere in the NH tropical band (improved in v2.22) are fairly small. In the stratosphere, the agreement between MIPAS and MLS data is quite good. However, there is a low bias of MLS with respect to MIPAS in the NH polar data, which may be due to sampling regions with differing CO concentrations in and around the polar vortex. Also, the MIPAS equatorial data drifts high in the UTLS, which may be due to cloud contamination that has not been removed successfully. The MLS measurements are consistently lower than MIPAS above 1 mb. At these altitudes, however, both data sets may be influenced significantly by prior constraints.

3.5.3 Conclusions and future work

The retrieval of CO from MIPAS ignoring non-LTE is acceptable in certain situations. In particular, the analysis of systematic errors introduced by ignoring non-LTE in section 3.4 suggests that retrievals at all altitudes should remain relatively unaffected at night. Simulations also suggest that retrievals can be performed in the UTLS without introducing significant systematic errors under all conditions examined. Polar winter data can be processed assuming LTE, although a more significant negative bias is introduced at high altitudes in this case. Using polar winter and nighttime MIPAS data, there was generally good agreement between the EOS MLS retrievals and RR27 MIPAS LTE retrievals of CO.

3.6 Joint retrieval of CO and vibrational temperature

There are clear limitations to an LTE treatment of CO. In this section, the feasibility of a joint retrieval of CO and vibrational temperature (T_v) is investigated. This method could potentially allow for CO retrievals from MIPAS to be performed quickly whilst accounting for the non-LTE effects.

Unlike more complex molecules, the non-LTE effects for CO can be characterised by a single T_v profile, as the band structure in the near infra-red is dominated by the fundamental transition CO(1-0), see figure 3.4. The joint retrieval allows for the characterisation of non-LTE effects whilst limiting the use of time-consuming calculations of the non-LTE populations within the retrieval process. Pre-computed non-LTE state distributions are adjusted within the retrieval, departing from either the kinetic temperature or else some prior estimate of vibrational temperature. If implemented successfully, this method offers significant advantages in terms of simplicity and improvements in processing times.

3.6.1 Retrieval precision

Random errors are calculated for the joint retrieval of CO, T_v and are compared against random errors for the LTE retrieval presented in section 3.4. As before, random error is simulated using the RFM for the FR17 configuration in the spectral region between 2135–2175 cm^{-1} . Joint retrieval precision is simulated for daytime and nighttime mid-latitude atmospheres. The equivalent LTE simulations are included in figure 3.9 for comparison. An *a priori* standard deviation for T_v of $z - 5$ K, where z is altitude in km, is used, reflecting the increased variability in T_v at

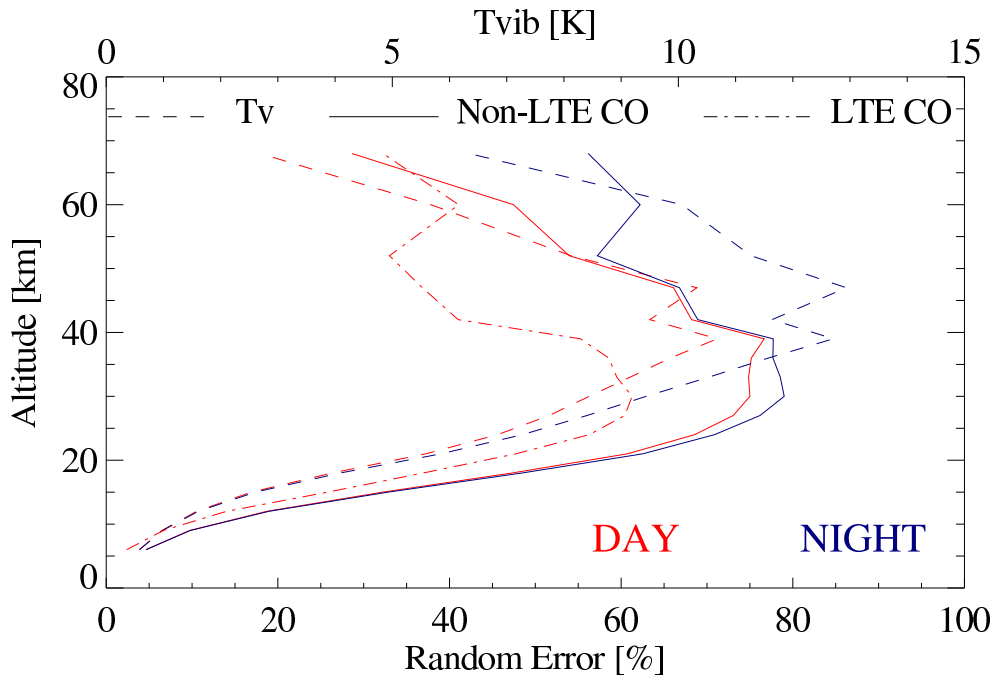


Figure 3.9: Random errors for an FR17 joint retrieval of CO and T_v , simulated under daytime and nighttime conditions using the RFM. Random errors assuming LTE conditions are also included. The *a priori* standard deviation for CO is set to 100%. *A priori* standard deviation for T_v is set to $z - 5$ K where z is altitude in km.

high altitudes. The *a priori* standard deviation of CO is set to 100% of its climatological value with no vertical correlations in \mathbf{S}_a .

As expected, random errors are worse in the joint retrieval due to the increased number of state vector elements, as well as correlations between CO and T_v . However, errors of better than 70% are obtained over most of profile; a loose indication that the majority of the information is derived from the measurements rather than the prior estimate. Retrieval precision is good in the UTLS, where random errors for CO of better than 20% are obtained. During the day, random errors for the joint retrieval above 40 km are better than in the LTE case due to the increased signal caused by non-LTE enhancements in radiance.

3.6.2 Retrievals from simulated data

Retrieval precision is poor at high altitudes. Simulations are therefore presented to determine whether a joint retrieval is feasible. When the T_v profile is known exactly, the retrieval should recover the correct CO profile. However, when there is no knowledge of the T_v structure of the atmosphere, the retrieval may struggle to fit both parameters. Simulations were performed for these extreme cases, and cases with intermediate knowledge of the T_v profile, to ascertain the necessary quality of the prior estimate of T_v .

An optimal estimation joint retrieval of CO and T_v using Levenberg-Marquardt iterations was using written for the FR17 configuration using the RFM as the forward model. Simulated truth spectra were generated using the RFM for two microwindow regions 2138.6–2141.5 cm^{-1} and 2156.0–2159.0 cm^{-1} for a CO only atmosphere, using a mid-latitude climatology for CO and a mid-latitude daytime T_v profile supplied by IAA, see also figure 3.3. Retrieval points for CO were placed at the FR17 tangent altitudes. Vibrational temperature is also retrieved at 90 and 120 km to account for variation in T_v in the mesosphere and lower-thermosphere (denoted “Upper-Atmosphere”, UA).⁷ A correlation length of 50 km was applied to CO in line with the smoothing constraint used in MORSE. A shorter correlation length of 20 km was applied to T_v to avoid over-smoothing of the vertical temperature structure.

⁷Without these extra levels, T_v is constrained to the T_k profile in the mesosphere. In this case, the retrieval tries to compensate for the mesospheric excitation that is unaccounted for by increasing the CO VMR in the top profile level to values that are much too high (over 1000 ppmv).

Vibrational temperature profile known exactly

Figures 3.10 and 3.11 show the results of simulations in which the T_v profile is known exactly. This represents a hypothetical best case, whereby random error is decreased due to non-LTE enhancements in radiance, and the systematic error due to uncertainties in the non-LTE effects is zero.

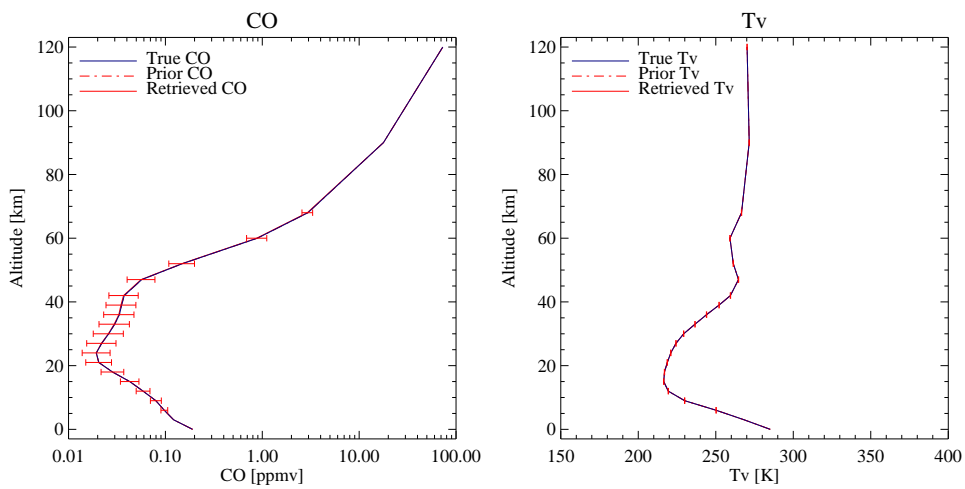


Figure 3.10: Simulated retrieved profiles when prior T_v is known exactly.

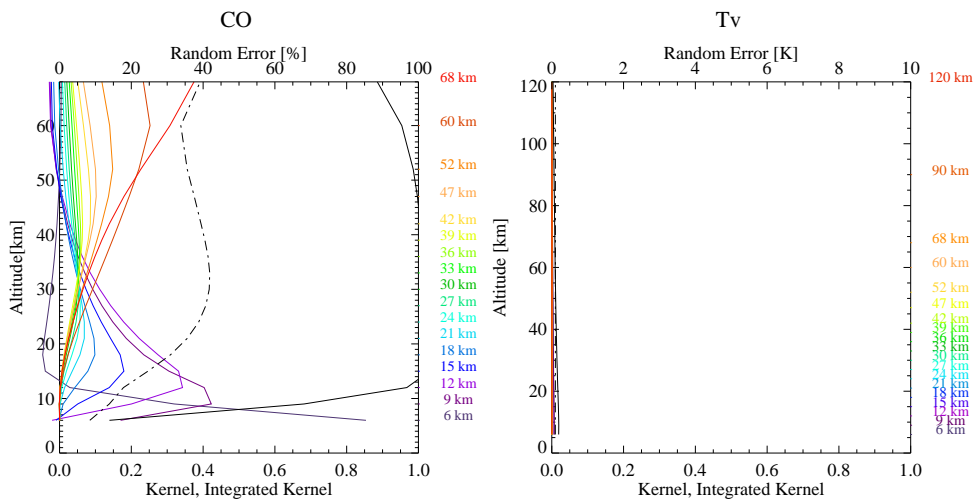


Figure 3.11: Averaging kernels when prior T_v is known exactly. Integrated kernel shown as solid line. Random error shown as dashed line.

At higher altitudes, where non-LTE enhancements improve retrieval sensitivity, the averaging kernels for CO are much better than in LTE

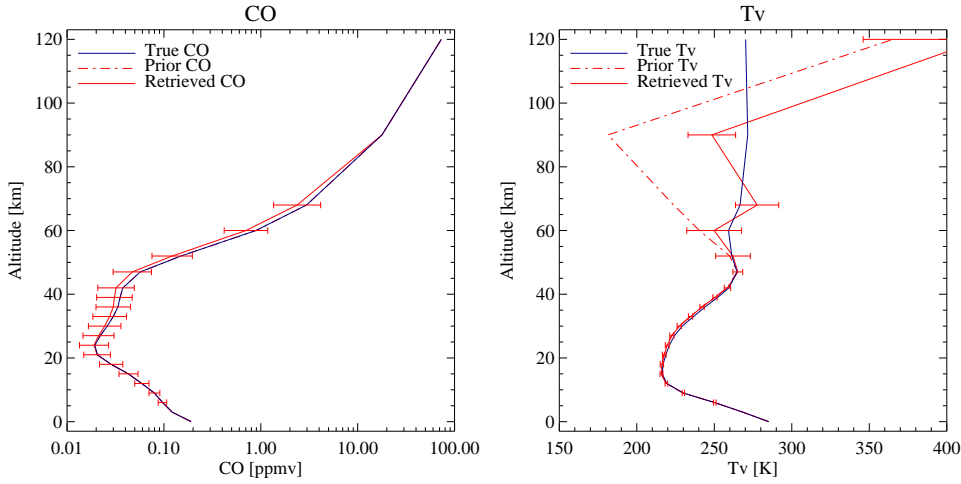


Figure 3.12: Simulated retrieved profiles when T_k is used as prior estimate of T_v .

(refer back to LTE kernels in figure 2.6(a)), the integrated kernel is unity along most of the profile, and random errors are less than 40 % above around 40 km.

Vibrational temperature profile unknown

The vibrational temperature profile will never be known exactly but will depart from some prior estimate. The simplest approach is to use T_k as the prior estimate of T_v . This assumes that we have no prior knowledge of the T_v profile and avoids the introduction of prior directional bias into the characterisation of the non-LTE effects. At high altitudes, T_k is likely to be very different from T_v , and the prior constraint on T_v must allow for a large adjustment to the profile of between 10–100 K. Therefore, $T_v - T_k$ has been used as an estimate of the *a priori* uncertainty. Below 30 km, $T_v = T_k$.

Figure 3.12 shows the retrieved profiles for CO and T_v . The extra retrieval levels at 90 and 120 km result in a better fit for T_v in the lower profile levels, and the true CO profile is recovered to within the random error.

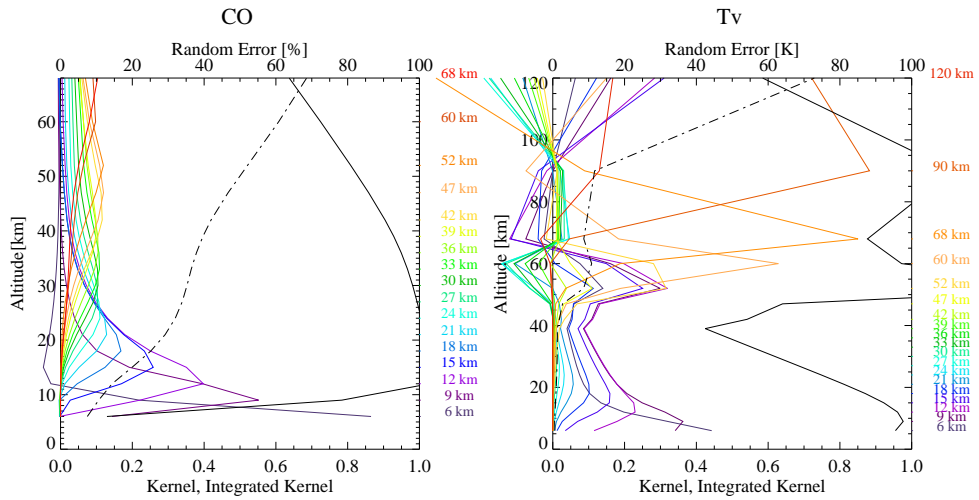


Figure 3.13: Averaging kernels when T_k is used as the prior estimate of T_v . Integrated kernel shown as black line. Random error shown as dashed line.

Averaging kernels, shown in figure 3.13, indicate that the retrieval is sensitive to CO in the UTLS. However, above this altitude retrieval sensitivity is poor and the solution is strongly influenced by the prior estimate.

Intermediate cases

Simulations were carried out as described above for additional cases, whereby the prior estimate of T_v is underestimated or overestimated by: 20 K, 7 K, 5 K and 2 K above 40 km. Prior uncertainty on CO is set to $T_v - T_k$. The results are summarised by showing the bias in retrieved CO and T_v with respect to the truth for the various cases considered. The bias in the CO retrieval for the case where the T_v profile is known exactly (0 K difference) is shown as a black line, and any deviations from zero can be attributed mainly to interpolation of profiles within the retrieval or forward model. The retrieval random errors for each case are indicated as dashed lines.

Requirements on absolute knowledge of T_v are less strict when the prior T_v is an underestimate of the true state since a given change in

T_v corresponds to a smaller difference in radiance. Results derived from underestimated T_v are shown in figure 3.14. In all cases, retrieved CO is within 20 % of the true profile at high altitudes. Below 30km, the likely deviation of T_v from T_k is negligible. The bias in retrieved CO is better than 10 % below 30 km where T_v is constrained to follow T_k to within 0.1 K. Deviations from the truth at these altitudes arise from the long correlation length (50 km) applied to the CO profile.

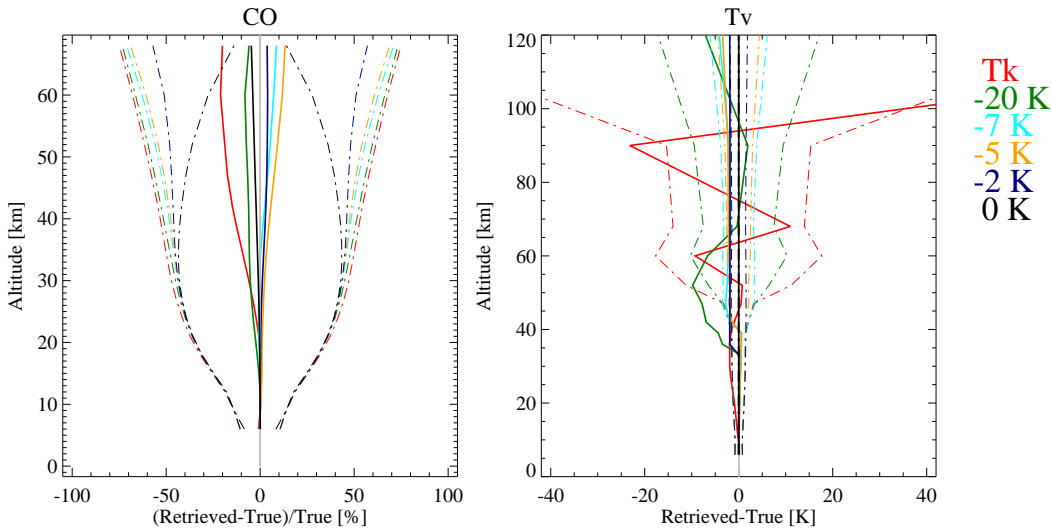


Figure 3.14: Summary of the retrieval biases when prior T_v is an underestimate of the truth. No upper atmosphere treatment of CO. Retrieval random errors shown as dashed lines.

Figure 3.15 shows results when prior T_v is an overestimate of the true state for the over and under-estimated cases, respectively. The retrieval is more difficult in these cases since for a given difference in T_v at there is a larger difference in radiance. For a T_v profile that is known to within 5–7 K, the retrieval of CO is accurate to within 30 % at high altitudes which is less than the expected variation due to random error shown in figure 3.9.

Figures 3.16 and 3.17 show the effects of including a column retrieval of CO above the top tangent altitude. As discussed in section 3.3, the

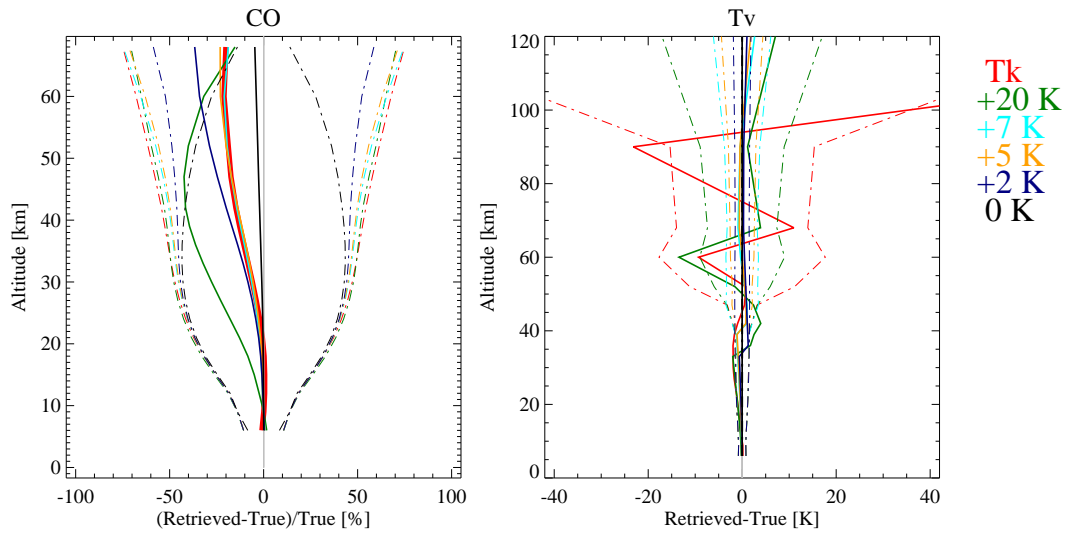


Figure 3.15: Summary of the retrieval biases when prior T_v is an overestimate of the truth. Retrieval random errors shown as dashed lines.

amount of CO in the mesosphere has a significant effect on the magnitude of the non-LTE excitation. However, the bias in CO is now worse at high altitudes, although the random error in CO is smaller. A column retrieval of CO may be unfeasible due to the limited information content of the spectra.

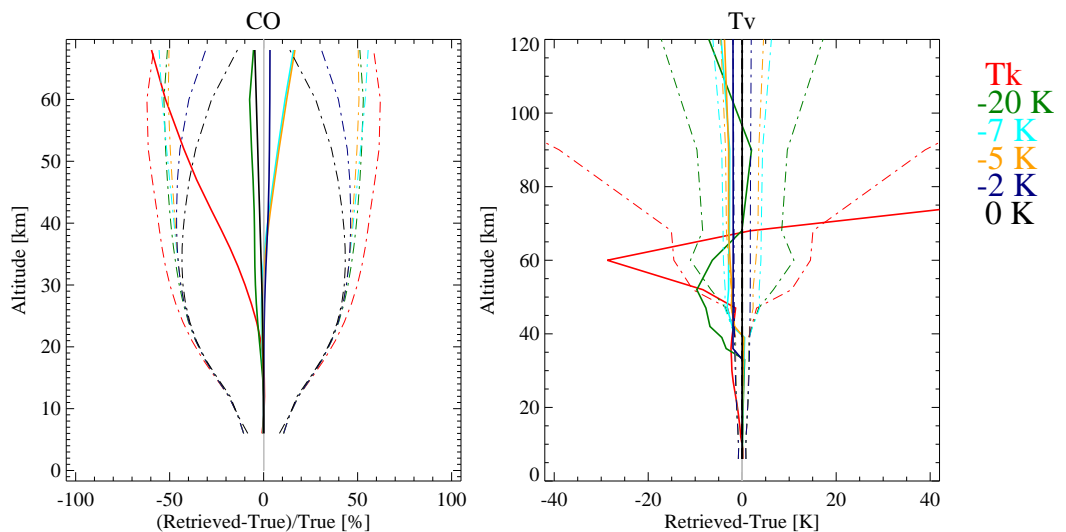


Figure 3.16: As in figure 3.14 but with upper-atmosphere column retrieval of CO.

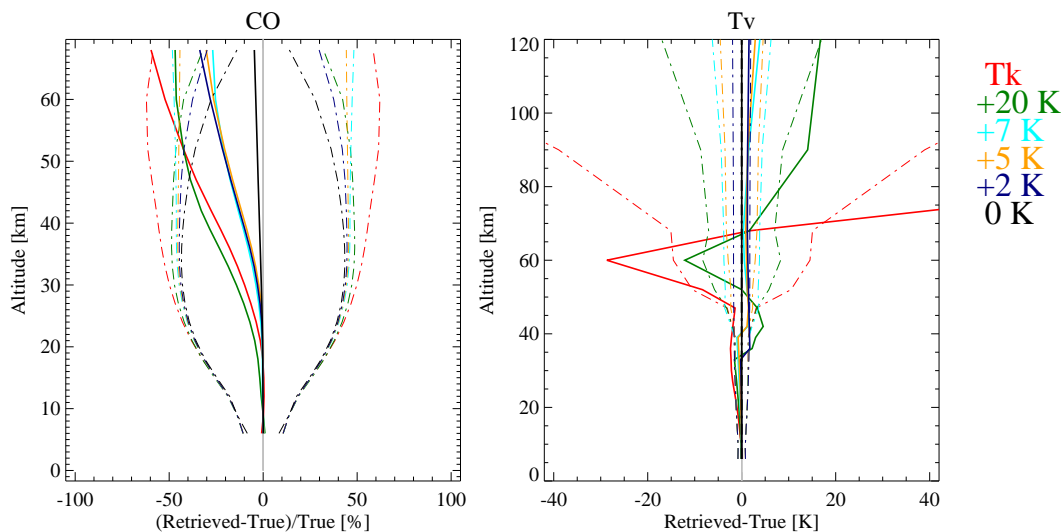


Figure 3.17: As in figure 3.15 but with upper-atmosphere column retrieval of CO.

Conclusions

Various simulations were presented for a CO only atmosphere modelled under mid-latitude daytime conditions. For a successful retrieval of CO, the vibrational temperature needs to be known to a high degree of accuracy *a priori*. Simulations suggest that this is to within 5–7 K. The requirements for T_v are less strict if the *a priori* is an underestimate of the truth, and underestimates of 20 K resulted in a retrieval bias in CO of less than 15 %. When there is no knowledge of the T_v profile, and T_k is used as an estimate of T_v with a suitably loose constraint, retrieved CO is increasingly influenced by the *a priori* estimate above 40 km. Since the magnitude of the non-LTE effects is strongly affected by the mesospheric CO abundance, simulations were performed including an upper-atmospheric column retrieval of CO. Although the tolerance for the prior estimate of T_v is more severe, all cases were retrieved to within 20 % of the truth for underestimates, except for the case where there is no prior knowledge of T_v . Biases were larger in the overestimated cases. However, a column retrieval of CO, in addition to the extra

levels inserted in the T_v profile, may not be feasible due to the limited information content of the spectra.

3.6.3 Preliminary T_v climatology

Simulated retrievals suggest that a very good prior knowledge of T_v is needed for the successful retrieval of CO, to within at least 5 K, and that departing from the kinetic temperature profile is not sufficient. To improve the prior estimate of T_v , an accurate climatology is needed. However, the large number of parameters involved, for example: solar flux, radiative transfer between layers and V-V transfer, amongst others, means that creating an accurate climatology of T_v is difficult. The problem consists of setting up a large number of model runs, which sample the parameter space appropriately, and then selecting the most suitable non-LTE populations to generate prior data for a given retrieval.

The GRANADA non-LTE model was used to create an ensemble of 288 model profiles of the non-LTE populations of CO(1-0), accounting for CO VMR and kinetic temperature in 6 latitude bands (90:65N/S, 65:20N/S, 20:0N/S) in 4 seasons (January, April, July, October), according to the IG2 Climatology Database v3.1 (Remedios et al., 2007). Since T_v is highly dependent on the absorption of solar radiation, calculations were performed at 12 solar zenith angles (0, 30, 60, 80, 90, 95, 98, 100, 102, 110, 115, 180°), with denser sampling across the terminator where illumination conditions change rapidly. Solar excitation leads to increased populations of CO(1) in the illuminated part of the LOS compared to the dark part by as much as one order of magnitude which can lead to significant errors in the forward radiance calculation if unaccounted for (Funke et al., 2008). Although gradient of non-LTE excitation is not accounted for explicitly, denser sampling across the terminator allows for

a range of conditions to be modelled according to changing illumination conditions. Two versions of the climatology were produced. The first considers only radiative non-LTE effects. The second also includes the most important V-V collisional processes (i.e., excitation by molecules also in non-LTE) between $N_2(1)$ and $CO(1)$, as shown in equation 3.5. This involves running a fully coupled model of the non-LTE processes involving CO_2 , N_2 , O_2 and $O(^3P)$, see López-Puertas et al. (1993) for further details. Although, when properly characterised, the V-V version should provide a better estimate of the T_v structure, we are faced with the problem of determining a climatology for the collisional partners, in particular $O(^3P)$, which depends strongly on solar zenith angle. These refinements are beyond the scope of this thesis but would be a necessary area for future development.

The non-LTE populations depend on the kinetic temperature, see equation 3.6. However, rather than simply assuming a climatological profile, it is possible refine calculations on a profile-by-profile basis using the retrieved T_k to adjust the tabulated population ratios. When the observed kinetic temperature, T_k , is close to the tabulated kinetic temperature, T_{k0} , an adjustment to the non-LTE to LTE populations ratio, r_m , for the fundamental transition may be calculated as

$$r_m(T_k) = A + (r_m(T_{k0}) - A) \exp \left[\frac{hcE_a}{k} \left(\frac{1}{T_k} - \frac{1}{T_{k0}} \right) \right] \quad (3.9)$$

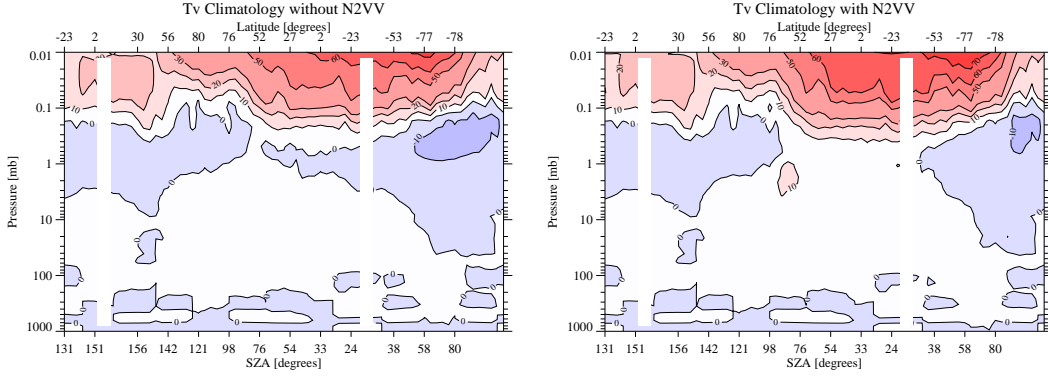
where E_a is the energy of the 1st excited state with respect to the ground state, and A is a factor depending on the Einstein coefficient of spontaneous emission for the transition (*B. Funke personal communication*). The vibrational temperature is then related to $r_m(T_k)$ through equa-

tion 3.6 given in section 3.3.1. The adjustment to the populations ratios given in equation 3.9 does not, however, account for the change in radiative transfer between layers that would result due to the difference in observed and tabulated T_k . The errors that result from this approximation are discussed in section 3.6.3.

As an example, figure 3.18 shows the non-LTE excitation ($T_v - T_k$) fields generated for orbit#09155 on 30th November 2003 both with (see figure 3.18(a)) and without (see figure 3.18(b)) $N_2(1)$ V-V processes included. Interesting features to note in both climatologies are high values of T_v in daylight scans, particularly in the polar summer regions, due to the prolonged sunlight and long path length through the upper atmosphere in this region. Also, a minimum in T_v is seen in most regions around 1 mb where radiative upwelling dominates resulting in $T_v < T_k$. Figure 3.18(b) includes N_2 V-V processes, which are important in the stratopause region. The subsequent effect on mesospheric T_v then mainly depends on the kinetic temperature around the stratopause and the predominance of upwelling radiation. Figure 3.18(b) shows that including the $N_2(1)$ V-V processes increases T_v in the mesosphere in most regions. The largest effect is seen in the polar summer scans, where the stratopause is particularly warm, and additional upwelling radiation due to the V-V collisional excitation of $CO(1)$ in this region has a significant effect on mesospheric $CO(1)$ populations.

Characterisation of errors

Characterisation of errors is not straightforward. However, some reasonable estimate must be made so that the *a priori* uncertainty on T_v used in the retrieval is appropriate. There are many uncertainties to be considered including:



(a) Without V-V coupling between $N_2(1)$ and $CO(1)$ (b) Including V-V coupling between $N_2(1)$ and $CO(1)$

Figure 3.18: Non-LTE enhancements ($T_v - T_k$) generated from non-LTE populations climatology for orbit#09155 on 30th November 2003.

- **Representation of climatological variables:** Spatial and seasonal distribution of T_k , CO and V-V collisional partners used to calculate tabulated populations ratios.
- **Interpolation errors:** errors introduced from interpolation between tabulated non-LTE to LTE populations ratios for the date, geolocation and SZA of a particular retrieval.
- **Errors in non-LTE modelling:** e.g. cloudiness unaccounted for and interference from hotbands of ozone in non-LTE neglected.
- **Errors from parameterisation:** Errors introduced from neglect of radiative transfer between layers in equation 3.9.

Since a full investigation of all the sources of error listed above is beyond the scope of this thesis, we limit the discussion to the error introduced by the parameterisation given in equation 3.9, which does not adjust radiative transfer between layers.

Upwelling radiation from the stratopause region has a significant effect on the T_v structure of the mesosphere, and differences between the observed and tabulated T_k in this region produce the largest errors in the

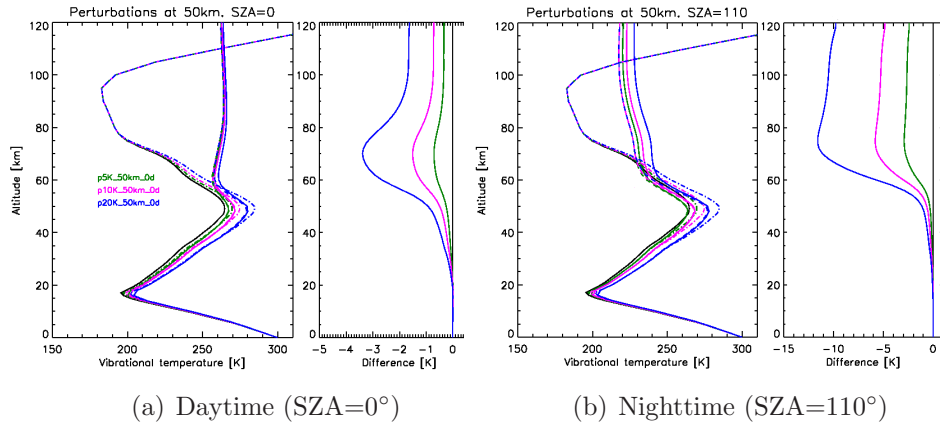


Figure 3.19: Error introduced from parameterisation given by equation 3.9. Perturbations to T_k of 5, 10 and 20 K centred on 50 km. Dot-dashed lines show perturbed T_k profile. Dashed lines show T_v profile calculated using parameterisation in equation 3.9. Solid lines show T_v profile calculated non-LTE model GRANADA for perturbed T_k profile. Differences between the parameterisation and the full non-LTE model calculations are shown in the right-hand panels.

parameterisation. Figure 3.6.3 compares T_v calculated using equation 3.9 against T_v calculated using the GRANADA non-LTE model. Calculations include N_2 V-V coupling. For very large $T_k - T_{k0}$ of 20K around 50 km, the parameterisation typically underestimates mesospheric T_v by up to around 4 K under daytime conditions, and by up to around 10K under nighttime conditions, see right-hand panels.

Further characterisation of prior uncertainties is an important area for future study. However, for the retrievals presented in this thesis, an *ad hoc* estimate of uncertainty has been used that allows generously for the parameterisation errors described above, as well as other potential errors. Uncertainties assigned for use in retrievals from real data are listed in table 3.2 for the various cases considered.

3.6.4 CO climatology

Prior CO is derived from the climatology by Remedios et al. (2007). An *a priori* uncertainty of 100 % of the profile value is typically used during the retrieval. However, concentrations inside the vortex may exceed 10 times that of extra-vortex air. Subsequent mixing of vortex air with the surrounding stratosphere leads to highly variable concentrations in this region. It is suggested that the *a priori* estimate of uncertainty in this region should be increased.

3.6.5 Retrievals from real data

Joint retrievals of CO, T_v were performed using MORSE from FR17 data. Non-LTE microwindows were selected that maximise information about both CO and T_v , using “generic” T_v profiles for daytime and nighttime mid-latitude and equatorial conditions, polar summer and polar winter conditions, produced using the GRANADA model. Interfering species were retrieved beforehand, and cloud contaminated sweeps removed.

Some additional difficulties are encountered when performing retrievals from real data. Unlike in simulations, the T_k profile is not known above the top tangent altitude. This means that it is only partially possible to determine the non-LTE excitation in the mesosphere in the current set-up. In addition, the retrieval levels used in MORSE differ from those used in simulations. As of yet, it is not possible to specify a different number of retrieval points for jointly retrieved species. Therefore, the 68 km retrieval point for T_v is moved to 80 km, where a perturbation is applied centred on 80km, which is triangular between 60 and 90 km, instead of the two additional points that were introduced in simulations at 90 km and 120 km. Retrievals are performed with an upper-atmosphere

column retrieval of CO. A set of retrievals are also performed which ignore the upper-atmosphere altogether, where the top retrieval point is at 68 km, assuming that $T_v = T_k$ above this altitude.

CASE 1: T_k a priori with UA retrieval																			
Altitude [km]	6	9	12	15	18	21	24	27	30	33	36	39	42	47	52	60	68	80	120
SD	T_v [K]	2	2	2	2	2	2	2	2	2	2	2	3	5	20	45	100		
	CO [%]	100
CASE 2 a): Radiative T_v a priori without UA retrieval																			
Altitude [km]	6	9	12	15	18	21	24	27	30	33	36	39	42	47	52	60	68	80	120
SD	T_v [K]	2	2	2	2	2	2	2	2	2	2	2	3	5	10	15	20		
	CO [%]	100
CASE 2 b): Radiative T_v a priori with UA retrieval																			
Altitude [km]	6	9	12	15	18	21	24	27	30	33	36	39	42	47	52	60	68	80	120
SD	T_v [K]	2	2	2	2	2	2	2	2	2	2	2	3	5	10	15	.	20	.
	CO [%]	100
CASE 3 a): $N_2(1)$ V-V T_v a priori without UA retrieval																			
Altitude [km]	6	9	12	15	18	21	24	27	30	33	36	39	42	47	52	60	68	80	120
SD	T_v [K]	2	2	2	2	2	2	2	2	2	2	2	3	5	10	15	20		
	CO [%]	100
CASE 3 b): $N_2(1)$ V-V T_v a priori with UA retrieval																			
Altitude [km]	6	9	12	15	18	21	24	27	30	33	36	39	42	47	52	60	68	80	120
SD	T_v [K]	2	2	2	2	2	2	2	2	2	2	2	3	5	10	15	.	20	.
	CO [%]	100
CASE 3 c): $N_2(1)$ V-V T_v a priori with UA retrieval, tighter S_a of T_v																			
Altitude [km]	6	9	12	15	18	21	24	27	30	33	36	39	42	47	52	60	68	80	120
SD	T_v [K]	2	2	2	2	2	2	2	2	2	2	2	2	2	3	5	.	10	.
	CO [%]	100

Table 3.2: Uncertainties in CO and T_v assigned to each profile level for retrievals from real data. Closely spaced dots indicate upper-atmosphere column retrieval of CO.

Biases in the zonal mean

We present zonally averaged retrievals performed on v4.61/4.62 level 1b FR17 data for the 30th November 2003. The *a priori* uncertainty on CO and T_v used in each case is listed in table 3.2. The following configurations are considered:

- **Case 1:** Observed T_k as prior T_v with an UA retrieval of CO and T_v .
- **Case 2:** Climatological T_v as *a priori* considering radiative non-LTE effects only either a) with or b) without UA retrieval of CO and T_v .
- **Case 3:** Climatological T_v as *a priori* considering both radiative and V-V collisional non-LTE effects either a) with or b) without UA retrieval and c) with UA retrieval of CO and constraining T_v to follow the climatology exactly.

Figure 3.20 shows the day-night bias in retrieved CO, normalised by the climatological VMR i.e. $\text{bias} = \left(\frac{\text{CO}_{\text{day}} - \text{CO}_{\text{ngt}}}{\text{CO}_{\text{clim}}} \right) \times 100\%$, for the various cases described above, for the latitude bands between 45:65 N/S, 20:45 N/S and 0:20 N. The retrieved non-LTE excitation is also shown.

In cases 2 a) and 3 b), the atmosphere above the top tangent altitude is ignored. CO VMR remains at its climatological value, and the vibrational temperature is assumed to be equal to the kinetic temperature. Results shown in figure 3.20 suggest that this is unsatisfactory, and that some account must be taken of the state of the upper-atmosphere. For example, in case 3 b) the retrieval compensates for the mesospheric non-LTE excitation that is ignored by increasing CO VMR in the top profile level, with a day-night bias of well over 1000%. In case 2 a), the retrieval also converges to an unphysical solution with the retrieved vibrational temperature drifting towards high values in the lower-atmosphere, accompanied by huge oscillations in the CO profile.

The retrieval performs much better when perturbations are applied to the UA, although results differ according to the prior estimate of T_v . The worst retrieval is case 1, in which T_k is used as the prior estimate of

T_v . Here there is a large positive bias in the daytime retrieval of CO in the 20:45 N band, which extends to over 1000 % around the stratopause. In case 2 b), where climatological T_v is used as *a priori* considering only radiative non-LTE effects, the retrieval performs much better, and the day-night bias is less than 250 % in all cases. When V-V processes are included into the T_v climatology, as in case 3 a), the retrieval is improved somewhat, with biases of less than 190% in all cases.

Case 3 c) shows what happens when the T_v climatology, including V-V effects, is assumed to be correct, which serves to illustrate how wrong we think our climatology might be. We see that the bias in retrievals from some latitude bands is consistently less than in others. For example, the positive day-night bias is greatest in the NH mid-latitude winter band (45:65 N), and least in the SH mid-latitude summer band (45:65 S), and this is common to all examples using climatological T_v as *a priori*. Such a positive bias in day-night CO might imply either that the daytime T_v is overestimated and/or that the nighttime T_v is underestimated in the climatology.

3.6.6 Conclusions and future work

The objective of this investigation was to discover whether a joint retrieval of CO and vibrational temperature, which could potentially be used to process CO operationally, was feasible, or whether time-consuming, on-line calculations of the non-LTE populations within the retrieval process, such as have already been implemented by IAA/IMK, were the only option. A method was presented whereby T_v could be derived within the joint retrieval from a climatology of non-LTE populations, created using an ensemble of model runs that sample the possible parameter space for various times of year, geolocations, and atmospheric

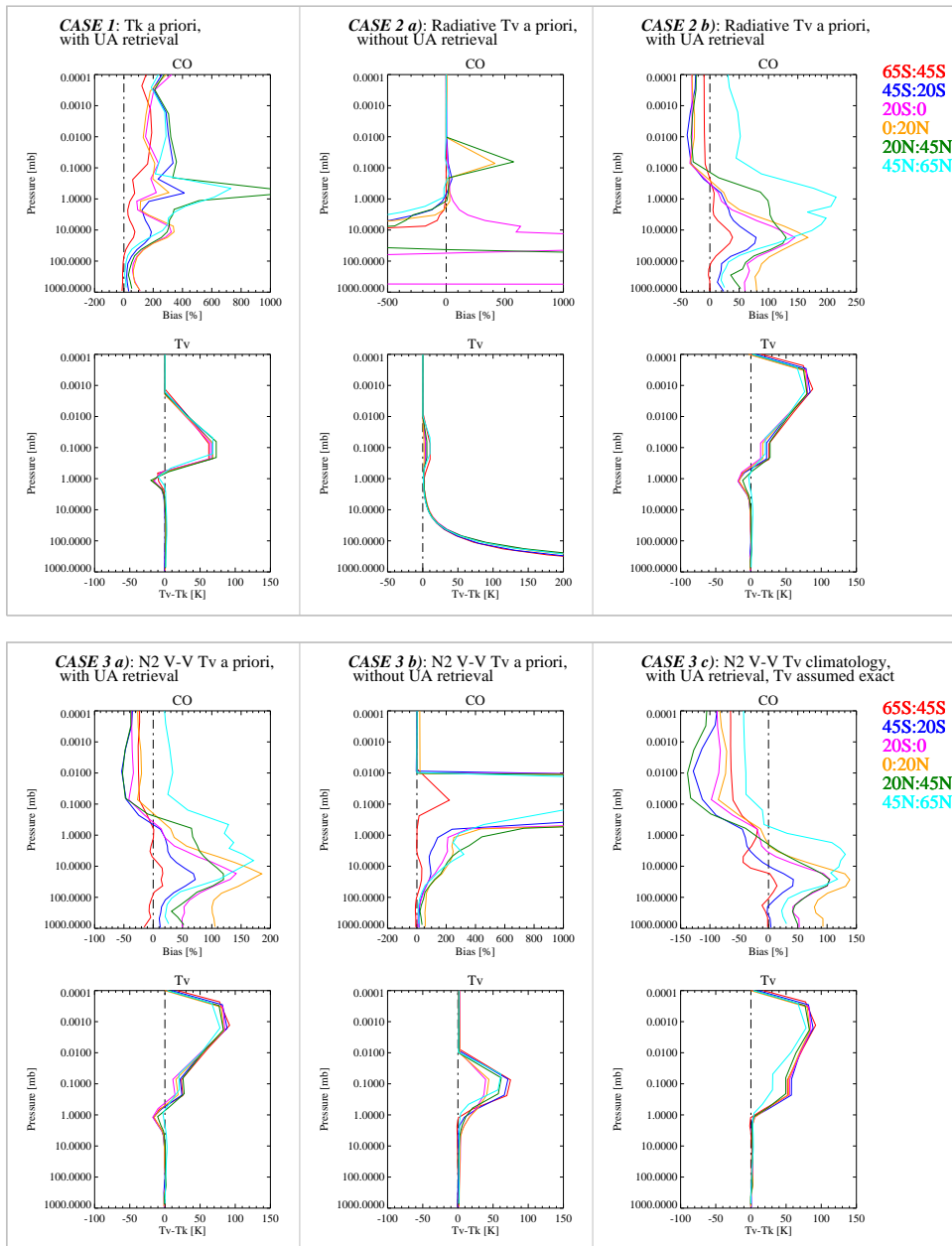


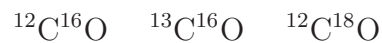
Figure 3.20: Joint retrievals of CO and T_v on real data from 30th November 2003.

conditions, in particular the CO VMR, solar zenith angle and kinetic temperature. Retrievals from real data confirmed that it was necessary to account for the mesospheric non-LTE excitation above the top tangent altitude, either by introducing additional levels in the T_v retrieval, or by moving the top retrieval point to a higher altitude. However, a lack of knowledge about T_k in the mesosphere limits our ability to determine the

mesospheric non-LTE excitation in the current set-up. Retrievals from real data contained significant biases of over 100 %. This is of the same order of magnitude as is commonly seen in retrievals which ignore the non-LTE effects altogether. It appears that to retrieve CO successfully, the climatology of T_v needs to be known to a high degree of accuracy, which simulations suggest may even be to within 1 or 2 K. This can only be achieved by explicit calculations of the non-LTE populations within the retrieval process, as are done currently by IMK/IAA. It seems unlikely that the joint retrieval is viable for the operational retrieval of CO. However, developing the joint retrieval further, as a faster, but less accurate alternative to on-line non-LTE retrieval calculations, would perhaps in any case be of interest.

3.7 Non-LTE effects in CO isotopologues

In addition to emission from the main isotopologue of CO, the spectra also contain isotopic emission lines, see figure 3.4. In order of abundance, the isotopologues present in the Earth's atmosphere are



We observe spectral lines between 2050 and 2060 cm^{-1} belonging to the fundamental transition (1-0) of the P-branch around 4.7 μm . According to the harmonic oscillator model, these transitions are described by

$$\nu_R = \nu_0 - 2BJ \quad \Delta J = +1 \quad (3.10)$$

where ν_0 is the fundamental frequency, B is the rotational constant and J is the rotational quantum number. A heavier isotope rotates more

slowly and, since angular momentum is quantised, has a smaller value of B than a lighter one, meaning that the spectral lines fall to the long-wavelength side and are more closely spaced. The different apparent line strengths are usually thought of as representing the relative abundance of the isotopes in the sample (López-Puertas and Taylor, 2001). However, differing degrees of non-LTE excitation also play a role. Furthermore, if T_v of the minor isotopes differ significantly from the main isotope, then they should be masked from the spectra in the retrieval of $^{12}\text{C}^{16}\text{O}$.

Fundamental band emission of $^{13}\text{C}^{16}\text{O}$ (1.11 % total CO) and $^{12}\text{C}^{18}\text{O}$ (0.204 % total CO) observed from CIRRIS-1A (Cryogenic Infrared Radiance Instrumentation for Shuttle) in the mesosphere and thermosphere (Dodd et al., 1993) was up to 30 times stronger than predicted based solely on the isotopic abundances. This was attributed to stronger excitation in the minor isotopes due to more effective absorption of tropospheric upwelling fluxes than by the main isotopologue (Funke et al., 2007). Non-LTE excitation of $^{13}\text{C}^{16}\text{O}$ has recently been modelled using GRANADA (see Funke et al., 2007). Isotopic emission was enhanced with respect to the most abundant isotopologue with vibrational temperatures around 15 K higher at 60 km at night and around 5 K higher during the day at 60 km ⁸.

For the isotopic lines to be visible above the level of noise, spectra between 60° N/S on 3rd January 2003 were co-added (922 spectra), resulting in random noise error of around $4.5 \times 10^{-3} \text{ nWm}^{-2}\text{sr}^{-1}\text{cm}$. Figure 3.21 shows isotopic spectra, modelled under LTE conditions using the RFM, as well as observed daytime and nighttime spectra and the day-night difference at 60 km. It is evident that daytime radiance for

⁸At night, lack of solar excitation, and therefore smaller populations of the excited state, mean that upwelling flux has a greater effect on $T_v - T_k$ than during the day, when the populations of the excited state are already greatly enhanced.

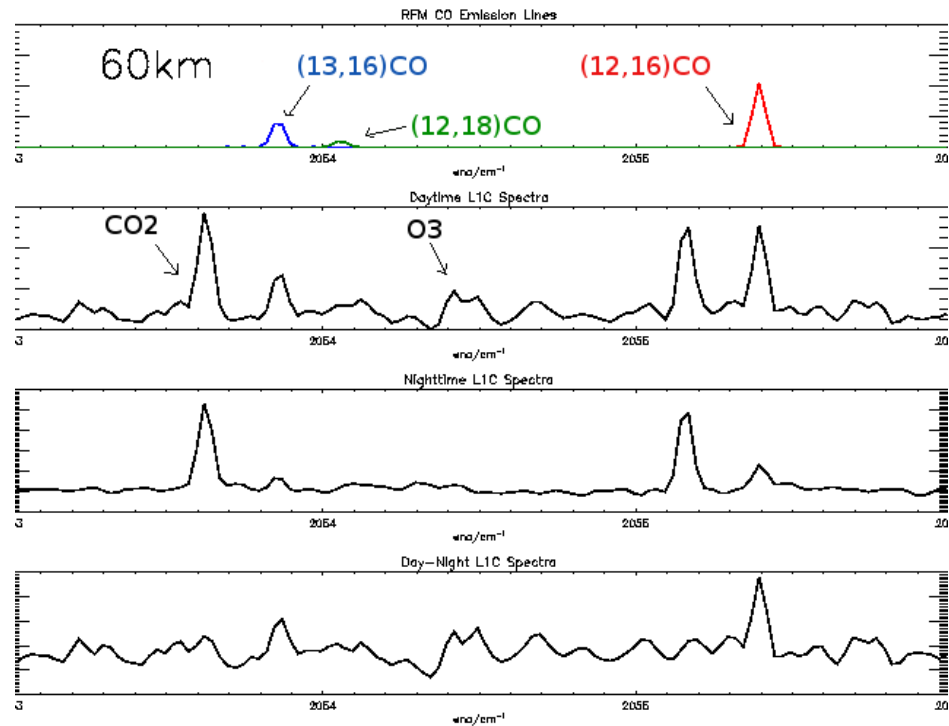


Figure 3.21: Observed and simulated spectra averaged between 60° N/S on 3rd January 2003. From top to bottom the panels show: RFM simulated radiance for CO only, averaged daytime observed spectra, averaged nighttime observed spectra and day-night difference. Note the changes in y-axis scale.

CO is significantly enhanced with respect to nighttime emissions. The peaks visible at around 2053.63 and 2055.15 cm^{-1} are CO_2 lines. The more irregularly shaped features, mainly apparent during the day, are O_3 emission features.

From figure 3.21, it is evident there are differing degrees of excitation in the isotopologues between day and night. We now investigate whether the observed non-LTE enhancements are more pronounced for the less abundant isotopologues. Figure 3.22 shows the observed average daytime radiance plotted against the RFM LTE modelled radiance at tangent altitudes between 33–68km. Ten spectral points, where isotopic emission is strongest, have been used in the analysis, chosen from a window region between 2050 and 2060 cm^{-1} where contributions from contaminants,

mainly CO₂ lines, O₃ and N₂O, are relatively small. The radiance for the isotopologues and contaminants is modelled using kinetic temperatures for each retrieval point used, derived from the ESA level 2 product. Non-LTE effects in the contaminants become significant at high altitudes. However, modelling the non-LTE effects is not feasible for the purposes of this investigation. Instead, a least squares fit is performed of the LTE modelled contaminants to the observations

$$F = ay_{\text{other}} + by_{\text{CO}_2} + c \quad (3.11)$$

where F is the fitted contaminant spectrum, y_{other} is the contribution of all contaminants except CO₂ (mainly O₃), and c is an offset term.

Figure 3.22 shows the observed daytime radiance at 60 km with respect to its LTE modelled value, indicated by the line $y = x$, removing contaminant contributions from the observed spectra as described. The ratio of observed to modelled radiance, which should give an indication of the non-LTE enhancement, was fitted to the data, constraining the best fit line to pass through the origin. The non-LTE enhancement appears, at first, to differ between isotopologues often with greater non-LTE enhancements in radiance for the less abundant isotopes. However, enhancements at lower altitudes, where all isotopologues should converge towards LTE, suggest that these differences may be due to contaminant signal that has not been removed. There are also large errors associated with the fit. Nighttime results are shown in figure 3.23. Non-LTE excitation is in the negative sense at higher altitudes, as expected in the upper-stratosphere, although, once again differences at lower altitudes suggest that the contaminant contribution may be biasing results.

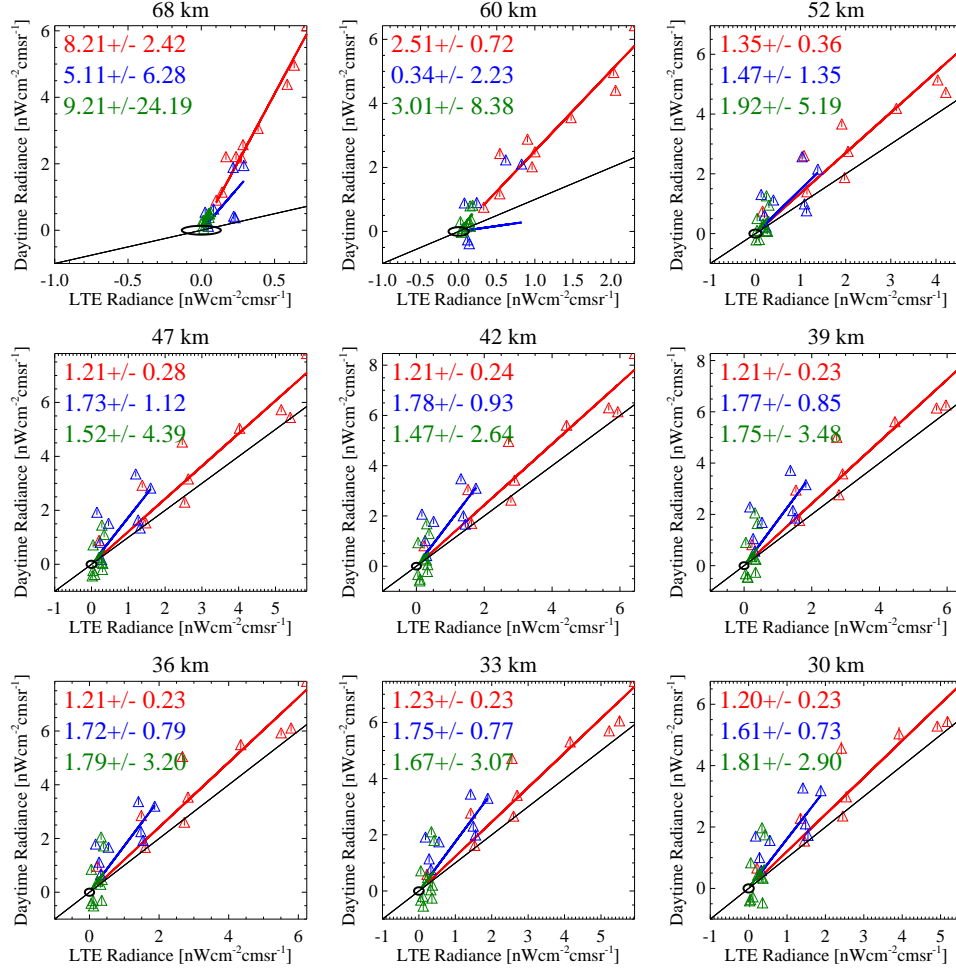


Figure 3.22: Observed daytime radiance averaged between 60° N/S plotted against RFM modelled LTE radiance between 33–68 km.

3.7.1 Estimating T_v of isotopologues

It is possible to derive a simple estimate of T_v by assuming that radiance from the target layer is emitted directly to space

$$\frac{R_{\text{non-LTE}}}{R_{\text{LTE}}} = \frac{\exp\left(\frac{h\nu}{kT_k}\right) - 1}{\exp\left(\frac{h\nu}{kT_v}\right) - 1} \quad (3.12)$$

where $R_{\text{non-LTE}}$ and R_{LTE} are the non-LTE (observed) and LTE (modelled) radiances respectively. The vibrational temperature is then given by

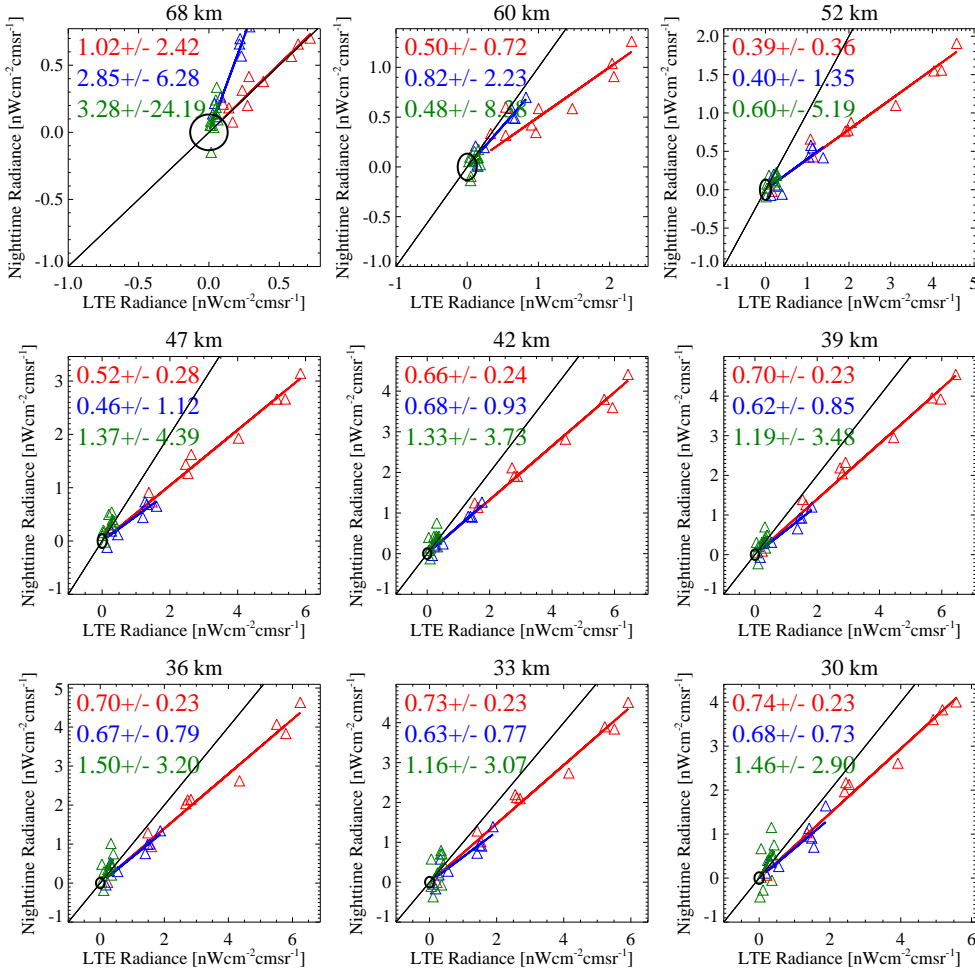


Figure 3.23: As in figure 3.22 but using nighttime spectra.

$$T_v = \frac{h\nu}{k \ln \left(\frac{\exp(h\nu/kT_k) - 1 + R'}{R'} \right)}; \quad R' = \frac{R_{non-LTE}}{R_{LTE}} \quad (3.13)$$

Vibrational temperature profiles derived from day and nighttime spectra are shown in figure 3.24. Vibrational temperatures at night are lower than during the day. There should, however, be no appreciable difference between day and nighttime vibrational temperatures below around 40 km. Differences at these altitudes may imply that the non-LTE contribution from contaminants has not been completely removed.

Vibrational temperature of $^{13}\text{C}^{16}\text{O}$ is higher than $^{12}\text{C}^{16}\text{O}$ at night at higher altitudes perhaps due to the effects of upwelling radiation. This trend is not seen in the daytime data, where the contribution of upwelling flux is relatively less important in the presence of solar excitation. Unfortunately, the difficulties associated with separating the contaminant signal from the isotopic signal leads to spurious values. In addition, fitting $R_{\text{non-LTE}}/R_{\text{LTE}}$ to such weak signals leads to very large errors which, assuming that uncertainty in $R' = R_{\text{non-LTE}}/R_{\text{LTE}}$ is the biggest source, are given by:

$$\Delta T_v = \sqrt{\left(-\frac{BA(R' - 1) - R'}{(\ln(\frac{A+R'}{A}))^2(AR' + R'^2)}\right)^2 (\Delta T_v)^2} \quad (3.14)$$

where $A = \exp(hv/kT_k) - 1$ and $B = hv/k$. These errors are much more significant than the apparent trends in the data, and results are therefore not conclusive.

Conclusions and future work

Currently, the MORSE retrieval uses the T_v profile of the principal isotopologue to model the isotopic lines. Although conclusions cannot be drawn directly from the spectra, modelling studies in the literature suggest that T_v of the less abundant isotopologues differs from the principal form, and that isotopic lines should therefore be masked from the spectra in the retrieval of the main isotope.

3.8 Observations of the hot bands

Hotbands refer to the vibrational transitions $v \geq 2$. At standard temperature and pressure there are very few molecules in the higher excited

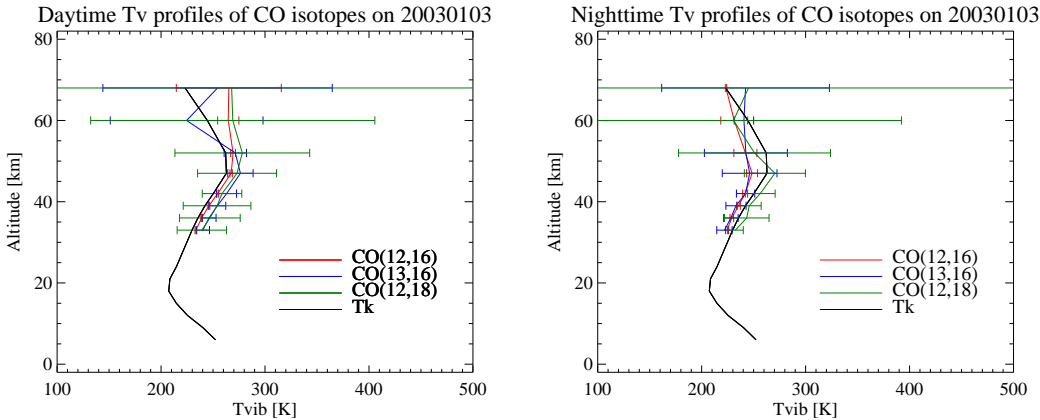


Figure 3.24: Isotopic T_v derived from globally averaged (60° N/S) observations on 3rd January 2003.

states, and so the initial conditions for such transitions seldom exist. However, in hot gases, for example in the the atmosphere of the Sun, or after population by non-LTE processes, the hotbands have increased significance (López-Puertas and Taylor, 2001). We have observed the hotband transition CO(2-1) for the principal isotopologue at high altitude in the Earth's atmosphere. Figure 3.25 shows observed radiances averaged globally between 60° N/S on 3rd January 2003 at 68 km, separated by day and night. Also shown is the day-night difference. The top panel identifies the CO(2-1) transition, modelled using the RFM under LTE conditions between 2140–2160 cm^{-1} . During the day, the population of the CO(2) level is increased due to solar excitation. The CO(2-1) hotband emission is seen clearly in the daytime spectra (2nd panel). At night, in the absence of solar radiation, the populations of CO(2) relax back to their LTE values, and the hotband emission is no longer observed.

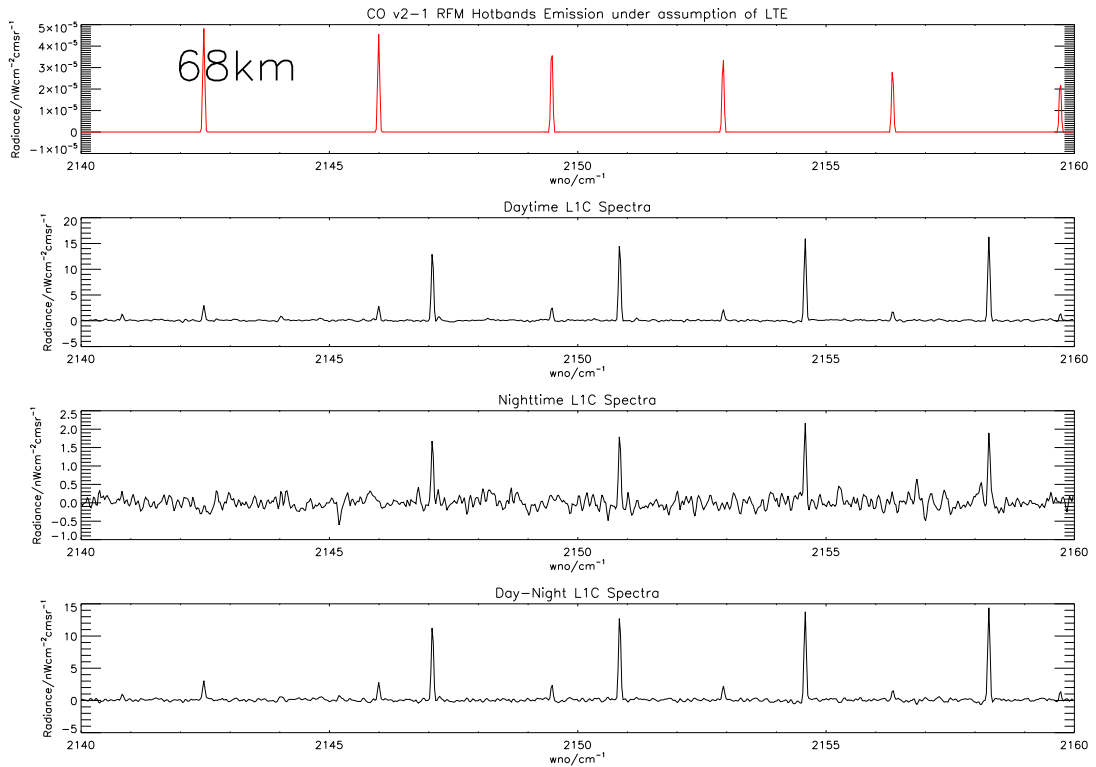


Figure 3.25: Globally averaged observations between 60° N/S of $^{12}\text{C}^{16}\text{O}$ hotbands (2-1) on 3rd January 2003 using v4.61/4.62 level 1b data at 68 km. Top panel shows CO(2-1) emission modelled using the RFM, 2nd panel shows observed daytime emission, 3rd panel shows observed nighttime emission, and bottom panel shows the observed day-night difference. Note the changes in y-axis scale.

3.8.1 Conclusions and future work

Hotbands should also be masked from the spectra in the CO retrieval.

An analysis could perhaps be performed to determine the T_v profile of the hotbands, which could then be compared against calculations using the GRANADA non-LTE model.

Chapter 4

N_2O_5 from MIPAS-ENVISAT

Di-nitrogen pentoxide (N_2O_5) is one of the “big-five” NO_y species (NO_2 , NO , HNO_3 , N_2O_5 , ClONO_2) which together play an important role in stratospheric ozone chemistry and are intimately linked to hydrogen, chlorine, and bromine compounds (Brohede et al., 2008). Di-nitrogen pentoxide is a diurnally varying species, acting as a nighttime reservoir for active nitrogen ($\text{NO}_x = \text{NO} + \text{NO}_2$), which drive the main natural catalytic cycles that remove ozone from the stratosphere (Crutzen, 1970, 1979). It also provides a pathway for the sequestration of NO_x into the odd nitrogen reservoir, HNO_3 , through reactions on the surface of Polar Stratospheric Clouds (PSCs) in the polar winter, and throughout the stratosphere via the reaction of N_2O_5 with the OH radical, as well as through heterogeneous reactions on the surface of sulphuric acid aerosol.

In situ measurements of atmospheric N_2O_5 are unfeasible due to the instability of the compound. Instead, spectroscopic techniques are used, usually exploiting the ν_{21} vibrational band (Smith et al., 1996). However, its weak signal and flat spectral shape make it difficult to distinguish from the spectrally flat background continuum. In this chapter, the retrieval precision of N_2O_5 is improved by altering the retrieval of the

continuum component. A novel method is then presented to validate the improved retrieval by comparing two independently derived estimates of a rate constant associated with its nighttime formation. These estimates can be derived from a single dataset that includes temperature, and the method does not require the use of complicated, often uncertain, chemical transport models.

Concentrations of N_2O_5 are often very low. In the usual optimal estimation retrieval of the logarithm of the volume mixing ratio, an appreciable positive bias is introduced into the retrieval of very small values, caused by the asymmetry of the *a priori* distribution. In the final section, we show that, in simulations, this bias can be removed by performing the retrieval in linear-space.

4.1 Role in the atmosphere

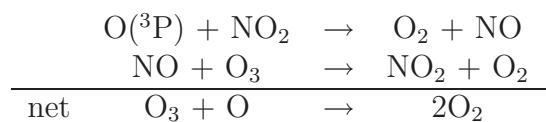
N_2O_5 is a diurnal reservoir for the NO_x gases which are involved in the main natural catalytic cycles via which odd oxygen is removed from the stratosphere. Cycles involving NO_x account for around 45% of the ozone removal in the 25–40 km region (Webster et al., 1990; World Meteorological Organization (WMO), 1985). Following Warneck (1988), ozone is involved in the following cycle in which odd oxygen is conserved;



However, the following reaction involving NO_2 is in competition with reaction 4.1 for atomic oxygen;



Reaction 4.4 is much faster than 4.1, meaning that reaction 4.4 is favoured, even though the abundance of NO_2 is around two orders of magnitude smaller than that of ozone. The NO that is released may then go on to react with ozone. These two reactions together result in a net removal of odd oxygen from the stratosphere with the catalysts, NO and NO_2 , being conserved;

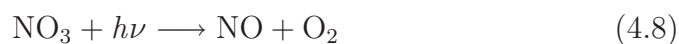


In the lower stratosphere, N_2O_5 provides a pathway for the net removal of NO_x , via hydrolysis on the surface of aerosol, to the more permanent reservoir, HNO_3 (Warneck, 1988).

4.1.1 The diurnal cycle

The diurnal cycle of NO , NO_2 and N_2O_5 is described following Brasseur and Solomon (1986). Figure 4.1 illustrates the diurnal variation of the principal reactive nitrogen species at 30 km.

During the day, the following photolytic processes are important;



At sunrise, the rapid photolysis of NO_2 in 4.5 causes a sudden decrease

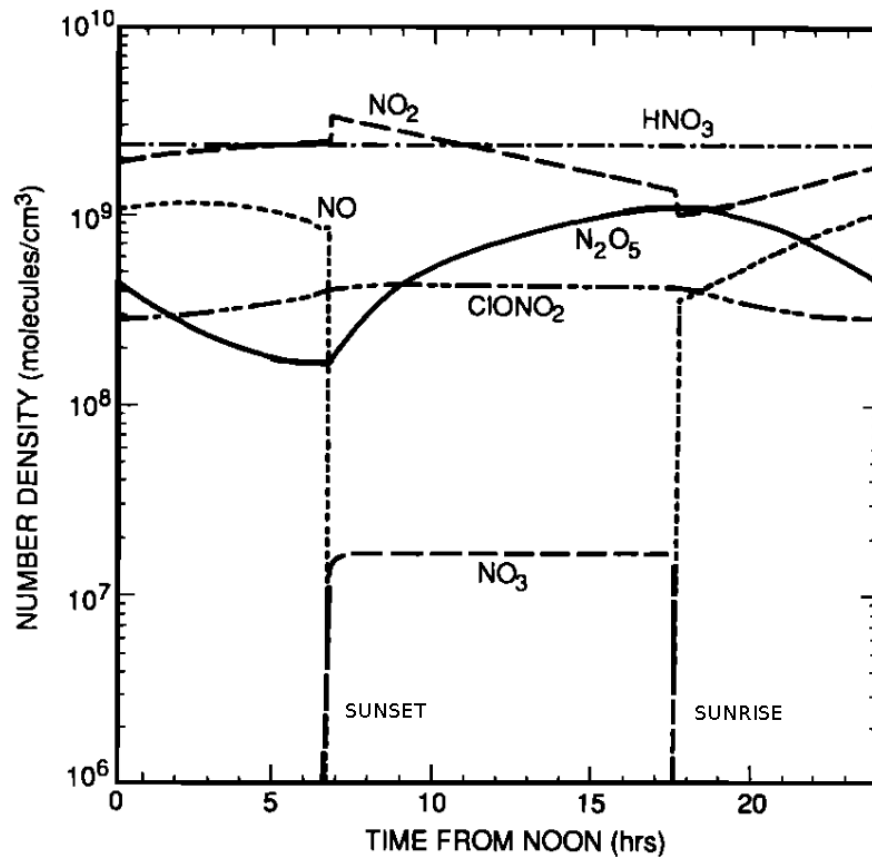
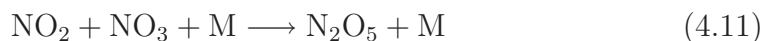


Figure 4.1: The diurnal variation of stratospheric nitrogen species at 30 km (Webster et al., 1990). Labels indicating sunrise/set have been added to the original figure.

in NO_2 and increase in NO concentrations. NO_3 is photolysed almost immediately at sunrise via reaction 4.7 leading to very small daytime densities for this species. However, the photolysis of N_2O_5 , caused by UV radiation in the range 200–400 nm, is much slower and causes a steady decrease in N_2O_5 concentrations during daylight hours. This spectral region corresponds to the most intense absorption bands of ozone – the Hartley bands – which means that the rate of photolysis is a strong function of overhead ozone column and solar zenith angle. As a result, the rate of photolysis of N_2O_5 increases with height, with a lifetime of many days at 30 km decreasing to hours at 40 km (Webster et al., 1990).

The important reactions at night are:



where M is a collisional partner. At sunset, photolysis of NO_2 shuts down. This allows reaction 4.9 to go rapidly to completion, causing a sudden increase in NO_2 and decrease in NO concentrations. Nighttime concentrations of NO become negligible. Photolysis of NO_3 also ceases allowing concentrations of NO_3 build-up at night through reaction 4.10. These conditions then allow N_2O_5 to increase gradually during darkness hours, see reaction 4.11. The formation of NO_3 , shown in 4.10, is the rate limiting step, proceeding much more slowly than reaction 4.11, and so concentrations of NO_3 remain low. Thermal decomposition of N_2O_5 in reaction 4.12 is also ongoing, although stratospheric temperatures greatly favour N_2O_5 formation.

N_2O_5 is converted to HNO_3 in heterogeneous processes on the surface of aerosol;



This reaction is most significant in the lower-stratosphere, below around 30 km, where the aerosol burden is highest. There is also loss of NO_x in the gas phase via the reaction of NO_2 with ClO to form ClONO_2 , with peak production at around 25 km. However, both HNO_3 and ClONO_2 contribute little to decrease nighttime concentrations of N_2O_5

above around 35 km (Nevison et al., 1996).

4.2 Previous measurements

Some of the main space-based measurements of N_2O_5 are listed in table 4.1. Stratospheric N_2O_5 was detected unequivocally for the first time using measurements from ATMOS Spacelab 3 aboard the Space Shuttle (Toon et al., 1986). Later IR emission measurements, from CLAES and ISAMS aboard UARS, had to contend with very high aerosol loadings in the stratosphere, and therefore a large, spectrally homogeneous continuum contribution, due to the eruption of Mount Pinatubo in 1991. Retrievals from these instruments relied on being able to discount the contribution of the continuum above a certain altitude. Retrievals from CLAES assumed that above some transition altitude, determined by total extinction, emission was entirely due to N_2O_5 , and conversely, below that altitude, emission from N_2O_5 was practically zero (Kumer et al., 1996). In a similar fashion, retrievals from ISAMS restricted the altitude range to be above the most intense aerosol loading, beginning at around 30 km (Smith et al., 1996).

Current instruments observe a clearer stratosphere,¹ and have broadband, but spectrally resolving, coverage. The ACE-FTS instrument, which works by solar occultation, is the only instrument other than MIPAS currently measuring N_2O_5 from space. It uses a very wide spectral window from 1210–1270 cm^{-1} containing regions with less continuum

¹The Mount Pinatubo eruption was a massive event. To compare against a recent event that penetrated the stratosphere, the Chaitén Volcano erupted, beginning on the 2nd May 2008, sending plumes of gas and ash to an altitude of around 30 km. However, it is estimated to have emitted only a few thousand tons of SO_2 , which in the stratosphere leads to the formation of sulphuric acid aerosol, compared to an estimated 20 million tons released by Mount Pinatubo in 1991 (http://earthobservatory.nasa.gov/NaturalHazards/natural_hazards_v2.php3?img_id=14821).

Instrument	Platform	Type	Operational	Reference
ATMOS	Spacelab 3	Limb-viewing FTS IR ab- sorption spec- troscopy	May 1985	Allen and Delitsky (1990)
CLAES	UARS	Limb-viewing IR etalon spectrometer	1991–1993	Kumer et al. (1996)
ISAMS	UARS	Limb-viewing IR Broad- band filter radiometer	1991–92	Smith et al. (1996)
ACE-FTS	SCISAT-1	IR FTS solar occultation	2003 –	Wolff et al. (2008)
MIPAS	ENVISAT	Limb-viewing IR FTS spec- trometer	2002–	Mengistu Tsidu et al. (IMK/IAA retrieval, 2004)

Table 4.1: Some previous space-based measurements of atmospheric N_2O_5 concentrations. Table of acronyms included in preface.

contribution. The balloon borne platform MIPAS-B also uses a very wide analysis window between 1220 and 1270 cm^{-1} (Wetzel et al., 1997). However, modelling such a wide spectral region is not feasible for its orbiting counterpart, MIPAS-ENVISAT, which, unlike the balloon-borne instrument, acquires data almost continuously. The IMK/IAA MIPAS-ENVISAT retrieval assumes that there is no significant local spectral variation in continuum and uses an N_2O_5 free microwindow between 1217.725 and 1216.725 cm^{-1} to constrain its contribution in the regions used to retrieve N_2O_5 at 1239.0–1243.0 cm^{-1} and 1275.0–1276.0 cm^{-1} (Mengistu Tsidu et al., 2004).

The paucity of observations and the diurnal variability of N_2O_5 mean that validation is difficult. So far, in validation studies of the IMK/IAA MIPAS retrieval, it is unclear whether the measurements or the CTM (Chemical Transport Model) corrections typically needed to compare measurements, leads to the disagreement. In a comparison of

the IMK/IAA retrieval of N_2O_5 against the chemistry climate model ECHAM-5/MESSy1, the model overestimated the diurnal cycle of N_2O_5 with respect to the measurements. However, it could not be established whether this was due to an incomplete representation of the chemistry, a problem with the photodissociation parameters for N_2O_5 or a problem with the observations (Brühl et al., 2007). In a separate study, ACE-FTS sunset measurements were biased low against the KASIMA CTM corrected MIPAS IMK/IAA measurements, by typically -10% for the daytime comparisons and -27% for the nighttime comparisons. They concluded that the most probable cause of the low bias was uncertainty in the CTM correction (Wolff et al., 2008).

4.3 Improving retrieval precision

In a standard MORSE retrieval, the target gas is retrieved jointly with continuum extinction and a radiometric offset term. The retrieval of the target gas is performed sequentially between microwindows, whereby the result from the previous microwindow is used as the *a priori* estimate for the next. This approach is considered valid since retrieved VMR does not physically depend upon the spectral region used in the retrieval. However, continuum extinction changes with wavelength, and for this reason, an independent retrieval of continuum extinction is usually performed in each microwindow. However, for adjacent microwindows, it is reasonable to assume that continuum extinction does not vary substantially, and that its contribution is correlated between nearby microwindows. We describe an alternative approach where, by using adjacent microwindows and performing a sequential retrieval of the continuum, the retrieval precision of N_2O_5 may be improved.

Simulations of N_2O_5 retrieval precision were performed for a joint retrieval of N_2O_5 , continuum and radiometric offset, with either a microwindow-by-microwindow continuum, (standard approach), in which case the continuum is assumed to be spectrally *uncorrelated*, or else a broadband continuum, in which case the continuum is assumed to be correlated between microwindows. Simulations were performed using the RFM to compute the ν_{21} vibrational band emission between 1230–1260 cm^{-1} at full spectral resolution, as shown in figure 4.3. Nominal B-band NESR of $20 \text{ nWm}^{-2}\text{sr}^{-1}\text{cm}$ is assumed. The region is treated as a set of ten contiguous 3 cm^{-1} wide microwindows. The N_2O_5 *a priori* is set to 100 % of the profile value with no vertical correlations.

The retrieval random error for N_2O_5 using the standard approach is shown in figure 4.2. Precision is poor, with random errors of greater than 70 % throughout the profile. Retrieval random errors for N_2O_5 in the broadband continuum retrieval are also shown in figure 4.2. There are improvements of up to 60 % around the N_2O_5 VMR maximum using this scheme. Treating the continuum component in this way means that there is now more information available about the target species.

As a result of these investigations, the MORSE algorithm was altered (by A. Dudhia) to allow for a broadband continuum retrieval, as an additional option to the original microwindow-by-microwindow retrieval.²

4.4 Retrieval method

In the analysis that follows, retrievals from real data for N_2O_5 and temperature are performed using MORSE from version 4.61/4.62 L1B spec-

²In the MORSE documentation (Dudhia, 2008a) the microwindow-by-microwindow retrieval is described as a “continuum” retrieval and the broadband continuum retrieval is referred to as an “aerosol” retrieval, owing to the spectrally smooth signature that arises from aerosol.

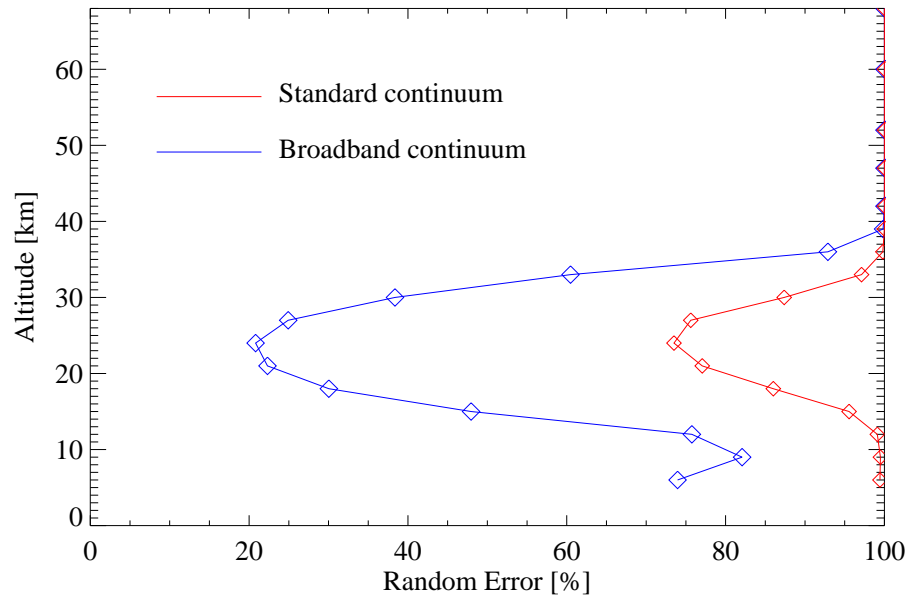


Figure 4.2: Simulated N_2O_5 retrieval random error for joint retrieval of N_2O_5 , continuum and radiometric offset, with either microwindow-by-microwindow or broadband treatment of the continuum.

tra. The broadband continuum retrieval, described in section 4.3, is applied to the retrieval of N_2O_5 . The microwindows used to retrieve N_2O_5 are shown in figure 4.3. Spectroscopic data is derived from the HITRAN database (Rothman et al., 1998; Flaud and Carli, 2003) and includes N_2O_5 absorption cross-section data (Cantrell et al., 1988). Contaminant species, predominantly CH_4 , N_2O and H_2O , are retrieved beforehand for each sweep. Cloud contaminated sweeps, identified using the method by Spang et al. (2004), with a maximum cloud index of 1.8, are removed from the analysis. The *a priori* profile is derived from a climatological database (Remedios et al., 2007) and consists of a mean value that does not include diurnal variation. An N_2O_5 *a priori* uncertainty of 100% of the profile value is assigned with a vertical correlation length of 50 km.

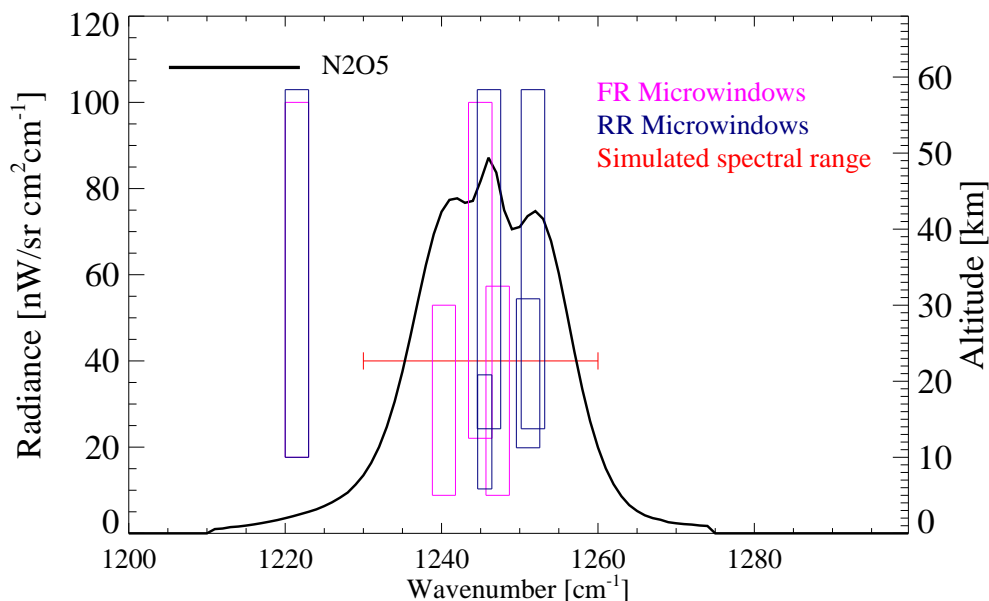
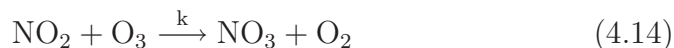


Figure 4.3: RFM simulated N_2O_5 ν_{12} band emission at 30 km. Red bar indicates spectral region used in simulations of retrieval precision. Pink bars show spectral and altitude range (left-hand axis) of FR N_2O_5 microwindows used for retrievals from real data.

4.5 Validation of N_2O_5 retrieval

We present a novel method to validate the retrieval of N_2O_5 by comparing two independently derived estimates of the rate constant for the formation of NO_3 in the stratosphere:



This reaction is the rate limiting step controlling the nighttime formation of N_2O_5 , described by reactions 4.10–4.12 in section 4.1.1.

4.5.1 Standard rate constant

The standard value of the rate constant, k , is computed using the Arrhenius equation. The expression, recommended by DeMore et al. (1997) for use in the stratosphere, contains two experimentally determined pa-

rameters, and otherwise depends exponentially on temperature;

$$k(T) = A \exp\left(\frac{-E}{RT}\right) \quad (4.15)$$

where k is in units of $\text{molecule}^{-1}\text{cm}^3\text{s}^{-1}$, T is kinetic temperature and R is the molar gas constant. The Arrhenius factor $A = 1.2 \times 10^{-13}$ and $\frac{E}{R} \pm \left(\frac{\Delta E}{R}\right) = 2450 \pm 150$. An empirical rule is recommended to calculate the error in k at a particular temperature due to experimental uncertainties;

$$f(T) = f(298) \exp\left(\frac{\Delta E}{R} \left(\frac{1}{T} - \frac{1}{298}\right)\right) \quad (4.16)$$

where $f(298) = 1.15$ and $f(T)$ is a multiplicative factor which gives the upper and lower bounds of k corresponding approximately to one standard deviation. The rate constant is highly temperature sensitive. A Taylor expansion about $T=235$ K ($\Delta k(235) \approx k'(235).3K$) indicates that a 3 K change in temperature at 235 K leads to around a 13% change in the rate constant. MIPAS temperature measurements should be adequate, with an absolute accuracy of better than 3 K (Dudhia, 2007).

4.5.2 Determination of N_2O_5 -dependent rate constant

The same rate constant in units of $\text{ppmv}^{-1}\text{hr}^{-1}$ can also be determined using;

$$k_{\text{VMR}} = \frac{1}{2[\text{O}_3]t} \ln\left(\frac{2\Delta[\text{N}_2\text{O}_5]}{[\text{NO}_2]} + 1\right) \quad ; \Delta[\text{N}_2\text{O}_5] = [\text{N}_2\text{O}_5] - [\text{N}_2\text{O}_5]_{\text{set}} \quad (4.17)$$

where $[\text{NO}_2]$, $[\text{N}_2\text{O}_5]$ and $[\text{O}_3]$ are the nighttime concentrations, in units of

ppmv, t is time since sunset measured in hours and $[N_2O_5]_{\text{set}}$ is the sunset concentration.³ Observational estimates of this rate constant can be used as an indirect validation of the N_2O_5 retrieval, by comparing k_{VMR} against the standard value, k . This approach avoids the use of sophisticated, but often uncertain, chemical transport models. As MIPAS overpasses are at a fixed LST, in order to vary the time since sunset at a particular latitude, observations from different times of year must be used. When calculating the time since sunset, it is necessary to account for delayed onset in the upper profile levels, which may extend to an hour or more, compared to the surface, in the summer months at high latitudes.

The method to compute k_{VMR} was first outlined by Toumi, R. and Pyle, J. A. and Webster, C. R. (1991). The derivation, detailed in appendix A, assumes that thermal decomposition of N_2O_5 is negligible, that $[NO_3]$ is in a steady-state and that loss of NO_2 to the longer-lived reservoirs HNO_3 and $ClONO_2$ can be ignored. Nevison et al. (1996) investigated the validity of several of these assumptions. They used a 1D model of reactive nitrogen chemistry including 12 relevant reactions and found that thermal decomposition of N_2O_5 is significant above around 40 km. They then demonstrated, using a 2D chemical-radiative-dynamical model by Garcia and Solomon (1994), that formation of HNO_3 and $ClONO_2$ over the course of the night becomes significant below around 35 km. Their study suggests that k_{VMR} provides a reasonable estimate of the rate constant in the mid-stratosphere, around the 36 km tangent altitude, where neglect of thermal decomposition and heterogeneous loss are less important. Sunset N_2O_5 is not observed directly but may either be

³Conversion to the more usual units of $\text{molecule}^{-1}\text{cm}^3\text{s}^{-1}$ is achieved by;

$$k_{\text{molecule}^{-1}\text{cm}^3\text{s}^{-1}} = \frac{k_{\text{VMR}} + 1 \times 10^{-6}}{1 \times 10^{-6}} \left(\frac{k_B T}{p} \right) \left(\frac{1 \times 10^6}{3600} \right) \quad (4.18)$$

ignored, or else estimated from the daytime observations using a photochemical model. The concentration of O_3 is assumed to remain constant over the course of the night.

4.5.3 Rate constant from nighttime observations only

The simplest approach is to assume that the sunset concentration of N_2O_5 is negligible. The rate constant k_{VMR} can then be calculated by considering the nighttime data only.

Overview of nighttime data

Daily zonal mean nighttime mixing ratios for the seasonal cycle in the Southern Hemisphere are shown in figure 4.4, for data acquired over the course of the FR mission between July 2002 and March 2004. Similar results (not shown) are obtained for the NH. A day's worth of data from each month is used, typically the 21st, 22nd and 23rd according to data availability. Total proxy NO_x (nighttime $NO_2 + 2N_2O_5$) is also indicated in figure 4.4. This quantity, which is roughly conserved on the diurnal timescale, varies on the seasonal timescale.

Similar results (not shown) are obtained using RR data.

Calculation of k_{VMR}

k_{VMR} is calculated using equation 4.17, assuming that $[N_2O_5]_{set}$ is negligible. The estimate of k_{VMR} is expected to be valid above around 30–35 km, where the timescale for photolysis of N_2O_5 is less than half a day (Nevison et al., 1996). At these altitudes, the sunset concentration is essentially zero, although this depends somewhat upon latitude and time of year.

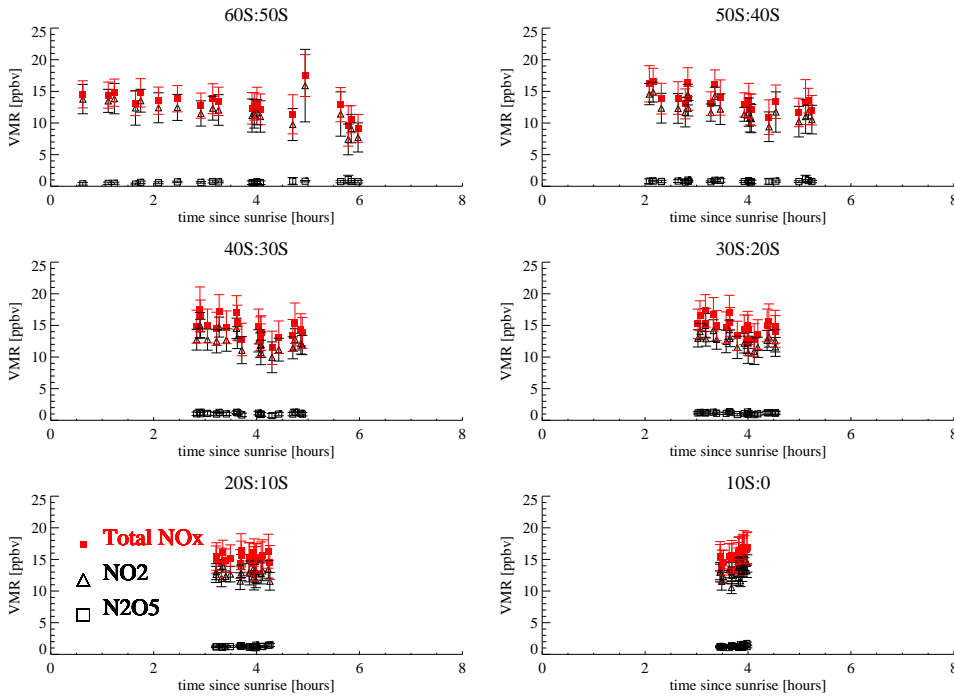


Figure 4.4: Daily zonal mean nighttime observations of NO_2 and N_2O_5 for dates between July 2002 and March 2004 at the 36 km tangent altitude. Error bars indicate scatter in the mean in each latitude band. Total proxy NO_x (nighttime $NO_2+2N_2O_5$) also indicated.

Figure 4.5 shows the results of the comparison of k_{VMR} against the standard value, k , at 36 km. At this altitude, heterogeneous loss and neglect of thermal decomposition of N_2O_5 are only expected to have a small effect on the estimate of k_{VMR} . Smaller times since sunset correspond to the summer months and conversely, larger times since sunset correspond to the winter months. Estimates are grouped by latitude band and hour since sunset. There is a larger range of times since sunset at higher latitudes. The error bars indicate the scatter of the estimates in each bin.

The upwards trend in figure 4.5(a) corresponds to a warmer stratosphere, and, therefore, greater N_2O_5 production, in the summer months. In figure 4.5(b), to aid the comparison, this temperature dependence is removed using the Arrhenius relationship in equation 4.15, and results

are scaled to $T=235$ K. The JPL recommended lower and upper bounds of k at this temperature, calculated using equation 4.16, are shown as dashed lines. There is broad agreement between the estimates. High latitude winter estimates of k_{VMR} , where photolysis is slow and the residual at sunset is significant, are higher than k , however.

4.5.4 Rate constant including daytime observations

Instead of ignoring $[N_2O_5]_{\text{set}}$ in the calculation of k_{VMR} , the daytime observations can be used to estimate the values at sunset.

Overview of the daytime observations

The zonal mean daytime concentrations of N_2O_5 for the SH seasonal cycle are displayed in figure 4.6. Also shown is the mean estimate of sunset N_2O_5 and the variation (scatter) in each latitude band over the annual cycle.

Determining sunset N_2O_5 concentrations

In order to account for non-negligible $[N_2O_5]_{\text{set}}$, the daytime observations are used to estimate the sunset concentrations using a simple photochemical scheme. During the day, N_2O_5 is photolysed by UV radiation. Photolysis is therefore a strong function of overhead ozone column and solar zenith angle, and must be modelled according to altitude, latitude, time of day and season. Photolysis rates have been derived from the TUV (Tropospheric Ultraviolet and Visible radiation model) (Madronich, 2006) using daytime MIPAS observations to supply the required ozone number densities and temperature profiles, which are assumed to remain constant over the course of the day. The model calculates the radiation field and photodissociation parameters under given atmospheric

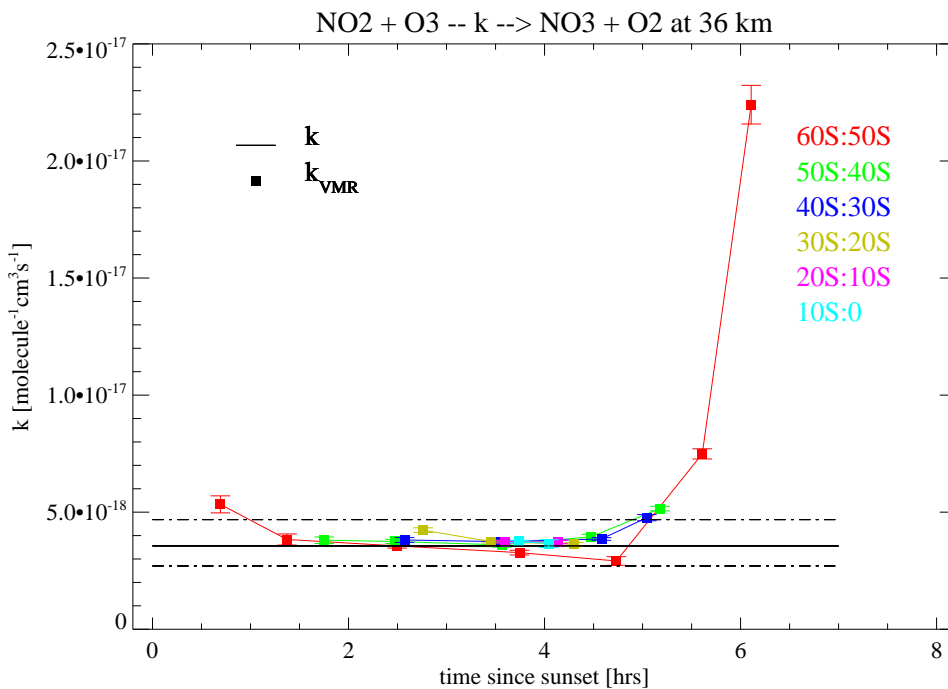
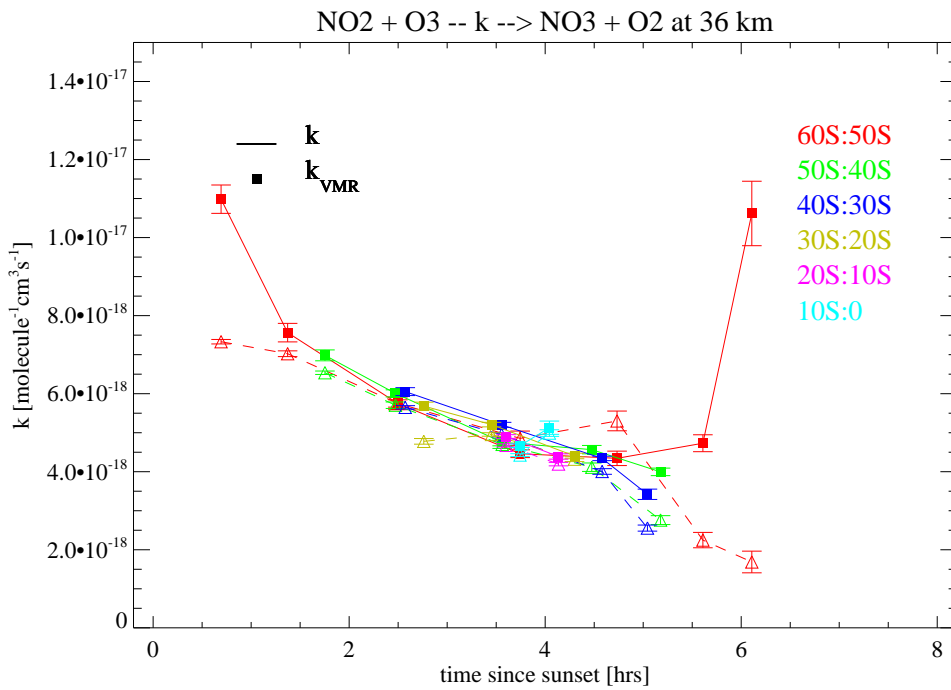


Figure 4.5: k and k_{VMR} (see equations 4.15 and 4.17) at 36 km. Assuming $[N_2O_5]_{\text{set}}=0$.

conditions using the JPL recommended absorption cross sections for N_2O_5 (DeMore et al., 1997; Madronich and Flocke, 1998). Calculations have been performed in a four-stream approximation (Chandrasekhar, 1960; Starnes et al., 1988).

Sunset N_2O_5 is estimated by extrapolating the daytime N_2O_5 measurements to sunset according to;

$$\frac{d[N_2O_5]}{dt} = -J_{N_2O_5}[N_2O_5] \quad (4.19)$$

where $J_{N_2O_5}$ are the photolysis rates derived using the TUV. Integration is performed in 15 minute time steps using a 4th order Runge-Kutta scheme. The contribution of thermal decomposition, given by reaction 4.12, to the decay of N_2O_5 is ignored. Thermal decomposition becomes more significant with altitude but is still over ten times slower than the photolytic decay at 40 km and over 100 times slower at 30 km (Connell and Johnston, 1979).

Rate constant accounting for non-negligible $[N_2O_5]_{\text{set}}$

Figure 4.7(b) shows the estimates of k_{VMR} at 36 km obtained using the daytime observations and TUV to account for non-negligible $[N_2O_5]_{\text{set}}$. Sunset concentrations of N_2O_5 are indicated in figure 4.7(a). The estimates are grouped by latitude band and hour since sunset. The error bars indicate the scatter in each bin. Sensitivity of the photolysis rates to ozone number density can cause large uncertainties in the estimate of $[N_2O_5]_{\text{set}}$, with a 10% change in O_3 at all profile levels producing around a 50% change in $[N_2O_2]_{\text{set}}$ for spring-time observations at mid-latitudes. However, the scatter of the estimates in each bin is usually larger and is used instead as an estimate of uncertainty in $[N_2O_5]_{\text{set}}$.

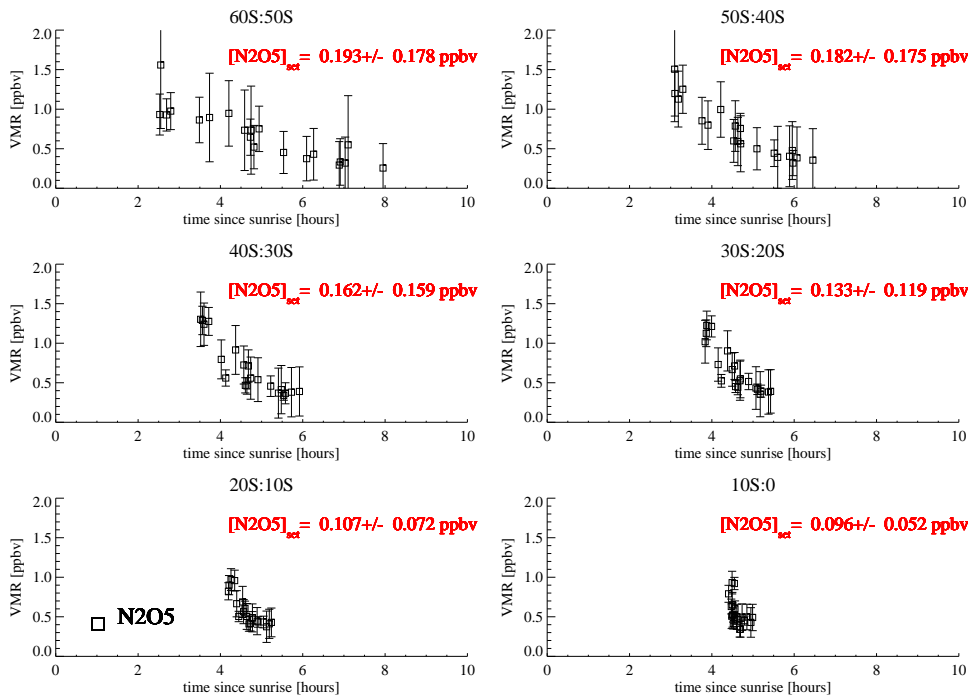
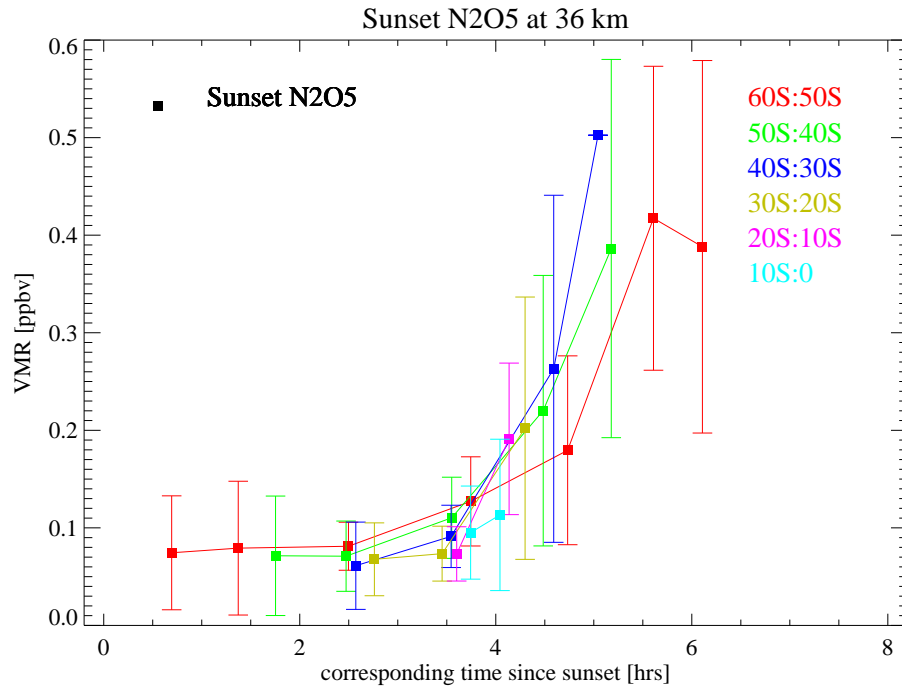
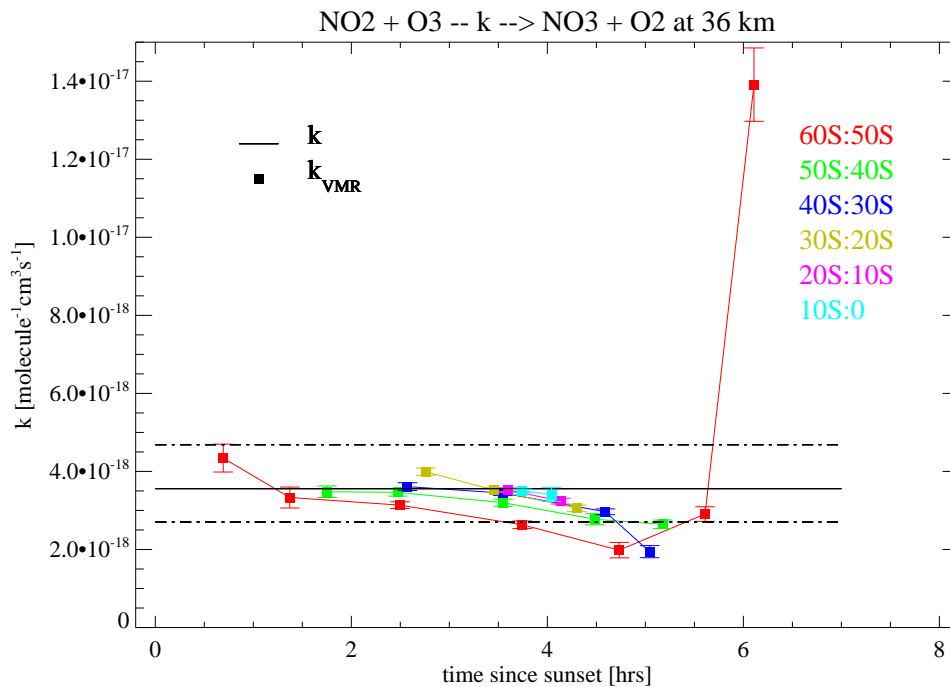


Figure 4.6: Daily zonal mean daytime observations of NO_2 and N_2O_5 for dates between July 2002 and March 2004 at the 36 km. Mean $[N_2O_5]_{set}$ and the variation (scatter) in each latitude band over the annual cycle are also indicated.

Comparing figure 4.7(b) with figure 4.5(b), high latitude wintertime estimates of k_{VMR} now agree with the Arrhenius value, k , within the scatter of the estimates. Values at times close to sunset are also somewhat reduced. Speculatively, the remaining upwards trend at large times since sunset in the 50–60 °N latitude band may be due to the seasonal conversion of NO_2 to the longer lived reservoirs $ClONO_2$ and HNO_3 via N_2O_5 .

Figure 4.8 shows the results of the same analysis at 33 km. At these altitudes heterogeneous loss of N_2O_5 is expected to become noticeable. In the derivation of k_{VMR} in equation 4.17, if the measured value of N_2O_5 is less than the true value, due to some process that has been ignored, then k_{VMR} is an underestimate of the true rate constant given by k . Under these circumstances, loss of N_2O_5 to HNO_3 and $ClONO_2$ over the course

(a) Sunset N_2O_5 calculated using photochemical model(b) k and k_{VMR} with temperature dependence removed.Figure 4.7: Estimates of rate constant scaled to $T=235$ K at 36 km. $[N_2O_5]_{set}$ calculated using photochemical model also shown.

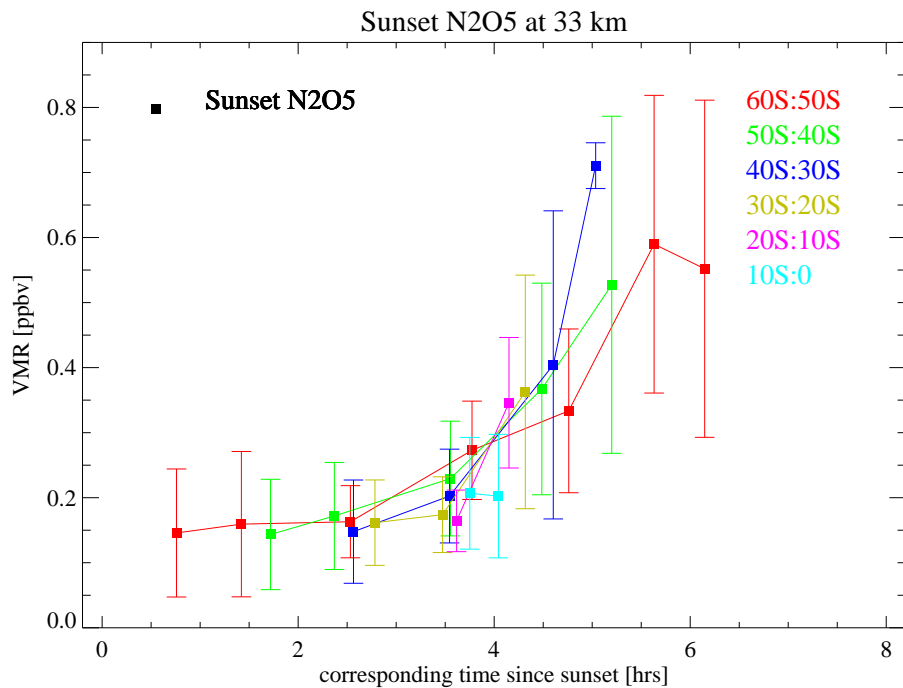
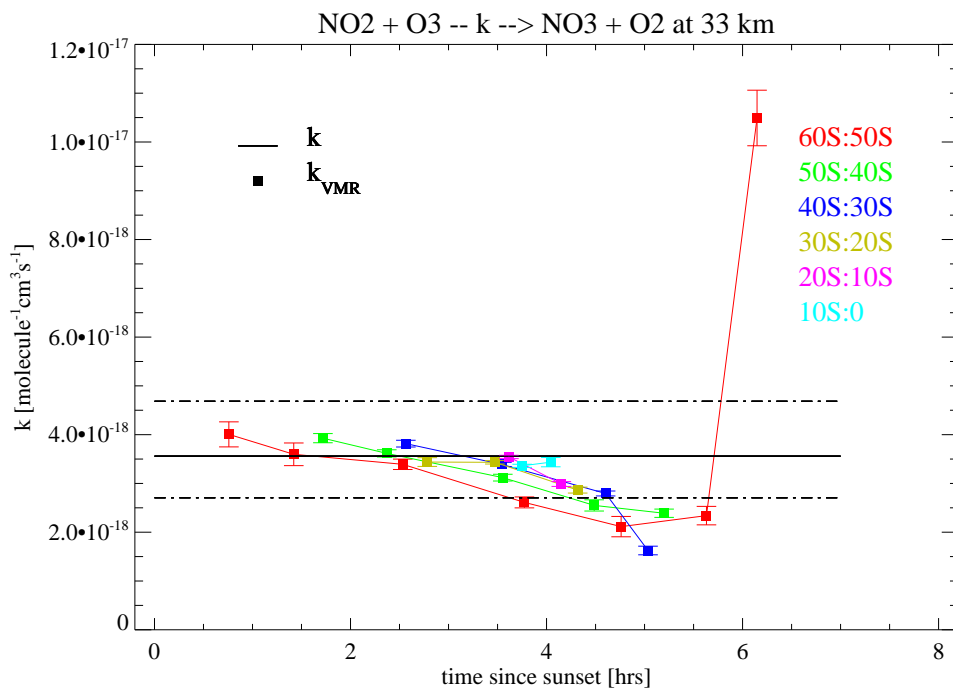
(a) Sunset N_2O_5 calculated using photochemical model(b) k and k_{VMR} with temperature dependence removed

Figure 4.8: As in figure 4.7 but at 33 km.

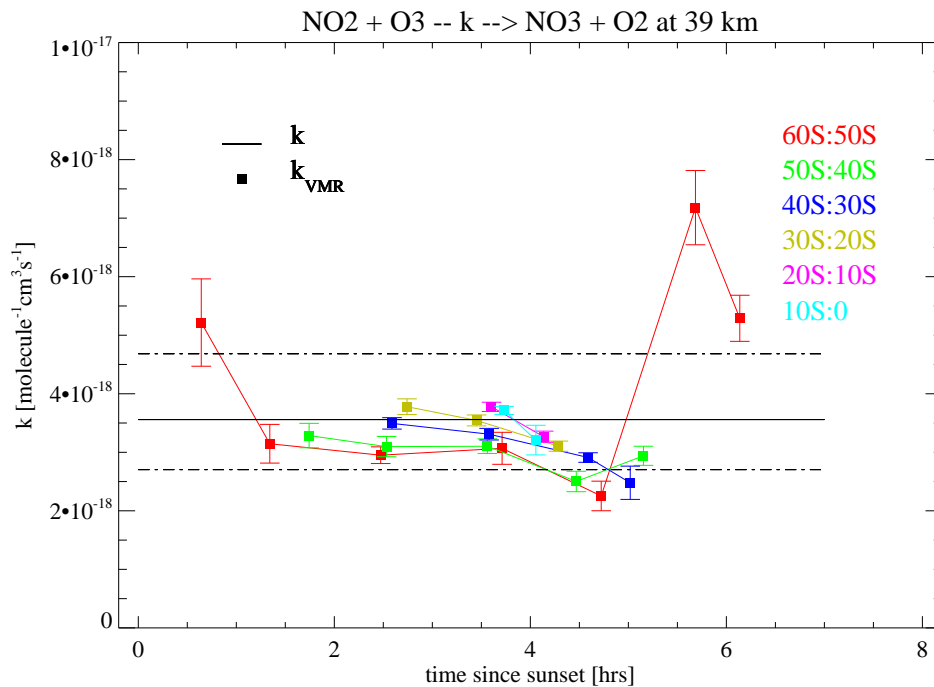
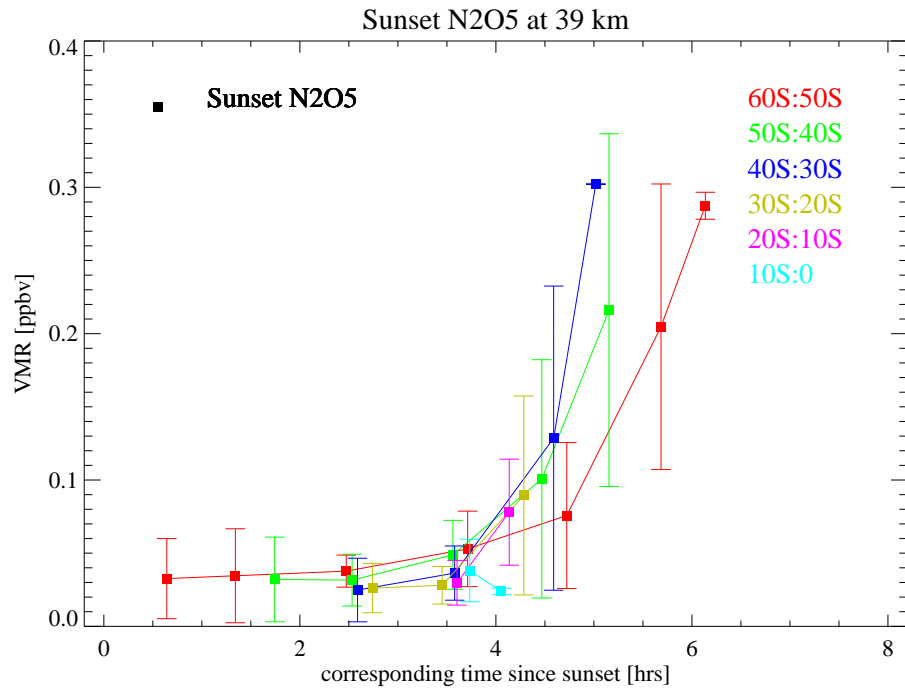


Figure 4.9: As in figure 4.7 but at 39 km.

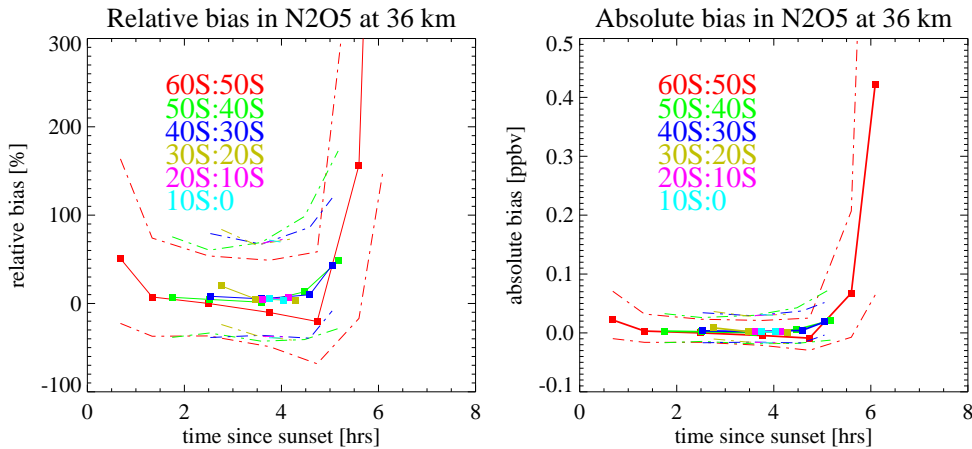


Figure 4.10: Relative and absolute bias in retrieved N_2O_5 at 36 km assuming differences in $(k_{\text{VMR}} - k)$ are entirely due to errors in retrieved N_2O_5 . Dashed lines show upper and lower limits of bias in retrieved N_2O_5 given uncertainties in k_{VMR} and k .

of the night might be seen as a downwards trend in k_{VMR} towards long times after sunset. A prominent downwards trend is indeed evident in figure 4.8(b). However, this trend is absent in calculations not using the TUV (not shown), which suggests that the photolysis may be too slow, leading to an $[N_2O_5]_{\text{set}}$ that is too large, and consequently an underestimate of the rate constant, see the equation for k_{VMR} in 4.17.

Results at 39 km are shown in figure 4.9. At these altitudes, thermal decomposition of N_2O_5 is expected to become significant. Studies by Nevison et al. (1996) suggest that over the course of the night ignoring thermal decomposition can lead to an overestimate in sunrise N_2O_5 concentrations of around 30 % at 40 km. Therefore, neglect of thermal decomposition might be expected to lead to a downwards trend in k_{VMR} towards large times since sunset. There is a hint of such a downwards trend in 4.9 at long times after sunset in all latitude bands, except for high latitude wintertime estimates, where there is an upwards trend, as noted above.

4.5.5 Implied bias in retrieved N_2O_5

Figure 4.10 shows the bias in retrieved N_2O_5 calculated at 36 km, assuming that differences in $(k_{\text{VMR}} - k)$ are entirely due to errors in retrieved values of N_2O_5 . Results are presented for the set of calculations described above assuming non-negligible sunset concentrations. Results are shown in figure 4.10. The relative bias is less than 10 % for equatorial and mid-latitudes. It is much higher in the high latitude summer case at long times after sunset, reaching (not shown) nearly 1000%. There is also a significant relative bias in the high latitude wintertime values, of around 50 %. It appears that MORSE overestimates low values of N_2O_5 . This is investigated further in the following section. Absolute values of the bias in N_2O_5 are also shown in figure 4.10. The implied bias is mostly less than around 0.1 ppbv except for high latitude wintertime estimates.

4.6 Linear-space retrieval of N_2O_5

It is common practice to perform a retrieval of $\ln(\text{VMR})$ rather than VMR. In this way, retrievals with order of magnitude variations (e.g. H_2O) may be performed. In addition, the retrieval of unphysical negative mixing ratios may be avoided. However, when dealing with mixing ratios close to zero, this type of retrieval presents disadvantages. For instance, consider an *a priori* VMR of 1 ppbv with a Gaussian PDF with a standard deviation of 1000% of the quantity being retrieved for both $\ln(\text{VMR})$ and VMR. For the $\ln(\text{VMR})$ retrieval, within 1 SD, we have $0.1\text{ppbv} < \text{VMR} < 10\text{ppbv}$. However, for the retrieval of VMR, we have $-9\text{ppbv} < \text{VMR} < 11\text{ppbv}$.⁴ In the VMR retrieval, the *a priori* proba-

⁴Conversion of log-space errors to linear-space; $\exp(\ln x + \ln(1 + \frac{\delta x}{x})) = x + \delta x$. Error in log-space is approximately equal to the fractional error; $\ln(1 + \frac{\delta x}{x}) \sim \frac{\delta x}{x}$ where x is the state vector and δx is its standard deviation.

bility distribution extends to lower values and should allow us to retrieve values close to zero although, as well as these very small values, it is now also possible to retrieve negative VMR. This requires that the radiative transfer code be altered appropriately, to avoid associated complications such as path segments with a transmittance $\tau > 1$.

4.6.1 Retrieval simulations

A code was written to perform a retrieval of $\ln(\text{VMR})$ and VMR for N_2O_5 retrieved jointly with broadband continuum and radiometric offset. The RFM was used to generate simulated measurements derived from the climatology by Remedios et al. (2007), in the spectral region 1220.075–1223.075 cm^{-1} , assuming a clear atmosphere ($k_{ctm}=0$) with no cloud. The retrieval uses Levenberg-Marquardt optimal estimation with sequential estimation using the RFM as the forward model. The *a priori* uncertainty for N_2O_5 is set to 100% of the profile value with a vertical correlation length of 50 km.

Figure 4.11 shows the retrieved values for the logarithmic and linear-space retrievals for cases where the true profile is 10%, 40% and 80% of the *a priori* profile. The right-hand figure shows the relative bias in the retrieved values with respect to the true values ($\frac{\text{retrieved}-\text{true}}{\text{true}} \times 100\%$). The biases at 33, 36 and 39 km for the various cases are listed in table 4.2 for clarity. In the case where the true value is 10% of the *a priori* value, the linear-space retrieval performs much better than the log-space retrieval at 36 km, with a relative bias of around 40% as opposed to almost 300% for the log-space retrieval. However, in the case where the true profile is 40% of the true value, although the linear-space retrieval performs better, differences are less pronounced. There are negligible differences between the log and linear-space schemes in the case where

the true profile is 80% of the *a priori* profile.

We may compare these results to the bias in N_2O_5 at 36 km calculated in section 4.5.5 for times close to sunset in the high-latitude summer. Under these conditions, the *a priori* estimate is typically around twice the retrieved value. The relative bias in retrieved N_2O_5 was found to be around 50 % in these cases. These values are broadly in agreement with the simulated bias introduced by the log-space retrieval.

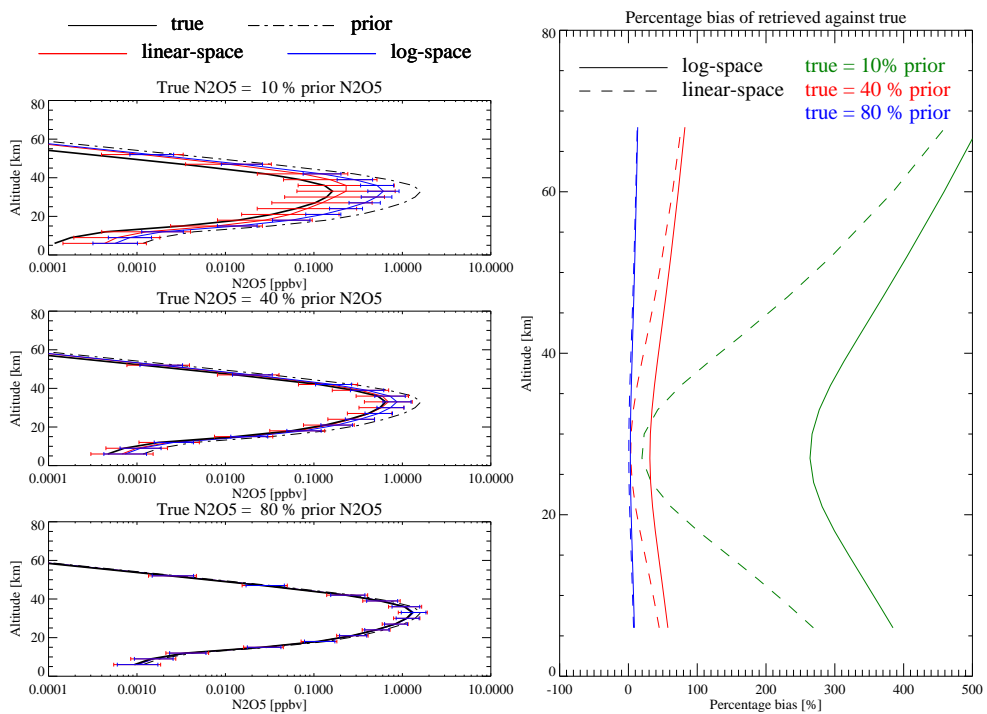


Figure 4.11: Plots on left compare simulated linear and log-space retrievals of N_2O_5 , where the true profile is 10%, 40% and 80% of the *a priori* profile. Plot on right shows the relative percentage bias of the retrieved values with respect to the truth for each case ($\frac{\text{retrieved}-\text{true}}{\text{true}} \times 100\%$).

4.7 Conclusions and future work

In the extra-polar mid-stratosphere, the method of comparing observationally derived rate constants provides a convenient method for the validation of the retrieval of N_2O_5 without the use of complicated, of-

true/prior [%]	altitude [km]	profile bias [%]	
		log-space	linear-space
10	33	117.9	13.3
	36	277.4	42.5
	39	293.6	76.2
40	33	34.2	7.1
	36	37.8	12.7
	39	42.2	19.6
80	33	3.4	1.2
	36	4.2	2.1
	39	5.2	3.3

Table 4.2: Relative percentage bias of in retrieved of N_2O_5 with respect to the true profile in simulations corresponding to figure 4.11.

ten uncertain chemical-transport models. However, uncertainties in the model photolysis rates used to calculate $[\text{N}_2\text{O}_5]_{\text{set}}$, as well as assumptions implicit in the derivation of the $[\text{N}_2\text{O}_5]$ -dependent rate constant, k_{VMR} , complicate the interpretation of the results. Agreement between k_{VMR} , and the standard rate constant, k , is encouraging, however, and there is agreement within the estimate of uncertainty in almost all cases. For equatorial and mid-latitude analyses, the agreement is better without including the TUV, due to uncertainties in photolysis rates. However, determining $[\text{N}_2\text{O}_5]_{\text{set}}$ using the TUV makes a marked improvement to the the high latitude wintertime estimates where the residual at sunset is significant. Speculatively, the remaining high bias in k_{VMR} with respect to k in the high latitude wintertime cases may be due to seasonal loss of NO_2 , via N_2O_5 , to the more permanent reservoir HNO_3 . Downwards trends are observed in k_{VMR} , in figures 4.7– 4.9. The trend at 33 km was attributed to photolysis rates that are too slow. At 39km, the downward trend may be due to thermal decomposition of N_2O_5 over the course of the night. The implied bias in N_2O_5 was then calculated assuming that uncertainty in $[\text{N}_2\text{O}_5]$ was the only source of error in $(k_{\text{VMR}} - k)$. For equatorial and mid-latitudes, the agreement between the rate constants

implies an absolute bias in $[N_2O_5]$ of less than 0.1 ± 0.3 ppbv at 36 km. For mixing ratios close to zero in the high latitude summer, estimates of k_{VMR} imply a relative bias of around 50 % for $[N_2O_5]$ at 36 km. In optimal estimation, such a bias is expected in a log-space retrieval of values close to zero with a higher prior estimate, due to the asymmetry of the *a priori* distribution. In simulations, it was shown that expected bias due to performing the retrieval in log-space was of the same order of magnitude as the bias implied by the rate constant analysis. By performing the retrieval in linear-space, this bias could be removed. The linear retrieval should be tested on real data.

Sunset values derived from daytime MIPAS observation could perhaps be compared against ACE-FTS measurements, although as with other comparisons of this type, it may be difficult to determine whether any discrepancy arises from the photochemical model used to extrapolate MIPAS data or from the retrieved values themselves.

Chapter 5

Long-term measurements of NO_y

A long-term climatology of the majority of NO_y is constructed by combining full and reduced spectral resolution measurements.

Reactive nitrogen species, known collectively as NO_y (NO , NO_2 , HNO_3 , $2 \times \text{N}_2\text{O}_5$, BrONO_2 , HNO_4), play an important role in stratospheric ozone chemistry and are intimately linked to hydrogen, chlorine and bromine compounds (Brohede et al., 2008). In the stratosphere, reactive nitrogen is mostly derived from the oxidation of N_2O . Nitrous oxide is a tropospheric source gas produced by complex denitrification mechanisms in soils (Brasseur et al., 1999a), with an anthropogenic source from the use of fertilizer in agriculture. It enters the stratosphere from the upwelling of tropospheric air in the tropical regions.

Around 90% of N_2O is converted to the unreactive form via photolysis at wavelengths between 190 and 210 nm



However, up to 10 % is converted into a reactive form

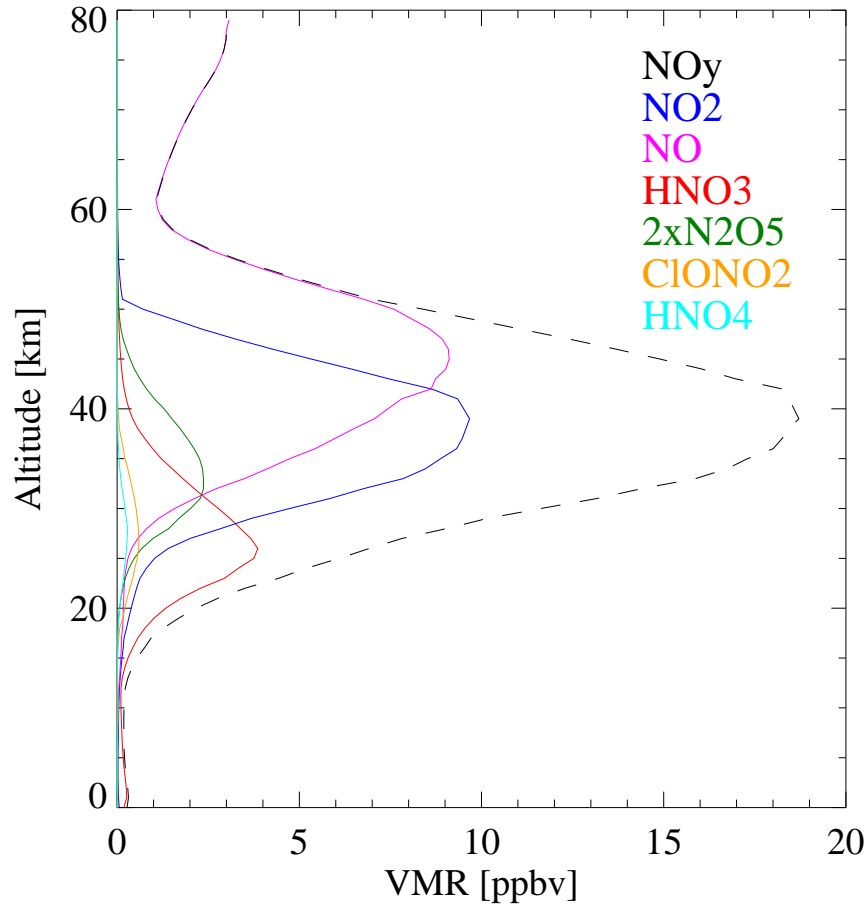


Figure 5.1: Components of NO_y for equatorial conditions derived from climatological values by Remedios et al. (2007). NO_2 , NO and N_2O_5 profiles do not include diurnal variation. HNO_4 , which cannot be measured by MIPAS, accounts for $< 1\%$ of total NO_y .



Excited atomic oxygen $\text{O}(^1\text{D})$ is primarily produced by the photolysis of ozone. Nitric oxide produced in reaction 5.2 combines rapidly with O_3 at sunset to form NO_2



Figure 5.2 shows the numerous reaction pathways leading from NO_2 to

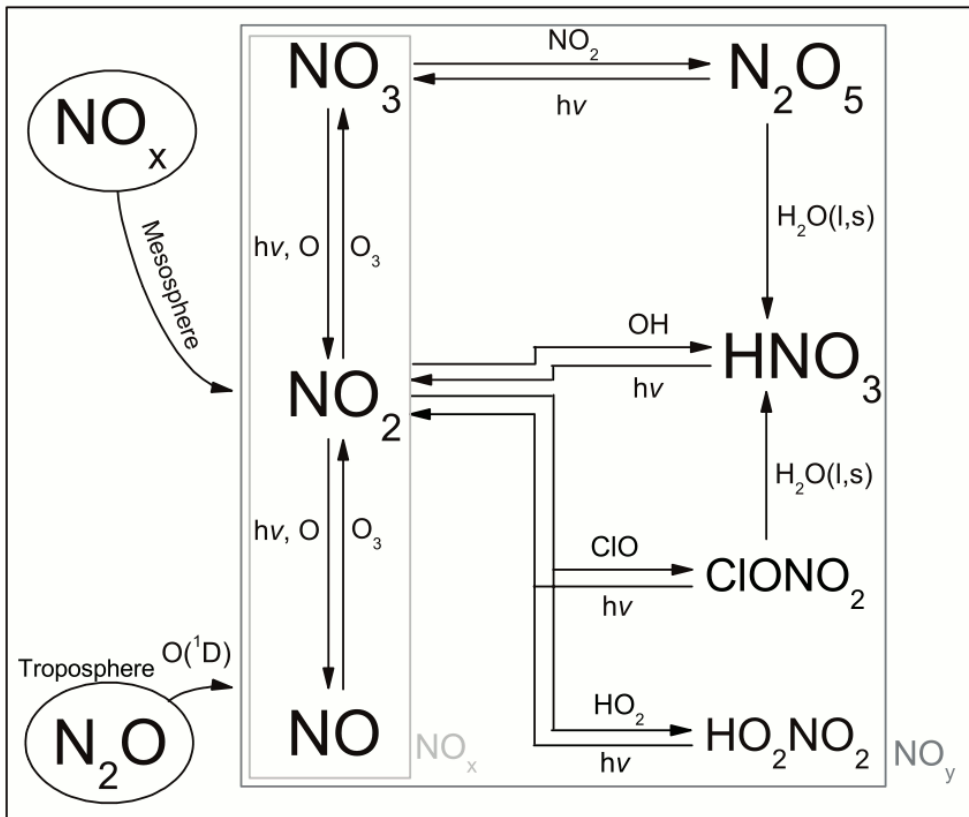


Figure 5.2: Simplified reaction scheme of NO_y (Wiegele et al., 2008).

the other NO_y species. Figure 5.1 shows the approximate partitioning of NO_y for equatorial conditions from the climatology by Remedios et al. (2007). The species NO_2 , NO , HNO_3 and N_2O_5 constitute the majority of NO_y with ClONO_2 and HNO_4 making up only a very small contribution to the total odd nitrogen budget. The contribution of NO_3 (not shown) is negligible.

A second NO_x layer exists in the thermosphere, produced by dissociation of molecular nitrogen by solar radiation and energetic particles. The stratospheric and thermospheric NO_x layers are normally separated by a mesospheric minimum caused by the photolysis of NO and recombination of NO with atomic nitrogen



Photolysis of NO is significant above around 40 km where the abundance of NO_y is increasingly controlled by photochemistry. In the lower stratosphere, NO_y abundance is primarily controlled by transport processes (Brohede et al., 2008).

Large amounts of mesospheric air are transported down to stratospheric altitudes inside the polar vortex by the descending branch of the meridional circulation. The polar vortex is weaker in the Northern Hemisphere due to the effects of elevated topography and increased planetary wave activity, resulting in warmer temperatures and weaker downwards transport than in the Southern Hemisphere. In both hemispheres, the vortex eventually dissipates in spring, triggered by radiative heating (Andrews et al., 1987). The perturbed chemistry inside the polar vortices, resulting from dynamical isolation of the air mass, suppression of photochemical pathways and cold temperatures, and the subsequent distribution of chemically processed air globally upon dissipation of the vortex, plays an important role in stratospheric composition. Large amounts of NO_x are transported to stratospheric altitudes without being photochemically destroyed, and once in the stratosphere is photochemically stable and may contribute to the stratospheric NO_y budget and hence global O_3 variability (Funke et al., 2005; Randall et al., 2001). The principal long-term reservoir of NO_y is HNO_3 , which is formed at all latitudes mainly through reaction with the OH radical or by the heterogeneous reaction of N_2O_5 on the surface of sulphate aerosols, which are always present in the

stratosphere due to the oxidation of biogenic and anthropogenic sulphur species (Brasseur et al., 1999b).



where the subscript (sa) denotes the liquid or solid sulfuric acid aerosol. Volcanic eruptions are a significant source of liquid sulphuric acid aerosol in the stratosphere, although the current aerosol loading is low. The last major event was the eruption of Pinatubo in 1991 which resulted in stratospheric SO_2 loading a factor of 50–100 times higher than present day levels (Brasseur et al., 1999b; Thomason et al., 2007). Nitric acid is also formed inside the polar vortex via N_2O_5 , which builds up rapidly in the darkness of polar winter. Subsequent reactions with type II PSCs, which form in cold temperatures more commonly found in the Antarctic, remove HNO_3 from the gas phase trapping it, leading to denitrification at low altitudes inside the polar vortex, before being returned to the gas phase upon evaporation of the PSC particles in spring. Downwards transport of NO_x inside the polar vortex, especially in the Southern Hemisphere, can lead to global increases in HNO_3 via N_2O_5 after dissipation through ion cluster chemistry in the upper-stratosphere, and/or heterogeneous reactions on sulphate aerosol at lower altitudes (Stiller and et al., 2005).

The principal sink of NO_y is located in the lower-stratosphere either through the washout into the troposphere or dry deposition of HNO_3 to the surface.

5.1 Previous measurements

Solar absorption measurements from ATMOS (Atmospheric Trace gas Molecule Spectroscopy) (Irion et al., 2002; Michelsen et al., 1998) and ACE-FTS (Atmospheric Chemistry Experiment Fourier Transform Spectrometer) (Wolff et al., 2008) are sensitive enough to detect the entire NO_y family (NO , NO_2 , HNO_3 , N_2O_5 , ClONO_2 , HNO_4). However, absorption measurements result in poor data coverage due to the occultation geometry. Atmospheric emission measurements, on the other hand, provide global coverage but generally measure a more limited range of species. Previously, measurements have been combined with other instruments to create a climatology of NO_y . For example, measurements of HNO_3 , ClONO_2 from the infra-red radiometer, CLAES (Cryogenic Limb Array Etalon Spectrometer), were combined with measurements of NO , NO_2 from the solar-occultation instrument HALOE (Halogen Occultation Experiment), both aboard UARS (Upper Atmosphere Research Satellite), to create a post-Pinatubo climatology of NO_y (HNO_3 , ClONO_2 , NO and NO_2), not including N_2O_5 , for January 1992–September 1994 (Danilin et al., 1999). More recently, a proxy NO_y climatology for 2002–2007 was created with NO_2 from the microwave instrument SMR (Sub-Millimeter Radiometer) and HNO_3 from the solar-occultation instrument OSIRIS (Optical Spectrograph and Infra-red Imager System), using a photochemical box model to determine the NO_y species that could not be measured directly (NO , ClONO_2 and $2 \times \text{N}_2\text{O}_5$) (Brohede et al., 2008). In this respect, the MIPAS instrument offers an advantage, providing direct, global measurements of the majority of the NO_y family: NO_2 , NO , HNO_3 , N_2O_5 , ClONO_2 , which together make up 96–99 % of total NO_y (Brohede et al., 2008), as well as providing simultaneous measurements of the

source gas N_2O , allowing for an estimate of NO_x ($=\text{NO}+\text{NO}_2$) production in the stratosphere. Although the FR MIPAS data has already been used extensively to study NO_y , and detailed comparisons of retrieved NO_y against chemistry climate models have been performed for the FR dataset (Brühl et al., 2007), the short time span of the FR mission, lasting less than 2 years, has precluded MIPAS data from use in studies of the long-term behaviour of NO_y , with the majority of MIPAS data, consisting of over 3 years of RR measurements, yet to be exploited, mainly due to difficulties in the adaptation of existing retrieval algorithms to cope with ill-conditioning in the new measurement modes.

In this paper, the FR and RR MIPAS datasets are combined for the first time to construct a long-term, global climatology of NO_y (nighttime NO_2 , HNO_3 , nighttime $2\times\text{N}_2\text{O}_5$, ClONO_2), N_2O and O_3 mixing ratios for the period 2002–2008 directly from the measurements. Direct measurements of NO are strongly affected by non local thermodynamic equilibrium (Funke et al., 2000), and accounting for these effects requires sophisticated modelling of the non-LTE populations.¹ However, since stratospheric NO is immediately converted to NO_2 at sunset, nighttime NO_2 can be used as measure of total NO_x ($\text{NO}+\text{NO}_2$) at altitudes where nighttime NO is negligible (below ~ 60 km) (Brasseur and Solomon, 1986). Di-nitrogen pentoxide is diurnally varying and is measured at night.

¹Very strong thermospheric emission from NO , due to elevated concentrations and strong non-LTE effects, make stratospheric measurements, where the concentration of NO is relatively low, particularly difficult.

5.2 Retrieval method

The available calibrated and geo-located version 4.61/4.62 L1B spectra for the FR modes and version 4.65 for RR modes MIPAS spectra (2002–2008) were processed at the University of Oxford with MORSE (Dudhia, 2008a). For weakly emitting species the retrieval problem is well-known to be ill-conditioned whereby sensitivity of the retrieval to noise results in error amplification that overwhelms the solution, and the retrieved profile is unstable unless some form of regularisation is used. In the RR modes, oversampling of the vertical profile and the location of the retrieval points at the tangent altitudes means that even a strongly emitting species not requiring regularisation on the FR grid needs some form *a priori* constraint. The MORSE algorithm is well suited to this type of problem, as it works on the basis of optimal estimation (Rodgers, 2000) using prior knowledge about the expected atmospheric state in conjunction with the spectral measurements to constrain the possible outcomes and estimate the most probable state. Prior pressure, temperature and volume mixing ratios (VMR) are derived from the IG2 Climatology Database v3.1 (Remedios et al., 2007). The optimal estimate, $\hat{\mathbf{x}}$, is given by

$$\hat{\mathbf{x}} = \mathbf{x}_a + (\mathbf{K}^T \mathbf{S}_y^{-1} \mathbf{K} + \mathbf{S}_a^{-1})^{-1} \mathbf{K}^T \mathbf{S}_y^{-1} (\mathbf{y} - \mathbf{K} \mathbf{x}_a) \quad (5.7)$$

where \mathbf{x}_a is the *a priori* estimate of the state, \mathbf{y} are the spectral measurements, \mathbf{S}_y is the instrument noise covariance, \mathbf{K} contains the forward model jacobians and \mathbf{S}_a is the covariance of the *a priori* estimate. Since the retrieval problem is moderately non-linear, a Gauss-Newton iterative method is used, which for stability, employs Levenberg-Marquardt iterations, introducing a tunable damping factor into the variation of the unknown (Rodgers, 2000). Retrieval precision is given by the propaga-

tion of instrument noise through the retrieval smoothed by the *a priori* error covariance (Rodgers, 2000)

$$\mathbf{S}_x = (\mathbf{K}^T \mathbf{S}_y^{-1} \mathbf{K} + \mathbf{S}_a^{-1})^{-1} \quad (5.8)$$

Optimal spectral regions, known as microwindows, are selected using the measured radiance, which minimise the contribution of systematic errors, such as contaminant contributions, and maximise the information content on the target species (Dudhia et al., 2002). Due to the differing effects of contaminant species, instrumental and modelling errors and vertical sampling at full and reduced resolution, the selected microwindows are not generally the same for the FR and various RR modes. During the retrieval, contaminant species are retrieved sequentially for each sweep followed by a retrieval of the target gas. Retrievals are performed jointly with a spectrally varying offset, or continuum term, mainly to account for unidentified cloud and aerosol or uncertainties in the modelling of line wings, as well as a constant offset to account for errors in radiometric calibration of the instrument. An *a priori* standard deviation of 100 % of the profile value is used to construct \mathbf{S}_a with a vertical correlation length of 50 km. Cloudy sweeps are identified using the cloud index method by Spang et al. (2004). Sweeps with an A-band cloud index > 1.8 are removed. The retrieval of N_2O_5 presents an additional problem relating to its weak, continuum-like signal, which is difficult to distinguish from stratospheric aerosol. For this molecule, the spectral region covered by the microwindows is extended to include the edge of the N_2O_5 band (centred around 1245 cm^{-1}), to include regions of weak N_2O_5 emission where the signal is predominantly from aerosol, thereby helping to fix its contribution.

5.2.1 Random and systematic errors in total NO_y

The random, systematic and total errors were calculated for total NO_y using FR17 and RR27 microwindows. Random errors represent the propagation of noise through the retrieval smoothed by the *a priori* covariance, as given in equation 5.8. Systematic errors are derived from the propagation of errors in the pressure and temperature retrieval, modelling of contaminant species, uncertainties in instrument calibration and forward modelling, as described in section 1.5. The total error in NO_y was calculated by combining the errors in the individual components of NO_y for a nighttime atmosphere from the climatology by Remedios et al. (2007) scaled by the relative abundance. Results are shown in figure 5.3. Over most of the altitude range, systematic errors make a more significant contribution than random error in the full and reduced resolution mode. Total errors of less than 10 % are possible between 21–42 km in the FR17 mode and between 30–47 km in the RR27 mode. The spectral and altitude range of the microwindows used and the random and systematic errors for the individual components of NO_y are included in appendix B.

5.3 Global and seasonal variation of NO_y

5.3.1 Time series

Monthly average time series were calculated for ozone, the components of NO_y and the source gas N_2O , discarding points with a retrieval error of greater than 50 %, thus ensuring the influence of the *a priori* estimate was small. Time series are presented on the 600 K potential temperature surface in the lower-stratosphere at around 30 mb. Zonal aver-

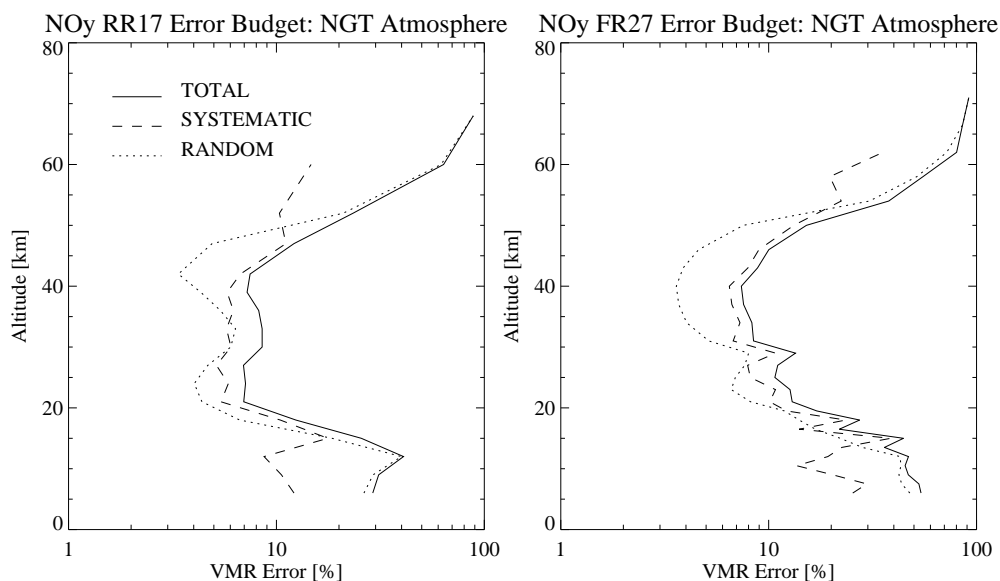


Figure 5.3: Random and systematic errors calculated for total NO_y using FR17 and RR27 operational microwindows.

ages were performed in 5° equivalent latitude bands. The transform to equivalent latitude/potential temperature co-ordinates was derived from the ECMWF T159 relative vorticity product on model levels (BADC ECMWF Operational Analysis data, [Internet]) following the method outlined by Nash, E.R. and Newman, P. A. and Rosenfield, J., E and Schoeberl, M. R. (1996) .²

Figure 5.5 shows the standard deviation for monthly zonal averages in 5° equivalent latitude bins for N_2O , NO_y species (nighttime NO_2 , HNO_3 , nighttime N_2O_5 , ClONO_2) and ozone on the 600 K potential temperature surface. Variability in each bin, mainly due to temporal variations over the course of a month, is usually much larger than the retrieval error due to noise, which is reduced by averaging large numbers of measurements. Regions of very high variability in the monthly average, especially in N_2O , NO_2 , HNO_3 and O_3 , are observed in the SH during the

²Equivalent latitude analysis only works up to around 1000 K, as there are large uncertainties on model wind vectors above. Simple zonal averaging by latitude has been used for $\theta \geq 1000$ K.

to higher latitudes by the meridional circulation from production regions near the equator. In the polar winter regions, the vortex is clearly marked by areas of low N_2O descended from higher altitudes. Chemically processed air inside the polar vortex is high in NO_2 , HNO_3 and ClONO_2 at various times. On the 600 K surface, there are differences between the hemispheres due to colder temperatures in the Antarctic winter. For example, denitrification due to sedimentation of HNO_3 on the surface of PSCs can be discerned towards the end of each SH winter. Mixing ratios of ClONO_2 are lower in the SH polar winter, where the cold temperatures and the presence of man-made halogenated compounds result in ClO being formed preferentially to ClONO_2 , causing O_3 -depletion once photolysis resumes in spring. The ozone hole is visible in the SH spring.

From August 2004 onwards, data is at the reduced spectral resolution. On the 600 K surface, there are systematic differences between the FR and RR NO_2 in the northern hemisphere polar summer as well as at equatorial and mid-latitudes. The mixing ratio of NO_2 retrieved from RR data generally has a low bias with respect to the FR data of up to several ppbv in the NH polar summer and the NH mid-latitudes and polar regions. The minimum in O_3 in the SH winter also appears more pronounced in the RR data. Such differences are likely to be an artefact of changing microwindows, whereby systematic errors propagating through the retrieval are eliminated less effectively in the RR modes. Figure 5.6 shows the random and systematic error components for NO_2 in the FR and nominal RR modes. The 600 K potential temperature surface is situated at around 24 km altitude. Total error in the FR17 mode is 20 % at 24 km, and 28 % in the FR27 mode, mostly due to increased systematic error due to uncertainties in the horizontal temperature gradient. It was

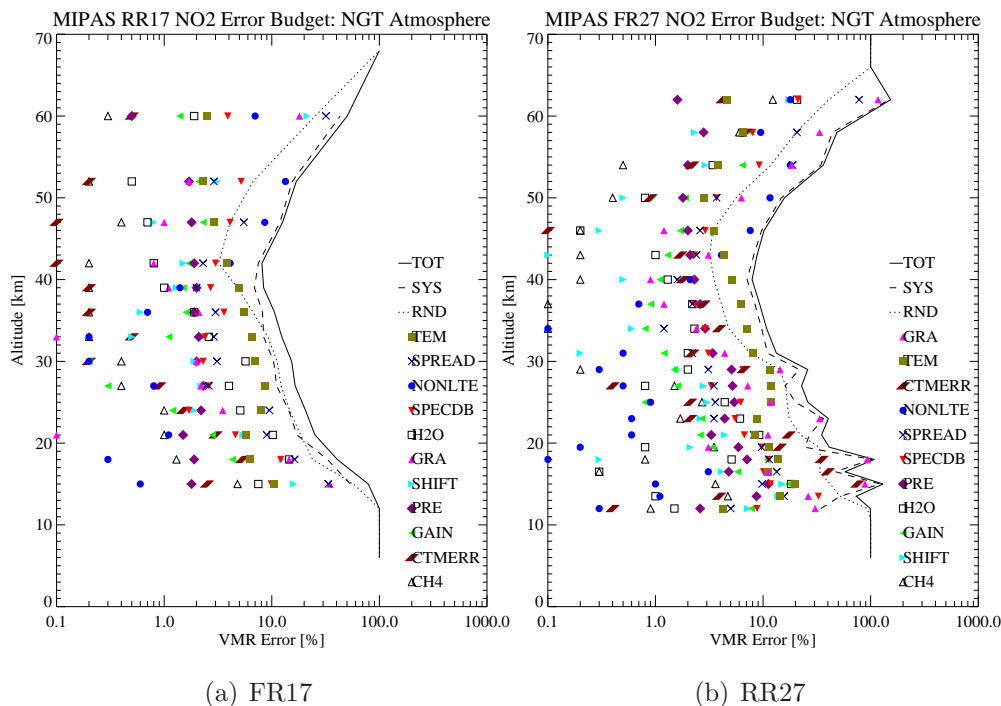


Figure 5.6: Random and systematic errors calculated for NO_2 using FR17 and RR27 operational microwindows.

recently noted by von Clarmann et al. (2009) that consideration of the horizontal temperature gradient improved retrieval quality in the RR modes. A retrieval algorithm Reselection and testing of an optimised set of RR microwindows may remove the apparent bias in reduced resolution NO_2 data leading to better agreement.

Total measurable NO_y (nighttime NO_2 , HNO_3 , $2 \times \text{N}_2\text{O}_5$, ClONO_2) was calculated on potential temperature surfaces spanning the mid to upper-stratosphere (600, 800 and 1000 K). Results are shown in figure 5.7. The corresponding standard deviation is shown in figure 5.8. At 600 K the lifetime of NO_y is long and the annual cycle in NO_y is weak at low latitudes. However, in the polar regions, descent of NO_y rich air is visible, and in the SH denitrification is evident during late polar winter. At the 1000 K surface, the lifetime of NO_y is short, and the distribution is mostly determined by the distribution of the source gas N_2O . The 800 K

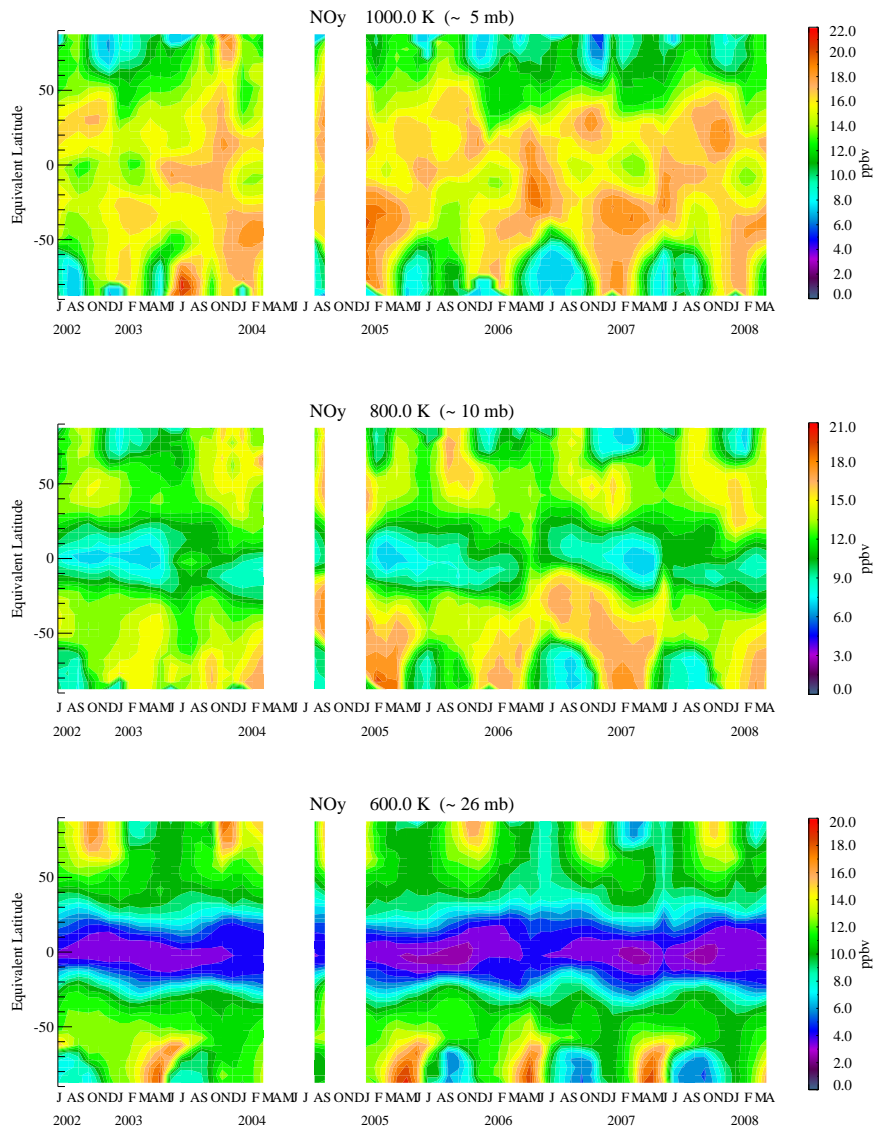


Figure 5.7: Time series of NO_y (nighttime NO_2 , HNO_3 , N_2O_5 , ClONO_2) at 600 K, 800 K and 1000 K. An approximate pressure level for each potential temperature surface is indicated.

surface represents the transition regions between the long and short-lived regimes. A systematic bias between the FR and RR data is not strongly evident in total NO_y , except in the high latitude northern hemisphere summer, where VMR on the 600 K surface is several ppbv lower than using the full resolution data, originating from the low bias in the reduced resolution NO_2 retrievals.

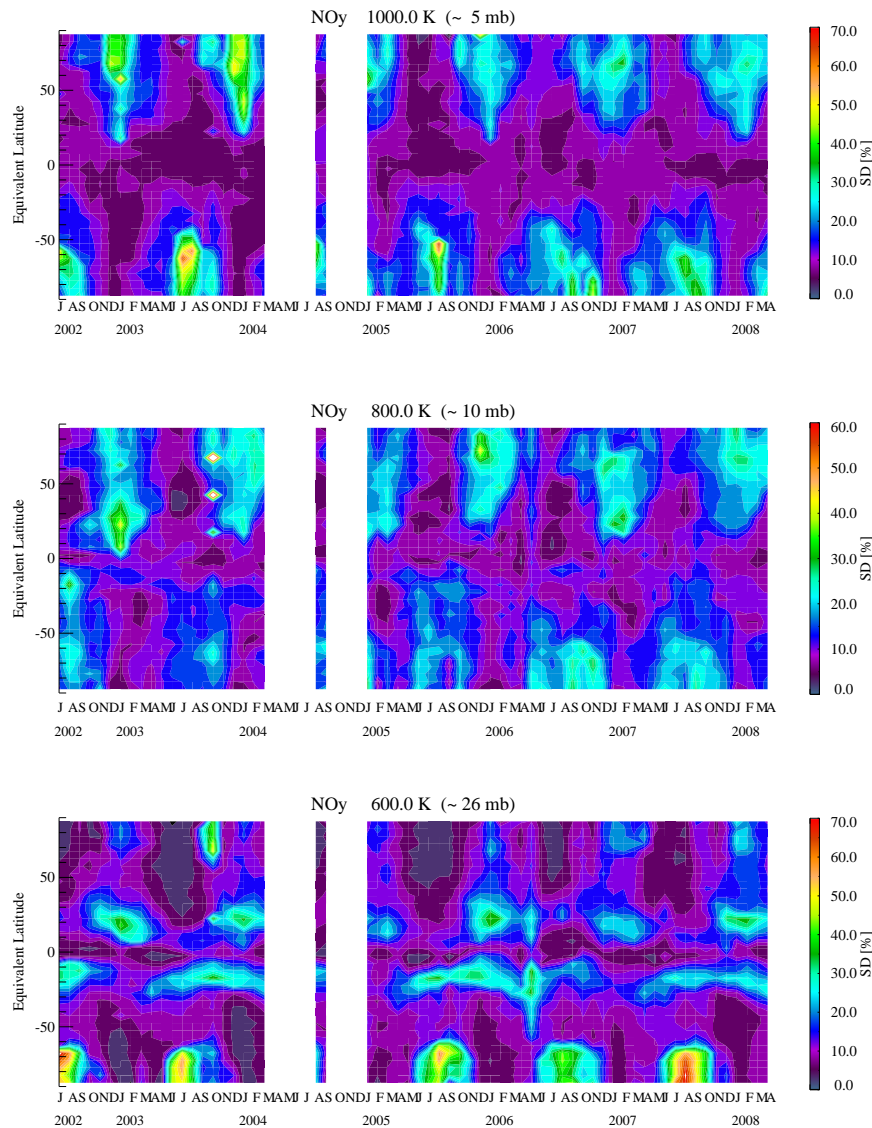


Figure 5.8: Standard deviation in percentage of time series of NO_y (nighttime NO_2 , HNO_3 , N_2O_5 , ClONO_2) at 600 K, 800 K and 1000 K. An approximate pressure level for each potential temperature surface is indicated.

5.3.2 Correlations between N_2O and NO_y

There are well known correlations between N_2O and NO_y in the stratosphere. Therefore, as a check for overall consistency of the datasets, the observed correlation between N_2O and NO_y for data acquired over the course of the mission may be compared with the expected values. Figure 5.9 shows the correlations between N_2O and NO_y for MIPAS data on

the 600 K potential temperature surface for July 2002–2008 (excluding 2004 where no data is available) in the SH, and for January of those years (including 2004) in the NH. Following Nash, E.R. and Newman, P. A. and Rosenfield, J., E and Schoeberl, M. R. (1996), data inside the polar vortex is separated from data outside the polar vortex by looking for the maximum gradient of Ertel’s potential vorticity in conjunction with the maximum zonal wind speed with respect to equivalent latitude, computed using operational ECMWF data (T159 Spectral Analysis on model levels, see BADC ECMWF Operational Analysis data, [Internet]).

Since stratospheric NO_y is produced by oxidation of N_2O injected from the troposphere in the tropics (Eq 5.2), younger air in the tropical stratosphere is high in N_2O and low in NO_y . As air moves towards the pole in the Brewer-Dobson circulation, and the residence time of air in the stratosphere increases, N_2O is gradually oxidised and air becomes richer in NO_y . Since the lifetimes of these species are long, of the order of decades, compared to the vertical and quasi-horizontal transport times, which are of the order of years and months respectively, there is a compact, almost linear (anti-) correlation between N_2O and NO_y , and the species are said to be in gradient equilibrium (Plumb and Ko, 1992; Keim et al., 1997). The value of the slope therefore represents the effective conversion efficiency of N_2O to NO_y and is largely independent of dynamical mixing effects.

However, the linear correlation breaks down inside the polar vortex. Here, air with mixing ratios of N_2O less than around 100 ppbv is transported down from altitudes where NO_y is short-lived, due to significant loss of NO_y via $\text{NO} + \text{N}$ (Eq 5.4). Under these conditions, the correlation is still compact but departs from linearity, as the gradient equilibrium condition breaks down (Lowenstein et al., 1993). At lower altitudes,

denitrification due to PSC formation and particle sedimentation in the lower-stratosphere is seen as a sudden departure from the correlation line for mixing ratios of N_2O less than around 140 ppbv, a value consistently observed at about the location where temperatures fall below the nitric acid tri-hydrate (NAT) condensation temperature (Lowenstein et al., 1993).

We calculate correlations between N_2O and NO_y for MIPAS data for the NH and SH winters (January in the NH and July in the SH, when the polar vortex is well established) spanning the FR and RR missions. Results are compared against correlations from *in situ* data obtained during a set of high altitude aircraft campaigns. Lowenstein et al. (1993) combined *in situ* aircraft measurements during Airborne Arctic Stratospheric Expedition (AASE) in 1989 with measurements from the follow-up mission, AASE, II in September 1991–March 1992. Trace gas concentrations were determined using infra-red absorption of tunable diode laser emission. Keim et al. (1997) obtained *in situ* aircraft measurements during the Airborne Southern Hemisphere Ozone Expedition/Measurements for Assessing the Effects of Stratospheric Aircraft (ASHOE/MAESA) in March–October 1994. They used a tunable laser absorption spectrometer to measure N_2O , and measured NO_y by catalytic reduction into NO followed by detection of NO and O_3 by chemi-luminescence. The extra-vortex (linear) correlations obtained are listed in table 5.1. In the first set of measurements by Lowenstein et al. (1993), an empirical correlation for the NH, valid for N_2O mixing ratios > 50 ppbv (below ~ 10 mb) was determined. Keim et al. (1997) later determined empirical correlations for the SH, also valid for N_2O mixing ratios > 50 ppbv. The correlation in the SH mid-latitudes showed seasonal variability of up to 28 %, whilst in the NH, observed seasonal variability was up to just 7%. This was attributed

to denitrification in the polar vortex, which occurs to a greater degree and over a wider area in the SH, and the subsequent mixing with air at lower latitudes. Values were assumed to return to previous values in the intervening months, completing the annual cycle (Keim et al., 1997). Due to this seasonal variability, aircraft measurements are used that are close in the seasonal cycle to the MIPAS observations.

The correlations calculated from MIPAS data for extra-vortex air are listed in table 5.1. In the NH, where the identification of air inside the vortex is less reliable, the extra-vortex correlation is calculated for data below 40°N equivalent latitude. At 600 K these equivalent latitudes are almost always found to be outside the vortex. In the SH extra-vortex air is identified as beginning at the edge of the outer surf-zone, which is determined by considering the maximum convex horizontal gradient in Ertel's potential vorticity against equivalent latitude. The 1σ uncertainty on the fitted parameters is indicated.

The range of correlation slopes implies an effective conversion efficiency for N_2O to NO_y of between around 6–7 %. The MIPAS data is generally self-consistent within the estimates of uncertainty, and there is no significant change between FR (2002, 2003, 2004) and RR (2005–2008) data. There is also good agreement between MIPAS and the aircraft measurements by Keim et al. (1997), although the correlation slope calculated for MIPAS measurements is consistently lower than the aircraft measurements in all years. The calculated correlations agree with the aircraft measurements within the given estimates of uncertainty.

Changes to the correlation curve associated with downwards transport are most apparent in the SH, where the vortex is more intense and stable. The location of the polar vortex, and separation of vortex from extra-vortex air is more successful in the SH, where there are strong gra-

dients in Ertel's potential vorticity and a strong zonal jet. In the NH, the vortex is less stable, breaking down sporadically throughout winter, triggered by sudden stratospheric warming events (Andrews et al., 1987). In particular, the sudden drop in NO_y for N_2O values below around 100 ppmv, perhaps associated with de-nitrification due to PSC formation and particle sedimentation, is especially apparent in 2005 and 2007. This sharp decrease is not seen in the NH data, where temperatures for NAT formation are reached less frequently and over a smaller area, although there is a hint of a break-down in linearity, due to downwards transport of air from altitudes where NO_y is not long-lived, where the curve flattens out for concentrations of N_2O less than around 100 ppbv.

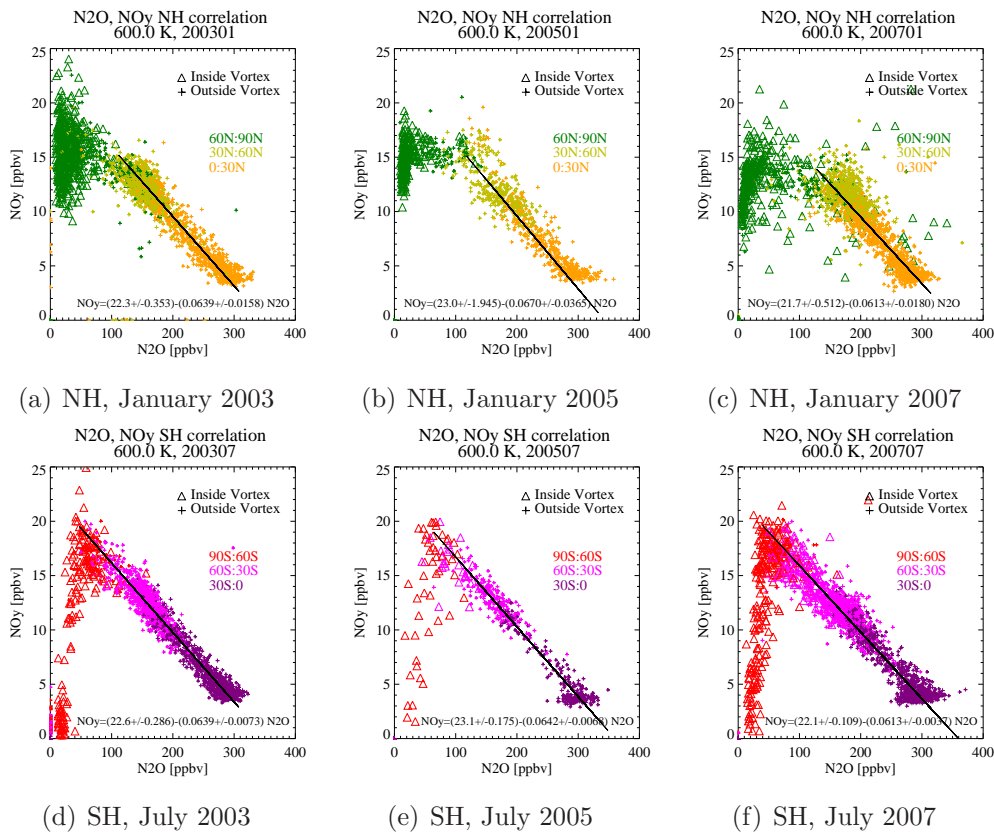


Figure 5.9: Correlations between N_2O and NO_y at 600 K for Southern and Northern Hemisphere winters in 2003, 2005 and 2007. Also shown is the empirical correlation calculated for extra-vortex data.

Year	Month		N_2O , NO_y correlation
		NH	$\text{NO}_y = 20.7 - 0.0644 \times \text{N}_2\text{O}$ (Uncertainty N/A) September 1991- March 1992 (Lowenstein et al., 1993).
		NH	$\text{NO}_y = (22.83 \pm 0.05) - (0.073 \pm 0.0002) \times \text{N}_2\text{O}$. January 1996 mid-latitudes (Keim et al., 1997).
		SH	$\text{NO}_y = (21.81 \pm 0.14) - (0.070 \pm 0.001) \times \text{N}_2\text{O}$. August 1994 mid-latitudes (Keim et al., 1997).
2003	January	NH	$\text{NO}_y = (22.3 \pm 0.4) - (0.064 \pm 0.158) \times \text{N}_2\text{O}$
	July	SH	$\text{NO}_y = (22.6 \pm 0.3) - (0.064 \pm 0.007) \times \text{N}_2\text{O}$
2005	January	NH	$\text{NO}_y = (23.0 \pm 1.9) - (0.067 \pm 0.037) \times \text{N}_2\text{O}$
	July	SH	$\text{NO}_y = (23.1 \pm 0.2) - (0.064 \pm 0.007) \times \text{N}_2\text{O}$
2007	January	NH	$\text{NO}_y = (21.7 \pm 0.5) - (0.061 \pm 0.018) \times \text{N}_2\text{O}$
	July	SH	$\text{NO}_y = (21.1 \pm 0.1) - (0.061 \pm 0.004) \times \text{N}_2\text{O}$

Table 5.1: Empirical anti-correlation between N_2O and NO_y for Northern and Southern Hemisphere for aircraft data (see references) and MIPAS FR and RR data. 1σ error in fitted parameters indicated.

Correlations with altitude

Correlations with altitude were examined qualitatively. Figure 5.10 shows the N_2O , NO_y correlations obtained with altitude in five equivalent latitude bands: 90:60 N/S, 60:30 N/S and 30S:30N using RR data for the first time from July 2007. In the winter hemisphere polar band (90S:60S), air may be de-nitrified at lower altitudes and the apparent gradient is reduced. Otherwise, trends are qualitatively as expected. The expected linear trends at high and low mixing N_2O ratios are evident, as well as the more scattered non-linear region around the peak of NO_y . The expected latitudinal variation is also observed with the highest values of peak NO_y observed in the tropics, and the lowest values in the mid-high latitudes in the summer hemisphere (Plumb and Ko, 1992).

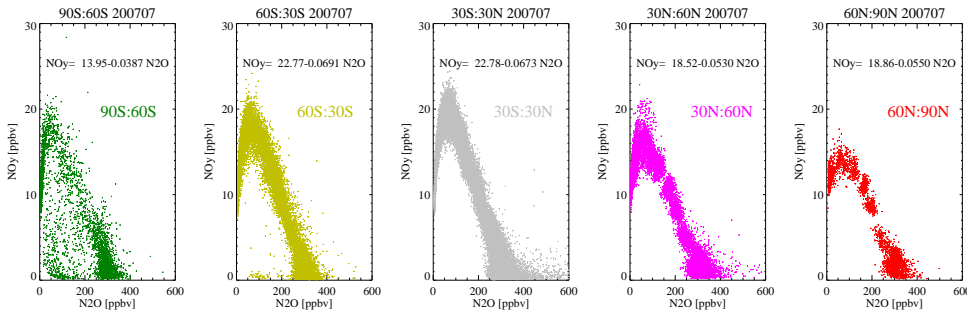


Figure 5.10: Vertical correlation between N_2O and NO_y in equivalent latitude bands 90:60 N/S, 60:30 N/S and 30S:30N. Data included from $\theta=350\text{--}5000$ K which spans the troposphere to lower-thermosphere. Linear fit calculated for stratospheric altitudes where N_2O values are between 150 and 40 ppbv.

5.4 Conclusions and future work

The MIPAS FR data-set was combined for the first time with RR data to outline a climatology of NO_y spanning 2002–2008, with the gap in data coverage during 2004 now representing just a small fraction of the total time series. Many of the expected features in N_2O , NO_y and ozone were evident in both the FR and RR data, which serves to illustrate the potential of MIPAS to provide a comprehensive, long-term data-set for NO_y , the source gas N_2O , as well as ozone. Correlations between the source gas N_2O and NO_y for extra-vortex data were investigated to test for consistency between FR and RR data-sets. In the mid-stratosphere, there were no significant differences between results using FR and RR data, within the estimates of uncertainty, and results were also broadly in agreement with correlations calculated previously for the NH and SH from high altitude aircraft campaigns (especially Keim et al., 1997). Data identified as being inside the polar vortex showed signs of downwards transport, as well as denitrification attributed to sedimentation on the surface of PSC's. The expected qualitative correlations of N_2O against NO_y with altitude were also observed, with linear correlations at low and high mixing ratios of N_2O , high values of the NO_y peak in the tropics

and lower values in the high latitude summer hemisphere.

There is large scope for future investigations using this combined data-set. It is suggested that an interesting candidate for quantitative analysis could be the total mass of odd nitrogen deposited in the stratosphere during the break-down of the polar vortex. It has been suggested that the net deposition of NO_x in the Antarctic winter can account for up to 9% of the N₂O oxidation source in the Southern Hemisphere (Funke et al., 2005). The long time series now afforded by MIPAS may now allow this quantity to be determined conclusively.

Chapter 6

Conclusions

Chapter 2 investigated the retrieval impact of the reduction in spectral resolution and increased vertical sampling introduced after a failure in the interferometer slide mechanism. The thesis then went on to address the main hypothesis that the range of species retrieved from MIPAS-ENVISAT could be extended within an Oxford-specific state of the art retrieval system to include important species whose retrieval was challenging. A feasibility study was performed for CO, which is an important tracer used throughout the atmosphere whose retrieval is complicated by non-LTE effects. To advance the suite of atmospheric chemistry measurements of NO_y , improvements were made to the retrieval of the diurnally varying species N_2O_5 . Di-nitrogen pentoxide is an important component of NO_y , linking the highly reactive nitrogen species NO and NO_2 to the more permanent reservoir HNO_3 . However, it is difficult to distinguish from the spectrally smooth background continuum due to its weak signal and flat spectral shape. The improved retrieval was validated using a novel method comparing MIPAS observations with an experimental rate constant. Then, in the final chapter, a climatology of NO_y (nighttime NO_2 , $2\times\text{N}_2\text{O}_5$, HNO_3 and ClONO_2), as well as the source gas N_2O and

ozone, was outlined using both the full and reduced resolution datasets for the first time.

Investigations into the effect of the new measurement modes were investigated for a worst case (CO) and best case (N_2O_5) molecule. Retrievals of CO in the stratosphere and above were expected to be severely affected by the reduction in spectral resolution. However, it was found that due to the non-negligible line width of CO, the impact of the RR modes on the retrieval for this molecule in the stratosphere was less severe than anticipated. The retrieval of N_2O_5 was not affected by the change in spectral resolution. Oversampling in the vertical domain in the new measurement modes was found to be the most significant factor in degradation of retrieval precision. Various vertical measurement and retrieval grids were tested. Retrieval points with a vertical spacing of 1.5 km used in the RR27 mode did not lead to a significant improvement in vertical resolution in the UTLS. However, there were significant increases in retrieval random error, due mainly to the shorter path length perturbed along the line-of-sight on the more closely spaced grid. By retrieving from a coarser grid (FR17) using the new RR27 mode data this degradation in retrieval sensitivity could be avoided.

Differences in systematic errors between the FR and RR retrievals are a more significant concern, as random errors can be reduced by averaging spectra leaving just the systematic component. Propagation of systematic errors through the FR17 and RR27 retrievals were calculated using operational microwindows for CO and N_2O_5 . Errors due to uncertainties in the horizontal temperature gradient were significantly larger in the RR27 mode than in the FR17 mode for CO. The contribution from uncertainties in the background continuum also made a more significant contribution in the RR27 mode. There were no significant difference in

systematic errors for the N_2O_5 retrieval. In both cases, the most significant contribution arises from uncertainties in the spectral database.

The retrieval of CO was investigated in chapter 3. Firstly, the quality of the retrieval that can be obtained ignoring non-LTE was investigated. In simulations, it was found that the systematic errors incurred were largest during the day, and were up to 20 times more significant than random error due to measurement noise at the top of the profile. However, it was found that non-LTE effects could be ignored in the UTLS, and at all altitudes at night without introducing significant systematic errors, for typical conditions of cloudiness, surface and tropospheric temperature. Polar nighttime data could also be used ignoring non-LTE. The systematic error was of the same order of magnitude as random error in this case and was in the negative sense. In comparisons of the MIPAS LTE retrieval of CO against EOS MLS data, which is unaffected by non-LTE, agreement was generally good, apart from some known problems in the MLS data, and a general low bias of MLS data with respect to MIPAS above 1 mb, where both data-sets are strongly influenced by different prior constraints.

The feasibility of a joint retrieval of CO and vibrational temperature to account for non-LTE effects was investigated in chapter 3. This type of algorithm is simpler to implement and faster than existing non-LTE retrieval schemes, which incorporate a non-LTE populations model into the inversion process (IMK/IAA). A retrieval code was written for the joint retrieval of CO and T_v using sequential optimal estimation with a Gauss-Newton Levenberg-Marquardt iteration scheme. It was found that CO random errors for the joint retrieval under both day and nighttime conditions were less than 70 % of the profile value at all altitudes, and better than 20 % in the UTLS. It was found that the retrieval of CO in the

stratosphere is strongly affected by the T_v profile in the mesosphere, and that some account must be taken of the upper-atmospheric T_v structure for a reasonable CO retrieval. In simulations, extra retrieval levels were introduced into the T_v state vector at 90 and 120 km. The effect of prior knowledge of T_v on the retrieval of CO was then investigated. It was found that using T_k as the prior estimate of T_v resulted in poor retrieval sensitivity, and there was a -20 % in CO at the top tangent altitude. The requirement on prior knowledge of T_v was found to be more strict for overestimates than for underestimates. For overestimates, the T_v structure needs to be known to within 5–7 K in the mesosphere for an accurate retrieval of CO in the stratosphere (bias to within 25 % for overestimates). Random errors for CO were improved at high altitudes by including a column retrieval into the state vector from 68 km to the top-of-the-atmosphere. However, the bias in the CO retrieval increased. In general, the bias in CO was very small (< 10 % below 30 km).

In chapter 3, a preliminary climatology of T_v was produced for use as prior data in a joint CO, T_v retrieval. The climatology was created using the GRANADA non-LTE populations model, considering variations in T_k , CO VMR and solar zenith angle. Two versions of the climatology were produced. The first version considered only radiative non-LTE effects, and the second also included $N_2(1)$ V-V transfer processes, which involve solving the non-LTE radiative transfer equation for a coupled system involving several other species whose concentrations were fixed. Vibrational temperature was then calculated on a profile-by-profile basis using a parameterisation that adjusts the tabulated non-LTE population ratios according to the observed T_k . An error analysis was performed for the parameterisation, which does not adjust radiative transfer between layers. Maximum errors of up to 4 K were expected during the day, and

10 K at night for the $N_2(1)$ V-V version of the climatology.

The joint retrieval was then tested on real data using MORSE. Zonal mean CO was computed in broad latitude bands for the 30th November 2003. There were significant biases in all cases examined. The bias was least significant using the most accurate version of the T_v climatology which considers $N_2(1)$ V-V processes as well as radiative excitation, applying a column retrieval of CO in the mesosphere, and with the upper level of the T_v state vector shifted to 80 km. Further development of the T_v climatology is an involved problem, and it is probable that the required knowledge of T_v may only be possible using online calculations of the non-LTE populations within the inversion process (IMK/IAA). The joint retrieval of CO and T_v is therefore not recommended for development into an operational scheme.

The non-LTE effects in the CO isotopologues ($^{12}C^{16}O$, $^{13}C^{16}O$, $^{12}C^{18}O$) were then investigated in chapter 3. Non-LTE enhancements were observed during the day, and conversely lower-than-LTE values were seen at night. Vibrational temperature profiles were derived. There were large associated uncertainties, and difficulties removing the contaminant signal. However, there were some hints of the expected trend in T_v between isotopologues, with the less abundant species having a higher vibrational temperature due to the relative transparency of the atmosphere to upwelling radiation. Errors in the analysis overwhelmed any trends, however, and results were inconclusive.

Hotband emission of the principal isotopologue was observed for the CO(2-1) transition.

It is recommended that the isotopologues and hotband contributions are masked during a retrieval of the principal isotope of CO.

In chapter 4, the treatment of the continuum was altered to improve

the retrieval of N_2O_5 . By assuming that the continuum is spectrally smooth a single extinction can be retrieved for all microwindows increasing the information available about N_2O_5 . The improved retrieval was then validated by comparing two estimates of a rate constant associated with its nighttime formation, one which depends on the observed nighttime N_2O_5 and NO_2 mixing ratios, sunset N_2O_5 concentrations, and ozone amount (denoted k_{VMR}), and another which can be calculated from the observed temperature, using experimental parameters for the stratosphere recommended by JPL (assumed to be true rate constant, denoted k). Two approaches were presented. The first assumes that sunset N_2O_5 is negligible. The second calculates the residual at sunset using a photochemical model (TUV) to calculate the photolysis rates, having supplied the observed ozone number densities. Agreement between k_{VMR} and k was very good for both methods. As expected, better agreement was obtained taking into account non-negligible sunset N_2O_5 for high latitude wintertime measurements. The analysis was performed at 3 mid-stratospheric altitudes (33, 36 and 39 km). The downwards trend in k_{VMR} towards large times since sunset at 33 km, see figure 4.8(b) was attributed to a problem with photolysis rates being too low at this altitude, rather than heterogeneous loss. A slight downwards trend was observed at 39 km, see figure 4.9(b). The implied bias in $[\text{N}_2\text{O}_5]$ was (0.1 ± 0.3) ppbv at low-latitudes

In chapter 4, it was shown that using a higher prior estimate can lead to a positive bias in retrieved values for small mixing ratios when performing a retrieval of $\ln(\text{VMR})$. In simulations, it was shown that this bias could be removed by performing the retrieval in linear-space.

In chapter 5, a long-term, global climatology of NO_y was constructed using both the full and reduced resolution data for the first time. It

was found that total error (random + systematic) of better than 10 % could be obtained for total NO_y for both FR17 and RR27 data in the mid-stratosphere. Monthly mean time series displayed many of the expected features at the 600 K potential temperature level (~ 30 mb), illustrating the potential of MIPAS to provide a long-term, comprehensive climatology of NO_y . Total NO_y was examined at 3 potential temperature surfaces in the stratosphere (600, 800 and 1000 K). The transition from a long-lived regime for NO_y at 600 K to a short-lived regime in the upper-stratosphere at 1000 K was clearly visible. A systematic bias was observed in NO_2 between full and reduced resolution data, particularly in the high latitude summer of the Northern Hemisphere, where widespread differences of several ppbv were observed. Analysis of systematic errors affecting NO_2 using operational FR17 and RR27 microwindows revealed that discrepancies may be due to a much larger systematic error due to uncertainties in the horizontal temperature gradient in the RR27 mode. To test for overall consistency of the MIPAS data-set, NH and SH correlations between N_2O and NO_y were calculated on the 600 K potential temperature surface for FR (2003) and RR (2005 and 2007) data. The MIPAS data was found to be self-consistent, and the agreement between calculated correlations for extra-vortex air was very good. There was also very good agreement between the correlations calculated from MIPAS data and previous high altitude aircraft measurements by Keim et al. (1997). The MIPAS data implied a conversion efficiency for the oxidation of N_2O to form NO_y of between 6–7 %. There was also evidence of subsidence of air from higher altitudes, where NO_y is short-lived, inside the polar vortex in both hemispheres. In the Southern Hemisphere, there was evidence of denitrication due to sedimentation of HNO_3 on the surface of PSC's inside the polar vortex. The correlation between

N_2O and NO_y with altitude was examined qualitatively in broad latitude bands. Trends were as expected with highest peak values of NO_y in the equatorial regions, and lowest peak values in the high-latitude summer regions.

6.1 Future Work

The joint retrieval of CO and T_v is not recommended for development into an operational scheme. However, it may be of interest for use as a faster, but less accurate alternative to the full non-LTE retrieval approach (IMK/IAA). Improvements that would need to be considered, mainly relating to the T_v climatology used to create the *a priori* estimate, are:

- Improved climatology of the collisional partners used in the V-V transfer calculations: CO_2 , N_2 , O_2 , and in particular $\text{O}(^3\text{P})$, which depends on solar zenith angle.
- Perform a full error analysis of the T_v climatology, examining representation of climatological variables (T_k , CO VMR, SZA, collisional partners), interpolation errors, errors and omissions in non-LTE modelling, and further investigation into the errors introduced by the parameterisation.
- Decide how best to tabulate the population ratios. Rather than tabulating population ratios based on different climatological T_k profiles, for example, it may be worth investigating tabulating according to perturbations applied at key points along the profile. For example, an adjustment to the T_k profile around the stratopause has a much bigger effect on the upwelling radiation (neglected in the parameterisation) than an equivalent perturbation in the tro-

posphere. A scheme that allows for denser tabulation in important regions may be advantageous in terms parameterisation errors.

The climatology of T_v could be tested as an improved first guess for use in the IMK/IAA CO retrieval (*S. Migliorini per comm*).

The *a priori* estimate of CO should also be examined. This is especially important in the polar regions, where downwelling and mixing around the polar vortex results in highly variable CO concentrations, which probably exceed the current prior estimate of uncertainty typically applied of 100 % of the profile value.

The optimum spacing of the retrieval grid for both CO and T_v should be investigated. It may be necessary to alter the retrieval grid used in the kinetic temperature retrieval, so that the non-LTE excitation ($T_v - T_k$) can be determined more reliably in the mesosphere. Currently, a climatological value of T_k is assumed above the top tangent altitude, and this may limit the effectiveness of the joint retrieval at lower altitudes.

If the joint retrieval of CO, T_v can be improved significantly, then a comparison should be performed against results from the IMK/IAA processor.

Other small suggestions for further work in chapter 3 on non-LTE effects on the CO isotopologues may be found for the interested reader therein.

In chapter 4, the linear-space retrieval of N_2O_5 should be tested on real data. The validation exercise, comparing independently derived rate constants, should then be repeated.

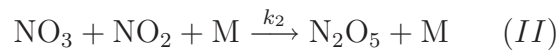
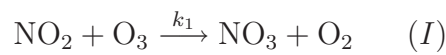
The new MIPAS NO_y , N_2O and ozone data-set presented in 5 appears very promising, although RR27 microwindows, in particular for NO_2 , require further optimisation. The dataset should also be examined for the seasonal correlations between NO_2 and HNO_3 as well as NO_2 and

O₃. It is suggested that an interesting candidate for qualitative analysis would be to determine the total amount of odd nitrogen deposited in the mid-latitude stratosphere after the break-up of the polar vortex in each hemisphere.

Appendix A

Derivation of N₂O₅-dependent rate constant

The following expanded derivation is taken from the paper by Toumi, R. and Pyle, J. A. and Webster, C. R. (1991). The formation of nighttime N₂O₅ is described by;



The continuity equations for [NO₂] and [N₂O₅] may be written;

$$\frac{d[\text{NO}_2]}{dt} = -k_1[\text{NO}_2][\text{O}_3] - k_2[\text{NO}_3][\text{NO}_2][\text{M}] \quad (\text{A.1})$$

$$\frac{d[\text{N}_2\text{O}_5]}{dt} = k_2[\text{NO}_2][\text{NO}_3][\text{M}] \quad (\text{A.2})$$

Concentrations of NO₃ are approximately in equilibrium and are sustained throughout the night (Naudet et al., 1981). Therefore, NO₃ in

reaction (I) is considered to be in a steady state so that the contribution from $\frac{d[NO_3]}{dt}$ is effectively zero;

$$\frac{d[NO_3]}{dt} = -k_2[NO_2][NO_3][M] + k_1[NO_2][O_3] = 0 \quad (A.3)$$

Eliminating $[NO_3]$ between equations A.1 and A.3, and integrating, we derive an expression for the time evolution of NO_2 ;

$$[NO_2] = [NO_2]_{set} \exp(-2k_1[O_3]t) \quad (A.4)$$

Eliminating $[NO_3]$ between equations A.2 and A.3, the continuity equation for N_2O_5 becomes;

$$\frac{[N_2O_5]}{dt} = k_1[O_3][NO_2]_{set} \exp(-2k_1[O_3]t) \quad (A.5)$$

Eliminating $[NO_2]_{set}$ using equation A.4 and integrating, we obtain;

$$[N_2O_5] = \frac{[NO_2]}{2} (\exp(2k_1[O_3]t) - 1) + [N_2O_5]_{set} \quad (A.6)$$

where t is time since sunset, $[NO_2]_{set}$ is the concentration at sunset, $[N_2O_5]_0$ is the concentrations at sunset and $[O_3]$ is the observed concentration and is assumed not to vary.

An expression for the rate constant k_1 (referred to in main text as k_{VMR}), corresponding to the rate limiting step (I) is given by;

$$k_1 = \frac{1}{2[O_3]t} \ln \left(\frac{2\Delta[N_2O_5]}{[NO_2]} + 1 \right) \quad ; \Delta[N_2O_5] = [N_2O_5] - [N_2O_5]_{set} \quad (A.7)$$

Appendix B

NO_y random and sytematic errors

Random and systematic errors for NO_y (NO₂, HNO₃, N₂O₅ and ClONO₂) as well as the source gas N₂O have been calculated for FR17 and RR27 operational microwindows. The spectral and altitude ranges of the top three microwindows, with the most imformation content selected for use in the FR17 and RR27 measurement modes are listed in tables B.1 and B.2.

Species	Label	Wavenumber range [cm^{-1}]	Altitude range [km]
N ₂ O	N2O0001	1272.0500–1275.0500	12–60
	N2O0004	1256.6750–1257.9750	9–30
	N2O0005	1262.3500–1263.1250	18–33
NO ₂	NO20001	1607.2750–1610.2750	15–68
	NO20002	1606.7750–1607.2000	15–30
	NO20003	1613.7250–1616.6000	15–68
HNO ₃	HNO30001	876.3750–879.3750	6–68
	HNO30003	1324.1750–1327.1750	33–68
	HNO30004	774.9000–775.0500	6–15
N ₂ O ₅	N2O50103	1238.8250–1241.7750	6–36
	N2O50104	1245.6750–1248.6750	6–39
	N2O50122	1243.4500–1246.4500	15–68
ClONO ₂	CLNO0101	778.5250–781.5250	18–52
	CLNO0102	1290.6250–1293.6250	6–68
	CLNO0103	808.4250–811.4250	6–36

Table B.1: Top three FR17 microwindows, selected for nighttime conditions, to retrieve NO_y (NO_2 , HNO_3 , N_2O_5 and ClONO_2) and N_2O .

Species	Label	Wavenumber range [cm^{-1}]	Altitude range [km]
N ₂ O	N2O0201	1271.6875–1274.6875	12–60
	N2O0202	1232.3750–1235.3750	6–27
	N2O0203	1276.3125–1279.3125	15–60
NO ₂	NO20201	1598.8750–1601.8750	15–60
	NO20202	1603.9375–1606.9375	15–60
	NO20203	1612.2500–1615.2500	15–60
HNO ₃	HNO30201	867.3125–870.3125	6–68
	HNO30202	878.2500–881.2500	9–60
	HNO30203	884.4375–887.4375	6–68
N ₂ O ₅	N2O50301	1232.8750–1235.8750	15–58
	N2O50302	1229.8125–1232.8125	18–58
	N2O50303	1236.0625–1238.6875	18–54
ClONO ₂	CLNO0301	812.2500–815.2500	15–46
	CLNO0302	815.3125–818.3125	16–40
	CLNO0303	1724.0000–1727.0000	13–40

Table B.2: Top three RR27 microwindows, selected for nighttime conditions, to retrieve NO_y (NO_2 , HNO_3 , N_2O_5 and ClONO_2) and N_2O .

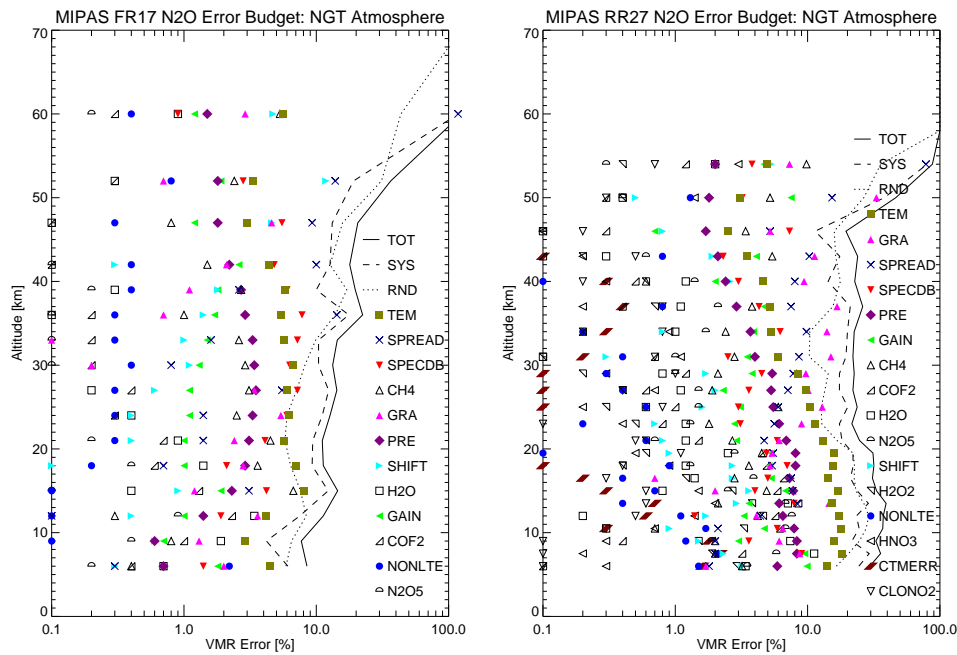


Figure B.1: Random and systematic errors calculated for N_2O using FR17 and RR27 operational microwindows.

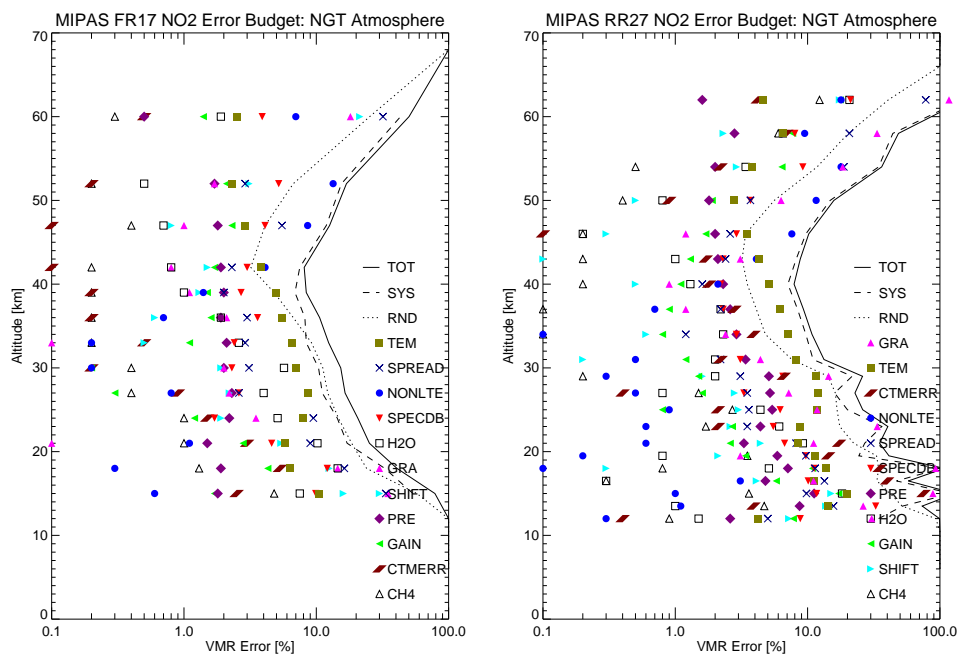


Figure B.2: Random and systematic errors calculated for NO_2 using FR17 and RR27 operational microwindows.

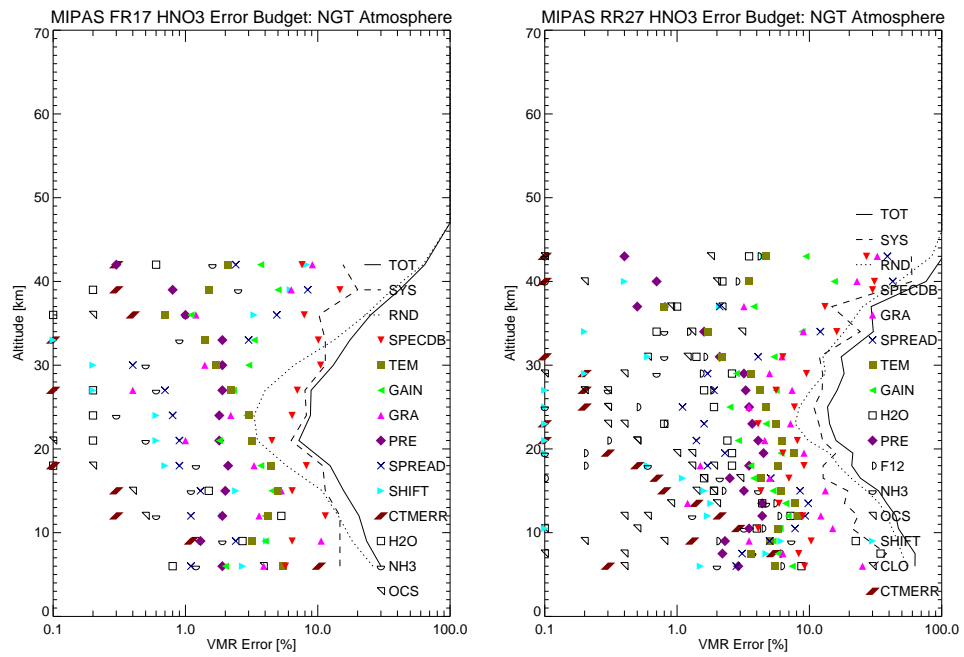


Figure B.3: Random and systematic errors calculated for HNO_3 using FR17 and RR27 operational microwindows.

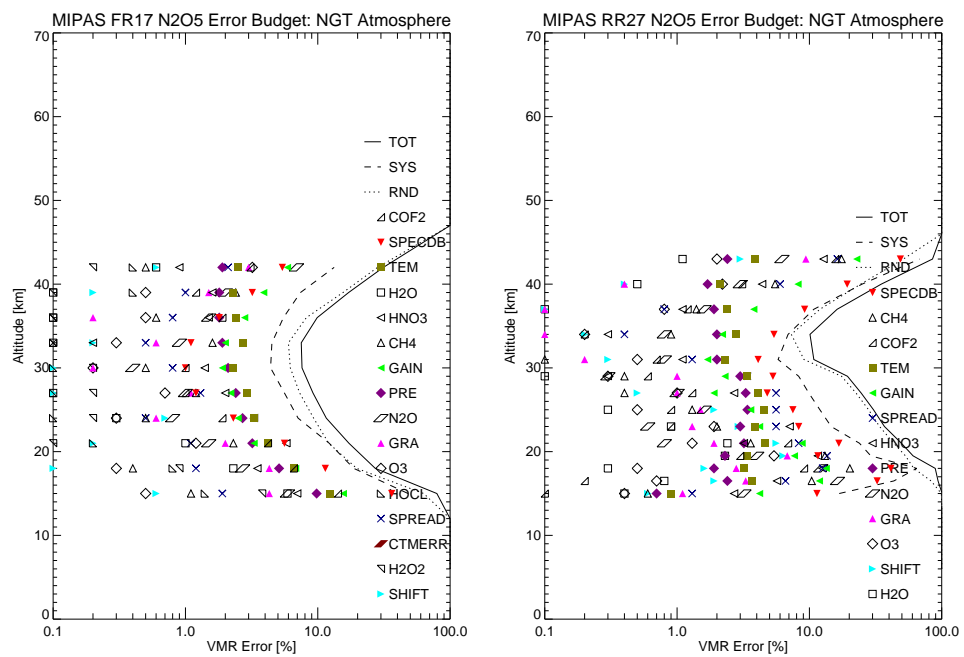


Figure B.4: Random and systematic errors calculated for N_2O_5 using FR17 and RR27 operational microwindows.

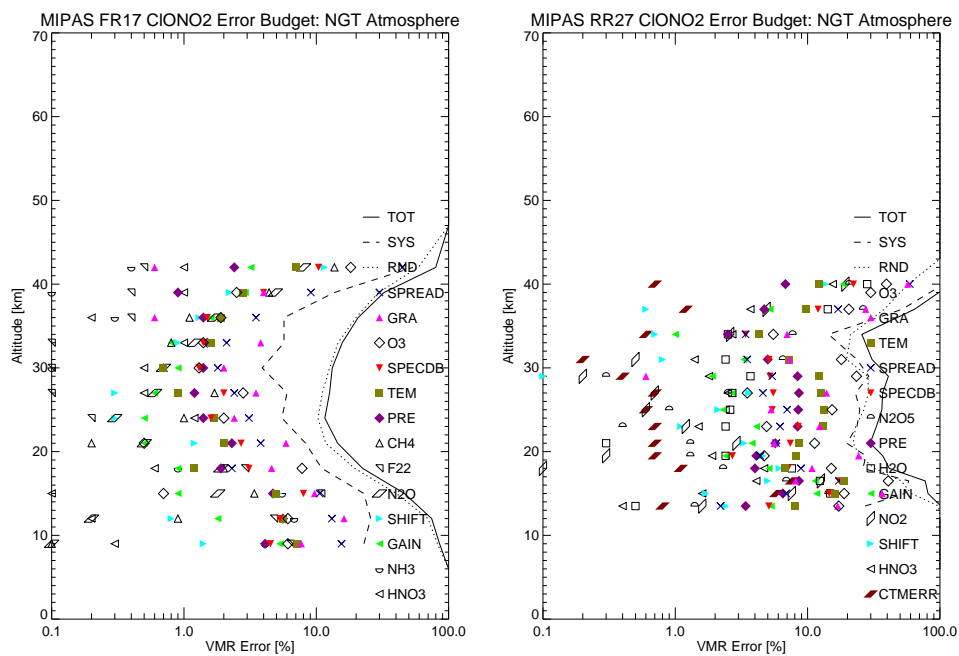


Figure B.5: Random and systematic errors calculated for ClONO₂ using FR17 and RR27 operational microwindows.

Appendix C

Coordinate transformations

C.1 Potential vorticity potential temperature coordinates

Rather than working in the usual spatial coordinates, it is often more useful to work in a system of coordinates consisting of potential temperature in the vertical, potential vorticity in the meridional direction and longitude (Stan and Randall, 2007). Since air parcels tend to conserve potential temperature and potential vorticity, as a result of transforming to this system, particles more generally follow the coordinate surfaces and much of the less interesting variation is removed. Potential temperature refers to the temperature a parcel of air would attain if it were to descend adiabatically to a reference pressure level, commonly 1000mb;

$$\theta = T \left(\frac{1000}{p} \right)^{(R/c_p)} \quad (\text{C.1})$$

where R is the gas constant and c_p is the specific heat capacity at constant pressure. Working in isentropic (potential temperature) coordinates eliminates adiabatic motions in the vertical. Potential vorticity

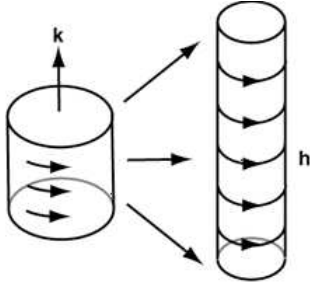


Figure C.1: Potential vorticity is a conserved quantity. As air converges, the column of air “spins-up” and relative vorticity increases.

coordinates perform a similar function, removing variation due to frictionless, adiabatic motions in the meridional direction. Ertel’s potential vorticity (EPV), which is the vertical component of absolute vorticity defined in isentropic coordinates, may be written;

$$\bar{\zeta} = f - \frac{(u \cos \phi)_\phi}{a \cos \phi} + \frac{v_\lambda}{a \cos \phi} \quad (\text{C.2})$$

$$\text{EPV} = \frac{\bar{\zeta}}{\sigma}, \quad \text{where } \sigma = -g^{-1} p_\theta \quad (\text{C.3})$$

where $f (=2|\Omega| \sin(\phi))$ is the coriolis parameter, u is the zonal component of wind, v is the meridional component of wind, ϕ is latitude and λ is longitude (Andrews et al., 1987). Figure C.1 illustrates the conservation of potential vorticity between potential temperature surfaces. Somewhat analogously to an ice-skater who draws their arms inwards and spins faster, as air converges, and the air column stretches, relative vorticity increases and the air column “spins-up”. EPV increases towards the north, is positive in the northern hemisphere and negative in the southern hemisphere, appearing as a series of meandering isolines surrounding the pole. When motion is frictionless and adiabatic, material may be thought of as being advected zonally along potential vorticity tubes with impermeable walls, which inflate in some regions and deflate in others

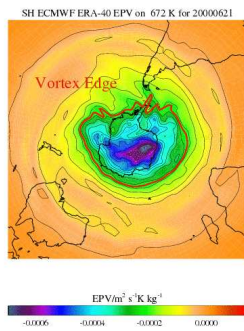
as air moves inside the tube (Stan and Randall, 2007). Diabatic and frictional processes mean, however, that in the high atmosphere, and in the boundary layer, EPV is not necessarily conserved.

C.2 Equivalent latitude

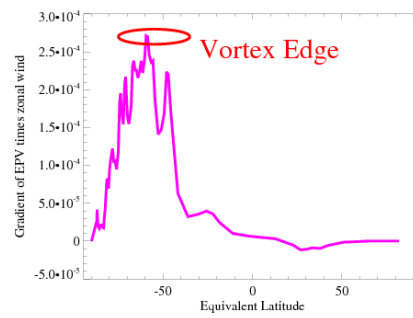
Equivalent latitude facilitates zonal averaging along potential vorticity tubes. It corresponds to the latitude circle bounding an area of the globe equal to the area enclosed by a given the isoline. This type of zonal averaging is particularly useful around the polar vortex where composition changes rapidly, with tongues of vortex air often extending to lower latitudes. Under these conditions, simple zonal averaging by latitude tends to smooth out the meridional variation. Averaging along potential vorticity tubes, on the other hand, captures the rapidly changing composition in this region.

C.3 Defining the vortex edge

Working in this coordinate system, the vortex edge may be determined by considering the maximum horizontal gradient of EPV in conjunction with the maximum zonal wind speed. At the true vortex edge, both distributions have strong peaks, (Nash, E.R. and Newman, P. A. and Rosenfield, J., E and Schoeberl, M. R., 1996). The edges of the surf-zone, where air inside the vortex mixes with air outside, is determined by considering the maximum concave and convex horizontal gradients of EPV.



(a) EPV fields in the SH from ERA-40 data on 6th June 2000 on 672 K.



(b) The pink line shows the gradient of EPV times the zonal wind on this date. There is a sharp maximum that defines the vortex edge.

Figure C.2: Determination of the vortex edge using EPV fields in the SH from ERA-40 data on 6th June 2000 on 672 K.

Bibliography

- Allen, D. C. and Simpson, C. J. S. M.: Vibrational energy exchange between CO and the isotopes of N₂ between 300 K and 80 K, *Chemical Physics*, 45, 203–211, 1980.
- Allen, D. R., Stanford, J. L., López-Valverde, M. A., Nakamura, N., Lary, D. J., Douglass, A. R., Cerniglia, M. C., Remedios, J. J., and Taylor, F. W.: Observations of Middle Atmosphere CO from the UARS ISAMS during the Early Northern Winter 1991/92, *Journal of the Atmospheric Sciences*, 56, 563–583, 1999.
- Allen, M. and Delitsky, M. L.: Stratospheric NO, NO₂ and N₂O₅: A comparison of Model Results With Spacelab 3 Atmospheric Trace Molecule Spectroscopy (ATMOS) Measurements, *Journal of Geophysical Research*, 95, 14 077–14 082, 1990.
- Andrews, D. G., Holton, J. R., and Leovy, C. B.: *Middle Atmosphere Dynamics*, vol. 40 of *International Geoscience Series*, Academic Press, 1987.
- BADC ECMWF Operational Analysis data, [Internet]: ECMWF Operational Analysis data, British Atmospheric Data Centre, URL <http://badc.nerc.ac.uk/data/ecmwf-op/>, 2006-.
- Barret, B., Turquety, S., Hurtmans, D., Clerbaux, C., Hadji-Lazaro, J., Bey, L., Auvray, M., and Coheur, P. F.: Global carbon monoxide vertical distributions from spaceborne high-resolution FTIR nadir measurements, *Atmospheric Chemistry Discussions*, 2001.

- Belotti, C., Carli, B., Ceccherini, S., and et al.: Retrieval of Tropospheric Carbon Monoxide from MIPAS Measurements, in: Atmospheric Science Conference, vol. 628 of *ESA Special Publication*, 2006.
- Brasseur, G. and Solomon, S.: *Aeronomy of the Middle Atmosphere*, D.Reidel Publishing Company, 1986.
- Brasseur, G., Orlando, J., and Tyndall, G.: *Atmospheric Chemistry and Global Change*, Oxford University Press, 1999a.
- Brasseur, G., Orlando, J., and Tyndall, G.: *Atmospheric Chemistry and Global Change*, Oxford University Press, 1999b.
- Brohede, S., McLinden, C. A., Urban, J., Haley, C. S., Jonsson, A. I., and Murtagh, D.: Odin stratospheric proxy NO_y measurements and climatology, *Atmospheric Chemistry and Physics Discussions*, 8, 5847–5899, 2008.
- Brühl, C., Steil, B., Stiller, G., Funke, B., and Jckel, P.: Nitrogen compounds and ozone in the stratosphere: comparison of MIPAS satellite data with the Chemistry Climate Model ECHAM5/MESSy1, *Atmospheric Chemistry and Physics Discussions*, 7, 9899–9924, 2007.
- Buchwitz, M., de Beek, R., Bramstedt, K., Noël, S., Bovensmann, H., and Burrows, J.: Global carbon monoxide as retrieved from SCIAMACHY by WFM-DOAS, *Atmospheric Chemistry and Physics Discussions*, 4, 2805–2837, 2004.
- Cantrell et al., C. A.: Infrared absorption cross sections for N_2O_5 , *Chemical Physics Letters*, 148, 358–363, 1988.
- Carlotti, M., Dinelli, B. M., Papandrea, E., and Ridolfi, M.: Assessment of the horizontal resolution of retrieval products derived from MIPAS observations, *Optics Express*, 15, 2005.

- Carlotti, M., Ceccherini, S., Raspollini, P., and Carli, B.: Modifications in MIPAS L2 processor for handling the new measurement scenario, Tech. rep., IFAC-CNR, 2006.
- Ceccherini, S., Cortesi, U., Verronen, P., and Kyrl, E.: Technical Note: Continuity of MIPAS-ENVISAT ozone data quality from full- to reduced-spectral-resolution operation mode, *Atmospheric Chemistry and Physics Discussions*, 8, 797–825, URL <http://www.atmos-chem-phys-discuss.net/8/797/2008/>, 2008.
- Chandrasekhar, S.: *Radiative Transfer*, Courier Dover Publications, 1960.
- Clerbaux, C., Hadji-Lazaro, J., Payan, S., Camy-Peyret, C., and Megie, G.: Retrieval of CO columns from IMG/ADEOS spectra, *Geoscience and Remote Sensing, IEEE Transactions on*, 37, 1657–1661, doi:10.1109/36.763283, May 1999.
- Clerbaux et al., C.: Carbon monoxide distribution from the ACE-FTS solar occultation measurements, *Geophysical Research Letters*, 32, 5814–5824, 2005.
- Connell, P. and Johnston, H.: The thermal dissociation of N₂O₅ in N₂, *Geophysical Research Letters*, 6, 1979.
- Crutzen, P.: The role of NO and NO₂ in the chemistry of the troposphere and stratosphere, *Annual Review of Earth and Planetary Science*, 7, 443–472, 1979.
- Crutzen, P. J.: The influence of nitrogen oxides on the atmospheric ozone content, *Quarterly Journal of the Royal Meteorological Society*, 96, 320–325, 1970.
- Danilin, M. Y., Rodriguez, J. M., Hu, W., Ko, M. K. W., Weisentein, D. K., Kumer, J. B., Mergenthaler, J. L., Russell III, J. M. and Koike, M., Yue,

- G. K., Jones, N. B., and Johnston, P. V.: Nitrogen species in the post-Pinatubo stratosphere: Model analysis utilizing UARS measurements, *Journal of Geophysical Research*, 104, 8247–8262, 1999.
- DeMore, W. B., Sander, S. P., Howard, C. J., Ravishnkara, A. R., Golden, D. M., Kolb, C. E., Hampson, R. F., Kurylo, M. J., and Molina, M. J.: Chemical kinetics and photochemical data for use in stratospheric modelling, Tech. rep., JPL, Evaluation number 12, 1997.
- Dodd, J. A., Winick, J. R., Blumberg, W. A. M., Lipson, S. J., Armstrong, P. S., and Lowell, J. R.: CIRRIS 1A observations of $^{13}\text{C}^{16}\text{O}$ and $^{12}\text{C}^{18}\text{O}$ fundamental band radiance in the upper atmosphere, *Geophysical Research Letters*, 23, 2683–2686, 1993.
- Dudhia, A.: Impact of Reduced Resolution on MIPAS, in: ASSFTS 12th Workshop, Quebec City, Canada, 2005.
- Dudhia, A.: MIPAS L2 errors [Internet], URL <http://www.atm.ox.ac.uk/group/mipas/err/>, 2007.
- Dudhia, A.: MIPAS Orbital Retrieval using Sequential Estimation (MORSE) [Internet], URL <http://www.atm.ox.ac.uk/MORSE/>, 2008a.
- Dudhia, A.: Reference Forward Model (RFM) [Internet], URL <http://www.atm.ox.ac.uk/RFM>, 2008b.
- Dudhia, A., Jay, V., and Rodgers, C. D.: Microwindow selection for high-spectral-resolution sounders, *Applied Optics*, 41, 3665–3673, 2002.
- Dudhia, A., ENVISAT Symposium, 2004: MIPAS Microwindows, ENVISAT and ERS Symposium, Saltzberg, 2004.
- Dupuy et al., E.: Strato-mesospheric measurements of carbon monoxide with the Odin Sub-Millimetre Radiometer: Retrieval and first results, *Geophysical Research Letters*, 31, 2004.

- Edwards, D. P.: GENLN2: A general line-by-line atmospheric transmittance and radiance model. Version 3.0: Description and users guide, Tech. rep., 1992.
- Edwards, D. P., López-Puertas, M., and Lopez-Valverde, M. A.: Non-local thermodynamic equilibrium studies of the 15 μm bands of CO₂ for atmospheric remote sensing, *Journal of Geophysical Research*, 98, 14 955–14 977, 1993.
- Edwards, D. P., Emmons, L. K., Gille, J. C., Chu, A., Attié, J. L., Giglio, L., Wood, S. W., Haywood, J., Deeter, M. N., Massie, S. T., Ziskin, D. C., and Drummond, J. R.: Satellite-observed pollution from Southern Hemisphere biomass burning, *Journal of Geophysical Research*, 111, 2006.
- Emmons, L., Deeter, M., Gille, J., Ziskin, D., Attié, J. L., and Warner, J.: Validation of MOPITT Retrievals of Carbon Monoxide, IEEE, 2002.
- Emmons, L. K., Deeter, M. N., Gille, J. C., Edwards, D. P., Attié, J.-L., Warner, J., Ziskin, D., Francis, G., Khattatov, B., Yudin, V., Lamarque, J.-F., Ho, S.-P., Mao, D., Chen, J. S., Drummond, J., Novelli, P., Sachse, G., Coffey, M. T., Hannigan, J. W., Gerbig, C., Kawakami, S., Kondo, Y., Takegawa, N., Schlager, H., Baehr, J., and Ziereis, H.: Validation of Measurements of Pollution in the Troposphere (MOPITT) CO retrievals with aircraft in situ profiles, *Journal of Geophysical Research*, 109, 2004.
- Endemann, M.: MIPAS Instrument Concept and Performance, Tech. rep., ESA-ESTEC, Noordwijk, european Symposium on Atmospheric Measurements from Space, 1999.
- Filipiak, M. J., Harwood, R. S., Jiang, J. H., Li, Q., Livesey, N. J., Manney, G. L., Read, W. G., Schwartz, M. J., Waters, J. W., and Wu, D. L.: Carbon monoxide measured by the EOS Microwave Limb Sounder on Aura: First results, *Geophysical Research Letters*, 32, 2005.

- Fischer, H. and Oelhaf, H.: Remote sensing of vertical profiles of atmospheric trace constituents with MIPAS limb-emission spectrometers, *Applied Optics*, 35, 2787, 1996.
- Flaud, J. M. and Carli, B.: MIPAS Dedicated Spectroscopic Database, Tech. rep., Institute for Applied Physics "Nello Carrara", URL <http://www.ifac.cnr.it/retrieval/database.html>, 2003.
- Friedl-Vallon, F., Maucher, G., Seefeldner, M., Trieschmann, O., Kleinert, A., Lengel, A., Keim, C., Oelhaf, H., and Fischer, H.: Design and Characterization of the Balloon-Borne Michelson Interferometer for Passive Atmospheric Sounding (MIPAS-B2), *Applied Optics*, 43, 3335–3355, 2004.
- Froidevaux, L., Livesey, N., Read, W., Jiang, Y., Jimenez, C., Filipiak, M., Schwartz, M., Santee, M., Pumphrey, H., Jiang, J., Wu, D., Manney, G., Drouin, B., Waters, J., Fetzer, E., Bernath, P., Boone, C., Walker, K., Jucks, K., Toon, G., Margitan, J., Sen, B., Webster, C., Christensen, L., Elkins, J., Atlas, E., Lueb, R., and Hendershot, R.: Early validation analyses of atmospheric profiles from EOS MLS on the aura Satellite, *Geoscience and Remote Sensing, IEEE Transactions on*, 44, 1106–1121, doi: 10.1109/TGRS.2006.864366, 2006.
- Funke, B., López-Puertas, M., Stiller, G., Clarmann, G. T. Höpfner, M., and Kuntz, M.: Non-LTE state distribution of nitric oxide and its impact on the retrieval of the stratospheric daytime NO profile from MIPAS limb sounding instruments, *Advances in Space Research*, 26, 2000.
- Funke, B., Martin-Torres, F. J., Lopez-Puertas, M., Höpfner, M., Hase, F., López-Valverde, M. A., and Garcia-Comas, M.: A Generic Non-lte Population Model For Mipas-envisat Data Analysis, EGS XXVII General Assembly, Nice, 21-26 April 2002, abstract#4915, 27, 2002.
- Funke, B., López-Puertas, M., Gil-López, S., von Clarmann, T., Stiller, G. P., Fischer, H., and Kellmann, S.: Downward transport of upper atmospheric

- NO_x into the polar stratosphere and lower mesosphere during the Antarctic 2003 and Arctic 2002/2003 winters, *Journal of Geophysical Research*, 110, doi:10.1029/2005JD006463, 2005.
- Funke, B., López-Puertas, M., Bermejo-Pantaleón, D., von Clarmann, T., Stiller, G. P., Höpfner, M., Grabowski, U., and Kaufmann, M.: Analysis of nonlocal thermodynamic equilibrium CO 4.7 μ m fundamental, isotopic, and hot band emissions measured by the Michelson Interferometer for Passive Atmospheric Sounding on Envisat, *Journal of Geophysical Research*, 112, doi:10.1029/2006JD007933, 2007.
- Funke, B., López-Puertas, M., García-Comas, M., Stiller, G. P., von Clarmann, T., Höpfner, M., Glatthor, N., Grabowski, U., Kellmann, S., and Linden, A.: Carbon monoxide distributions from the upper troposphere to the mesosphere inferred from 4.7 μ m non-local thermal equilibrium emissions measured by MIPAS on Envisat, *Atmospheric Chemistry and Physics Discussions*, 8, 20 607–20 659, URL <http://www.atmos-chem-phys-discuss.net/8/20607/2008/>, 2008.
- García, R. R. and Solomon, S.: A new numerical model of the middle atmosphere. 2. Ozone and related species, *Journal of geophysical research on atmospheres*, 99, 12 937–51, 1994.
- Heald, C. L., Jacob, D. J., Fiore, A. M., Emmons, L. K., Gille, J. C., Deeter, M. N., Warner, J., Edwards, D. P., Crawford, J. H., Hamlin, A. J., Sachse, G. W., Browell, E. V., Avery, M. A., Vay, S. A., Westberg, D. J., Blake, D. R., Singh, H. B., Sandholm, S. T., Talbot, R. W., and Fuelberg, H. E.: Asian outflow and trans-Pacific transport of carbon monoxide and ozone pollution: An integrated satellite, aircraft, and model perspective, *Journal of Geophysical Research*, 108, 4804–+, 2003.
- Irion, F. W., Gunson, M. R., Toon, G. C., Change, A. Y., Eldering, A., Mahien, E., Manney, E., Michelsen, G. L., Moyer, E. J., Newchurch, M. J.,

- Osterman, G. B., Rinsland, C. P., Salawitch, R. J., Sen, B., Yung, Y. L., and Zander, R.: Atmospheric Trace Molecule Spectroscopy (ATMOS) experiment version 3 data retrievals, *Applied Optics*, 41, 6968–6979, 2002.
- Keim, E. R., Lowenstein, M., Podolske, J. R., Fahey, D. W., Gao, R. S., Woodbridge, E. L., Wamsley, R. C., Donnelly, S. G., Del Negro, L. A., Nevison, C. D., Solomon, S., Rosenlog, K. H., Scott, C. J., Ko, M. K. W., Weisenstein, D., and Chan, K. R.: Measurements of the $\text{NO}_y\text{-N}_2\text{O}$ correlation in the lower-stratosphere: Latitudinal and seasonal changes and model comparisons, *Journal of Geophysical Research*, 102, 13 193–13 212, 1997.
- Kleinert, A., Birk, M., Wagner, G., and Friedl-Vallon, F.: Radiometric accuracy of MIPAS calibrated spectra, *ENVISAT Symposium*, 2007.
- Kumer, J. B., Mergenthaler, J. L., Roche, A. E., Nightingale, R. W., Zele, F., Gille, J. C., Massie, S. T., Bailey, P. L., Connell, P. S., Gunson, M. R., Abrams, M. C., Toon, G. C., Sen, B., Blavier, J.-F., Smith, S. E., and Taylor, F. W.: Comparison of CLAES preliminary N_2O_5 data with correlative data and a model, *Journal of Geophysical Research*, 101, 9657–9678, doi:10.1029/95JD03767, 1996.
- Lelieveld, J., Peters, W., Dentener, F. J., and Krol, M. C.: Stability of tropospheric hydroxyl chemistry, *Journal of Geophysical Research*, 107, 4715, doi:10.1029/2002JD002272, 2002.
- Livesey, J. N., Van Snyder, W., Read, W. G., and Wagner, P. A.: Retrieval Algorithms for the EOS Microwave Limb Sounder (MLS), *IEEE Transactions on Geoscience and Remote Sensing*, 44, 2006.
- Livesey, N. J., Read, W. G., Filipiak, M. J., Froidvaux, L., Harwood, R. S., Jiang, J. H., Jimenez, C., Pickett, H. M., Pumphrey, H. C., Santee, M. L., Schwartz, M. J., Waters, J. W., and Dong, L. W.: Version 1.5 level 2 data quality and description document, Tech. rep., JPL, 2005.

- Livesey, N. J., Read, W. G., Lambert, A., Cofield, R. E., Cuddy, D. T., Froidvaux, L., Fuller, R. A., Jarnot, R. F., Jiang, J. H., Jiang, Y. B., Knosp, B. W., Kovalenko, L. J., Pickett, H. M., Pumphrey, H. C., Santee, M. L., Schwartz, M. J., Stek, P. C., Wagner, P. A., Waters, J. W., and Dong, L. W.: Version 2.2 level 2 data quality and description document, Tech. rep., JPL, 2007.
- Logan, J. A., Prather, M. J., Wofsy, S. C., and McElroy, M. B.: Tropospheric chemistry - A global perspective, *Journal of Geophysical Research*, 86, 7210–7254, 1981.
- López-Puertas, M. and Funke, B.: Remote Sensing of the non-LTE Atmosphere, *Remote Sensing of the Atmosphere for Environmental Security*, 2007.
- López-Puertas, M. and Taylor, F. W.: Non-LTE Radiative Transfer in the Atmosphere, World Scientific, 2001.
- López-Puertas, M., López-Valverde, M., A., Edwards, D. P., and Taylor, F., W.: Non-Local-Thermodynamic-Equilibrium Populations of the First Vibrational Excited State of CO in the Middle Atmosphere, *Journal of Geophysical Research*, 98, 8933–8947, 1993.
- López-Valverde, M., A., López-Puertas, M., Remedios, J. J., Rodgers, C. D., Taylor, E. C., Zipf, E. C., and Erdman, P. W.: Validation of measurements of carbon monoxide from the improved stratospheric and mesospheric sounder, *Journal of Geophysical Research*, 101, 9929–9955, 1996.
- Lowenstein, M., Podolske, J. R., Fahey, D. W., Woodbridge, E. L., Tin, P., Weaver, A., Newman, P. A., Strahan, S. E., Kawa, S. R., Schoeberl, M. R., and Lait, L. R.: New observations of the NO_y/N₂O correlation in the lower stratosphere, *Geophysical Research Letters*, 20, 2531–2534, 1993.

- Luo, M., Rinsland, C. P., Rodgers, C. D., Logan, J. A., Worden, H., Kulawik, S., Eldering, A., Goldman, A., Shephard, M. W., Gunson, M., and Lampel, M.: Comparison of carbon monoxide measurements by TES and MOPITT: Influence of a priori data and instrument characteristics on nadir atmospheric species retrievals, *Journal of Geophysical Research*, 112, 2007.
- Madronich, S.: TUV: Tropospheric Ultraviolet and Visible Radiation Model, Tech. rep., NCAR/ACD, URL <http://cprm.acd.ucar.edu/Models/TUV/>, 2006.
- Madronich, S. and Flocke, S.: The role of solar radiation in atmospheric chemistry, Springer, *Handbook of Environmental Chemistry*, edited by P. Boule, 1998.
- Mengistu Tsidu, G., von Clarmann, T., Stiller, G. P., Höpfner, M., Fischer, H., Glatthor, N., Grabowski, U., Kellmann, S., Kiefer, M., Linden, M., Milz, M., Steck, T., Wang, D. Y., and Funke, B.: Stratospheric N₂O₅ in the austral spring 2002 as retrieved from limb emission spectra recorded by the Michelson Interferometer for Passive Atmospheric Sounding (MIPAS), *Journal of Geophysical Research*, 109, doi:10.1029/2004JD004856, 2004.
- Michelsen, H. A., Manney, G. L., Gunson, M. R., and Zander, R.: Correlations of stratospheric abundances of NO_y, O₃, N₂O, and CH₄ derived from ATMOS measurements, *Journal of Geophysical Research*, 103, 28 347–28 359, 1998.
- MIPAS Product Handbook [Internet]: URL <http://envisat.esa.int/dataproducts/mipas>, 2008.
- Nash, E.R. and Newman, P. A. and Rosenfield, J., E and Schoeberl, M. R.: An objective determination of the polar vortex using Ertel's potential vorticity, *Journal of Geophysical Research*, 101, 9471–9478, 1996.

- Naudet, J. P., Huguenin, D., Rigaud, P., and Cariolle, D.: Stratospheric observations of NO_3 and its experimental and theoretical distribution between 20 and 40 km, *Planetary and Space Science*, 32, 707–711, 1981.
- Nevison, C. D., Solomon, S., and Russell, J. M.: Nighttime formation of N_2O_5 inferred from the Halogen Occultation Experiment sunset/sunrise NO_x ratios, *Journal of Geophysical Research*, 101, 6741–6748, 1996.
- Newell, R. E.: One dimensional models: a critical comment, and their application to carbon monoxide, *Journal of Geophysical Research*, 82, 1449–1450, 1977.
- Norton, R. H. and Beer, R.: New apodizing functions for Fourier spectrometry, *J. Opt. Soc. Am.*, 259, and errata corrige *J. Opt. Soc. Am.*, 67, 419, (1977), 1976.
- Plumb, A. and Ko, M. K. W.: Interrelationships between mixing ratios of long-lived stratospheric constituents, *Journal of Geophysical Research*, 97, 10 145–10 156, 1992.
- Pumphrey, H. C., Filipiak, M. J., Livesey, N. J., Schwartz, M. J., Boone, C., Walker, K. A., Bernath, P., Ricaud, P., Barret, B., Clerbaux, C., Jarnot, R. F., Manney, G. L., and Waters, J. W.: Validation of middle-atmosphere carbon monoxide retrievals from the Microwave Limb Sounder on Aura, *Journal of Geophysical Research*, 112, doi:10.1029/2007JD008723, 2007.
- Randall, C. E., Siskind, D. E., and Bevilacqua, R. M.: Stratospheric NO_x Enhancements in the Southern Hemisphere Vortex in Winter/Spring of 2000, *Geophysical Research Letters*, 28, 2385–2388, 2001.
- Raspollini, P., Belotti, C., Burgess, A., Carli, B., Carlotti, M., Ceccherini, S., Dinelli, B. M., Dudhia, A., Flaud, J.-M., Funke, B., Hpfner, M., Lopez-Puertas, M., Payne, V., Piccolo, C., Remedios, J. J., Ridolfi, M., and Spang, R.: MIPAS level 2 operational analysis, *Atmospheric Chemistry and*

- Physics, 6, 5605–5630, URL <http://www.atmos-chem-phys.net/6/5605/2006/>, 2006.
- Remedios, J. J., Leigh, R. J., Waterfall, A. M., Moore, D. P., Sembhi, H., Parkes, I., Greenhough, J., Chipperfield, M., and Hauglustaine, D.: MIPAS reference atmospheres and comparisons to V4.61/V4.62 MIPAS level 2 geophysical data sets, *Atmospheric Chemistry and Physics Discussions*, 7, 9973–10 017, 2007.
- Ridolfi, M., Carli, B., Carlotti, M., von Clarmann, T., Dinelli, B., M., Dudhia, A., Flaud, J. M., Höpfner, M., Morris, P. E., Raspollini, P., Stiller, G., and Wells, R. J.: Optimized forward model and retrieval scheme for MIPAS near-real-time data processing, *Optical Society of America*, 39, 1323–1340, 2000.
- Rodgers, C. D.: *Inverse Methods for Atmospheric Sounding*, World Scientific, 2000.
- Rothman, L. S., Rinsland, C. P., Goldman, A., Massie, S. T., Edwards, D. P., Flaud, J. M., Perrin, A., Camy-Peyret, C., Dana, V., Mandin, J., Y., Schroeder, J., McCann, A., Gamache, R. R., Wattson, R. B., Yoshino, K., Chance, K. V., Jucks, K. W., Brown, L. R., Nemtchinov, V., and Varanasi, P.: The HITRAN Molecular Spectroscopic Database and HAWKS (HITRAN Atmospheric Workstation): 1996 edition, *Journal of Quantitative Spectroscopy and Radiative Transfer*, 60, 665–710, 1998.
- Shannon, C. E. and Weaver, W.: *The Mathematical Theory of Communications*, University of Illinois Press, Urbana, 1962.
- Smith, S. E., Dudhia, A., Morris, P. E., Remedios, J. J., Rodgers, C. D., Taylor, F. W., Kerridge, B. J., Chipperfield, M. P., Kumer, J. B., Roche, A. E., and Gunson, M. R.: N₂O₅ measurements from the ISAMS: validation and preliminary results, *Journal of Geophysical Research*, 101, 9897–9906, 1996.

- Spang, R., Remedios, J., J., and Barkley, M., P.: Colour indices for the detection and differentiation of cloud types in infra-red limb emission spectra, *Advances in Space Research*, 33, doi:10.1016/S0273-1177(03)00585-4, 2004.
- Stamnes, K., Tsay, S.-C., Wiscombe, W., and Jayaweera, K.: Numerically stable algorithm for discrete-ordinate-method radiative transfer in multiple scattering and emitting layered media, *Applied Optics*, 27, 2502–2509, 1988.
- Stan, C. and Randall, D.: Potential Vorticity as Meridional Coordinate, American Meteorological Society, 2007.
- Stiller, G. P. and et al.: An enhanced HNO₃ second maximum in the Antarctic midwinter upper stratosphere 2003, *Journal of Geophysical Research*, D20303, doi:doi:10.1029/2005JD006011, 2005.
- Stiller, G. P. and von Clarmann, T.: The Karlsruhe Optimized and Precise Radiative transfer Algorithm (KOPRA), Tech. rep., IMK (Institute for Meteorology and Climate Research), 2008.
- Stiller, G. P., von Clarmann, T., Funke, B., Glatthor, N., Hase, F., Höpfner, M., and Linden, A.: Sensitivity of trace gas abundances retrievals from infrared limb emission spectra to simplifying approximations in radiative transfer modelling, *Journal of Quantitative Spectroscopy and Radiative Transfer*, 72, 249–280, 2002.
- Stiller, G. P., von Clarmann, T., Chidiezie Chineke, T., Fischer, H., Funke, B., Gil-Lopez, S., Glatthor, N., Grabowski, U., Hoepfner, M., Kellmann, S., Kiefer, M., Linden, A., Lopez-Puertas, M., Mengistu Tsidu, G., Milz, M., and Steck, T.: Early IMK/IAA MIPAS/ENVISAT results, in: Society of Photo-Optical Instrumentation Engineers (SPIE) Conference Series, edited by Schaefer, K. P., Lado-Bordowsky, O., Comeron, A., and Picard, R. H., vol. 4882 of *Society of Photo-Optical Instrumentation Engineers (SPIE) Conference Series*, pp. 184–193, doi:10.1117/12.465164, 2003.

- Thomason, L. W., Pitts, M. C., and Winker, D. M.: CALIPSO observations of stratospheric aerosols: a preliminary assessment, *Atmospheric Chemistry and Physics Discussions*, 7, 5595–5615, URL <http://hal.archives-ouvertes.fr/hal-00302732/en/>, 2007.
- Toon, G. C., Farmer, C. B., and Norton, R. H.: Detection of stratospheric N₂O₅ by infrared remote sounding, *Nature*, 319, 570–571, 1986.
- Toumi, R. and Pyle, J. A. and Webster, C. R.: Theoretical interpretation of N₂O₅ measurements, *Geophysical Research Letters*, 18, 1213–1216, 1991.
- von Clarmann, T., Höpfner, M., Kellmann, S., Linden, A., Chauhan, S., Funke, B., Grabowski, U., Glatthor, N., Kiefer, M., Schieferdecker, T., Stiller, G. P., and Versick, S.: Retrieval of temperature, H₂O, O₃, HNO₃, CH₄, N₂O, ClONO₂ and ClO from MIPAS reduced resolution nominal mode limb emission measurements, *Atmospheric Measurement Techniques Discussions*, 2, 181–236, 2009.
- Wang, J., Gille, J. C., Bailey, P. L., Liwen, P., and Edwards, D.: Retrieval of Tropospheric Carbon Monoxide Profiles from High-Resolution Interferometer Observations: A New Digital Gas Correlation (DGC) Method and Applications, American Meteorological Society, 1999.
- Warneck, P.: *Chemistry of the Natural Atmosphere*, vol. 41, International Geophysics Series, 1988.
- Waters, J. W., Froidevaux, L., and Harwood et al., R. S.: The Earth Observing System Microwave Limb Sounder (EOS MLS) on the Aura Satellite, *IEEE Transactions on Geoscience and Remote Sensing*, 44, 2006.
- Webster, C. R., May, R. D., Toumi, R., and Pyle, J.: Active Nitrogen Partitioning and the Nighttime Formation of N₂O₅ in the Stratosphere: Simultaneous in Situ Measurements of NO, NO₂, HNO₃, O₃, and N₂O Using

- the BLISS Diode Laser Spectrometer, *Journal of Geophysical Research*, **95**, 13 851–13 866, 1990.
- Wetzel, G., Oelhaf, H., von Clarmann, T., Fischer, H., Friedl-Vallon, F., Maucher, G., Seefeldner, M., Trieschmann, O., and Lefèvre, F.: Vertical profiles of N₂O₅, HO₂NO₂, and NO₂ inside the Arctic vortex, retrieved from nocturnal MIPAS-B2 infrared limb emission measurements in February 1995, *Journal of Geophysical Research*, **102**, 19,177–19,186, 1997.
- Wiegele, A., Kleinert, A., Oelhaf, H., Ruhnke, R., Wetzel, G., Friedl-Vallon, F., Lengel, A., Maucher, G., Nordmeyer, H., and Fischer, H.: Spatiotemporal variations of NO_y species in the northern latitudes stratosphere measured with the balloon-borne MIPAS instrument, *Atmospheric Chemistry and Physics Discussions*, **8**, 4693–4725, 2008.
- Wolff, M. A., Kerzenmacher, T., Strong, K., Walker, K. A., Tooney, M., Dupuy, E., Bernath, P. F., Boone, C. D., Brohede, S., Catoire, V., von Clarmann, T., Coffey, M., Daffer, W. H., De Mazire, M., Duchatelet, P., Glatthor, N., Griffith, D. W. T., Hannigan, J., Hase, F., Höpfner, M., Huret, N., Jones, N., Jucks, K., Kagawa, A., Kasai, Y., Kramer, I., Kllmann, H., Kuttippurath, J., Mahieu, E., Manney, G., McLinden, C., Mbarki, Y., Mikuteit, S., Murtagh, D., Piccolo, C., Raspollini, P., Ridolfi, M., Ruhnke, R., Santee, M., Senten, C., Smale, D., Ttard, C., Urban, J., and Wood, S.: Validation of HNO₃, ClONO₂, and N₂O₅ from the Atmospheric Chemistry Experiment Fourier Transform Spectrometer (ACE-FTS), *Atmospheric Chemistry and Physics Discussions*, **8**, 2429–2512, 2008.
- World Meteorological Organization (WMO): Atmospheric ozone 1985: Assessment of our understanding of the processes controlling its present distribution and change, Tech. Rep. rep. 16, WMO, Geneva, global Ozone Research and Monitoring Project, 1985.